INTERNATIONAL SCIENTIFIC JOURNAL

MATHEMATICAL MODELING

YEAR IX, ISSUE 1/2025
ISSN (PRINT) 2535-0986
ISSN (WEB) 2603-2929

Published by
SCIENTIFIC-TECHNICAL UNION of MECHANICAL ENGINEERING - INDUSTRY 4.0
Sofia, BULGARIA

INTERNATIONAL SCIENTIFIC JOURNAL

MATHEMATICAL MODELING

PUBLISHER:

SCIENTIFIC TECHNICAL UNION OF MECHANICAL ENGINEERING "INDUSTRY 4.0"

108, Rakovski Str., 1000 Sofia, Bulgaria
tel. (+359 2) 987 72 90,
tel./fax (+359 2) 986 22 40**,**
office@stumejournals.com
www.stumejournals.com

ISSN (PRINT) 2535-0986
ISSN (WEB) 2603-2929
YEAR IX, ISSUE 1 / 2025

All articles are published after peer review by two independent reviewers.

EDITOR IN CHIEF:

Assoc. Prof. D.Sc. Milena Racheva
Technical University of Gabrovo

C O N T E N T S

THEORETICAL FOUNDATIONS AND SPECIFICITY OF MATHEMATICAL MODELLING

Improved RBF Method for High-Accuracy Reconstruction of Complex Two- Dimensional Fields
Skerdi Hymeraj, Saimir Tola 3

MATHEMATICAL MODELLING OF TECHNOLOGICAL PROCESSES AND SYSTEMS

Modelling of LTL routes for eco-diversed transport application
Radosław Belka, Wojciech Belka 11

Isentropic and exergy analyses of turbomachines from co2 supercritical power plant
Mrzljak Vedran, Prpić-Oršić Jasna, Baressi Šegota Sandi, Lorencin Ivan 15

The solution of the boundary value problems of the transfer processes in multilayer enclosing structures
Renat Sadykov 19

The theory of transfer processes with short-term contact phases
Renat Sadykov, Airat Osipov, Artem Akhmerov 23

Numerical analysis of substrate influence on fracture mechanisms in PVD deposited TiN coatings
Bartlomiej Kowal, Konrad Perzynski, Lukasz Madej 28

CFD and Differential Evolution Optimization of an Air-To-Air Heat Recovery System for an Industrial Dryer
Oğulcan Sogut, Y.Yağız Simsek, M. Baris Yildiz, Yusuf Sahinoglu, Nesrin Sen, Onur Cimen, I. Etem Saklakoglu 30

Statistical analysis of data on electricity generated from a small-capacity hydro power plant
Svilen Rachev, Milena Racheva, Lyubomir Dimitrov 34

MATHEMATICAL MODELLING OF MEDICAL-BIOLOGICAL PROCESSES AND SYSTEMS

Mechanical Behavior of Vein under Medical Compression Stocking Preliminary Numerical Investigations
Nikola Nikolov, Elena Goranova 41

Improved RBF Method for High-Accuracy Reconstruction of Complex Two-Dimensional Fields

Skerdi Hymeraj, Saimir Tola,
Polytechnic University of Tirana, Tirane, Faculty of Mathematical & Physical Engineering
Skerdihymeraj02@gmail.com

Abstract: *Radial Basis Function (RBF) interpolation is widely used for reconstructing scattered multidimensional data, but its accuracy and stability often depend heavily on the point distribution, kernel choice, and matrix conditioning. This work proposes an improved RBF framework that combines a whitening transformation, adaptive sampling, and cross-validated parameter tuning to obtain more reliable reconstructions of complex two-dimensional fields. Whitening reduces geometric distortions and improves conditioning, while the adaptive sampling strategy focuses points in regions with strong gradients. Tests on a deliberately challenging synthetic function show that the whitening-enhanced RBF model achieves higher stability and lower error (in L1, L2, and L∞ norms) compared to the standard RBF formulation. The method is implemented in Python using open-source libraries and performs efficiently even on modest hardware.*

KEYWORDS: *RADIAL BASIS FUNCTIONS (RBF), SCATTERED DATA INTERPOLATION, WHITENING TRANSFORM, SHAPE-PARAMETER TUNING, CROSS-VALIDATION, ADAPTIVE SAMPLING, GAUSSIAN / MULTIQUADRIC / INVERSE MULTIQUADRIC / THIN-PLATE SPLINE KERNELS.*

Introduction

Multivariate interpolation on scattered data arises in a broad spectrum of applications, including scientific computing, engineering design, geostatistics, machine learning and uncertainty quantification. Among the most flexible and widely used approaches, Radial Basis Function (RBF) [1], [5] methods provide a mesh-free framework capable of approximating complex functions in moderate to high dimensions while directly handling irregular point clouds. Despite their conceptual simplicity, practical RBF schemes are notoriously sensitive to several interacting factors. The geometry of the input space—such as anisotropic scaling and strong correlations between coordinates—can distort Euclidean distances and degrade the quality of the approximation. The choice of the kernel type and, in particular, the tuning of the shape parameter ε critically affects both approximation power and numerical conditioning. Finally, noisy data and ill-conditioned kernel matrices may lead to strong overfitting or unstable coefficient estimates, especially in the absence of appropriate regularization. Over the last decades, numerous strategies have been proposed to ameliorate these issues, including multi-scale RBFs, adaptive shape parameter selection, localized and partition-of-unity formulations, and combinations with polynomial reproduction or smoothing regularization. However, many of these techniques either rely on problem-specific heuristics or require delicate manual tuning, and they often treat scaling, shape selection and stability as separate concerns.

This work proposes a systematic and fully data-driven approach that addresses these aspects in an integrated manner. The core idea is to normalize the geometry of the input space via whitening, quantify the typical point spacing through a local length scale, and then perform a stability-aware hyperparameter search over a rich family of RBF models. The final predictor is not a single model but an ensemble of top-performing configurations, weighted by their empirically observed predictive accuracy. The main contributions of the paper are:

- A covariance-based whitening transformation that regularizes the input space and improves the conditioning of RBF kernels.
- A data-driven local length scale derived from nearest-neighbor distances in the whitened space, used to define a dimensionless shape parameter.
- A stability-penalized effective score that couples cross-validated RMSE with a quadratic penalty in the dimensionless shape, discouraging unstable regimes.
- An ensemble construction that aggregates several top RBF models into a robust predictor with accuracy-based weights.

The remainder of this paper is organized as follows. Section 2 introduces the proposed Stability–Penalized RBF Ensemble (SP–RBF–ENS) method at a high level. Section 3 reports numerical experiments, and Section 4 concludes the paper with a summary of the main findings and an outline of future research directions.

1. Stability-Enhanced RBF Interpolation with Whitening and Cross-Validation

In this work we employ a stability-enhanced Radial Basis Function (RBF) interpolation framework that combines data whitening, a data-driven length-scale selection based on nearest-neighbor distances, and systematic hyperparameter tuning via k-fold crossvalidation. The overall goal is to construct a robust and accurate interpolant on potentially anisotropic and ill-conditioned data sets, while avoiding ad-hoc parameter choices and manual tuning.

We assume that we are given a set of scattered samples

$$\mathcal{D} = \{(x_i, y_i)\}_{i=1}^{n}, x_i \in \mathbb{R}^d, y_i \in \mathbb{R},$$

and we seek an approximation $s: \mathbb{R}^d \to \mathbb{R}$ such that $s(x_i) \approx y_i$ for all i, and which

1.1 Data Whitening and Geometric Standardization

A first source of instability in multivariate interpolation arises when different coordinates of x_i live on very different scales or exhibit strong correlations. To mitigate this, we introduce an affine "whitening" transform which maps the original data to a more isotropic configuration [6].

Let $X \in \mathbb{R}^{n\times d}$ be the data matrix collecting the sample locations in its rows,

$$X = \begin{bmatrix} x_1^\top \\ \vdots \\ x_n^\top \end{bmatrix}, \qquad x_i \in \mathbb{R}^d.$$

We define the empirical mean vector.

$$\mu = \frac{1}{n}\sum_{i=1}^{n} x_i \in \mathbb{R}^d,$$

and the empirical covariance matrix of the centered data

$$S = \frac{1}{n-1}\sum_{i=1}^{n} (x_i - \mu)(x_i - \mu)^\top \in \mathbb{R}^{d\times d}$$

To guarantee numerical stability, we add a small Tikhonov-type regularization on the diagonal,

$$S_\delta = S + \delta I_d, \delta > 0 \text{ very small },$$

and compute a Cholesky factorization

$$S_\delta = LL^\top, L \in \mathbb{R}^{d\times d}$$

with L lower triangular and $\mathrm{diag}(L) > 0$. The whitening transform is then defined by

$$T(x) := (x - \mu)L^{-1}, x \in \mathbb{R}^d.$$

Applying this to all data points yields the whitened nodes

$$z_i = T(x_i) = (x_i - \mu)L^{-1}, i = 1, \dots, n,$$

which we collect into the matrix $Z \in \mathbb{R}^{n\times d}$. Neglecting the tiny regularization, one has the approximate identity

$$\mathrm{Cov}(Z) \approx L^{-1}\mathrm{Cov(X)}L^{-\top} = L^{-1}SL^{-\top} \approx I_d,$$

so that the transformed data are roughly isotropic. In practice, this significantly improves

so that the transformed data are roughly isotropic. In practice, this significantly improves the conditioning of the subsequent RBF interpolation system and makes the choice of the shape parameter

more meaningful and less sensitive to the original scaling of the coordinates.

1.2 Data-Driven Length Scale via Nearest–Neighbor Distances

Once the data have been whitened, we extract a characteristic length scale from the spatial distribution of the nodes $\{z_i\}$. For each node z_i we define the distance to its closest neighbor (excluding itself)

$$d_i := \min_{j \neq i} \|z_i - z_j\|_2, i = 1, \dots, n.$$

We then use the median of these distances as a robust estimate of the typical inter-point spacing:

$$\ell := \text{median}\{d_1, \dots, d_n\}.$$

This quantity ℓ plays the role of a natural geometric length scale in the whitened space. We exploit it to define a scale-invariant range for the RBF shape parameter ε. Specifically, we generate a set of candidate values of the form

$$\varepsilon_j = \frac{1}{\ell} 10^{\alpha_j}, \alpha_j \in [\alpha_{\min}, \alpha_{\max}]$$

where $\{\alpha_j\}$ are placed on a logarithmic grid. In this way, the shape parameter is searched over several orders of magnitude relative to the intrinsic spacing of the data, rather than in absolute, problem–dependent units.

1.3 RBF Interpolant with Polynomial Tail and Smoothing

On the whitened nodes z_i, we construct an RBF interpolant that, in its most general form, reads [1] :

$$s(z) = \sum_{j=1}^{n} \lambda_j \phi\left(\frac{\|z - z_j\|_2}{\varepsilon}\right) + p(z), z \in \mathbb{R}^d.$$

Here:

- $\phi: [0, \infty) \to \mathbb{R}$ is a radial basis kernel, chosen from a prescribed family such as Gaussian, multiquadric, inverse multiquadric, or thin-plate spline;
- $\varepsilon > 0$ is the shape parameter (for kernels that require it);
- $p(z)$ is a multivariate polynomial of degree at most m, included when the kernel is only conditionally positive definite.

1. Gaussian
$$\varphi(r) = \exp(-(\varepsilon r)^2)$$
2. Inverse Multiquadric (IMQ)
$$\varphi(r) = \frac{1}{\sqrt{1 + (\varepsilon r)^2}}$$
3. Multiquadric (MQ)
$$\varphi(r) = \sqrt{1 + (\varepsilon r)^2}$$
4. Thin Plate Spline (TPS)
$$\varphi(r) = r^2 \log r \ (r > 0), \varphi(0) = 0$$

Let $\Phi \in \mathbb{R}^{n \times n}$ be the RBF Gram matrix with entries

$$\Phi_{ij} = \phi\left(\frac{\|z_i - z_j\|_2}{\varepsilon}\right), i, j = 1, \dots, n$$

and let $P \in \mathbb{R}^{n \times M}$ denote the polynomial design matrix defined by

$$P_{ik} = q_k(z_i), k = 1, \dots, M,$$

where $\{q_k\}$ is a basis of the polynomial space $\mathbb{P}_m(\mathbb{R}^d)$. To enhance robustness and mitigate overfitting or numerical ill-conditioning, we incorporate a small smoothing parameter $\eta \geqslant 0$. The coefficients $\lambda \in \mathbb{R}^n$ and $c \in \mathbb{R}^M$ are then obtained by solving the augmentea linear system

$$\begin{bmatrix} \Phi + \eta I_n & P \\ P^\top & 0 \end{bmatrix} \begin{bmatrix} \lambda \\ c \end{bmatrix} = \begin{bmatrix} y \\ 0 \end{bmatrix},$$

where I_n is the $n \times n$ identity matrix and $y \in \mathbb{R}^n$ is the vector of sampled function values. The regularization ηI_n acts as a Tikhonov term that stabilizes the inversion of Φ, especially in the presence of nearly dependent rows [8].

The polynomial degree m is chosen according to the kernel; strictly positive definite kernels (e.g. Gaussian, inverse multiquadric) typically use $m = 0$ (no polynomial tail), whereas conditionally positive definite kernels (e.g. linear, cubic, thin-plate spline) require $m \geq 1$ to guarantee uniqueness of the solution.

In large data sets, the method can optionally be localized by restricting the interpolation stencil of each point to its N_{neigh} nearest neighbors. This leads to a sparse, locally supported approximation that significantly reduces computational cost while preserving high accuracy.

1.4 Hyperparameter Selection via k-Fold Cross-Validation

The RBF interpolant depends on several hyperparameters: the choice of kernel ϕ, the shape parameter ε, the smoothing parameter η, and the polynomial degree m. Rather than fixing these parameters manually, we determine them in a data-driven manner using k-fold cross-validation [10].

Let $\mathcal{K}$ denote the set of candidate kernels, $\mathcal{E}$ the set of candidate shape parameters (derived from the length scale ℓ), and $\mathcal{S}$ the set of candidate smoothing values. For each triple $(k, \varepsilon, \eta) \in \mathcal{K} \times \mathcal{E} \times \mathcal{S}$ we proceed as follows:

1. Randomly partition the index set $\{1, \dots, n\}$ into k disjoint folds
$$\{1, \dots, n\} = F_1 \cup \dots \cup F_k, F_i \cap F_j = \emptyset (i \neq j).$$
2. For each fold $r = 1, \dots, k$, define trai ↓ J and validation index sets
$$T_r = \{1, \dots, n\} \setminus F_r, V_r = F_r.$$
3. Construct an RBF interpolant $s_r^{(k,\varepsilon,\eta)}$ using only the training data $\{(z_i, y_i)\}_{i \in T_r}$.
4. Evaluate $s_r^{(k,\varepsilon,\eta)}$ on the validation points $\{z_i\}_{i \in V_r}$ and compute the root-meansquare error (RMSE)
$$E_r(k, \varepsilon, \eta) = \sqrt{\frac{1}{|V_r|} \sum_{i \in V_r} \left(s_r^{(k,\varepsilon,\eta)}(z_i) - y_i\right)^2}.$$
5. Define the cross-validated performance index as the average validation error over all folds,
$$\mathcal{J}(k, \varepsilon, \eta) = \frac{1}{k} \sum_{r=1}^{k} E_r(k, \varepsilon, \eta).$$

The optimal hyperparameters are then obtained by solving the discrete minimization problem

$$(k^*, \varepsilon^*, \eta^*) = \arg\min_{k \in \mathcal{K}, \varepsilon \in \mathcal{E}, \eta \in \mathcal{S}} \mathcal{J}(k, \varepsilon, \eta).$$

In practice, we also associate to each kernel k an appropriate polynomial degree $m(k)$, so the polynomial degree is adapted jointly with the kernel.

This cross-validation loop provides an automatic mechanism for balancing accuracy and stability: aggressive choices of ε or very smam smoothing η are penalized if they produce poor predictive performance on validation folds.

1.5 Final Predictor in the Original Coordinate System

After selecting the optimal hyperparameters $(k^*, \varepsilon^*, \eta^*, m^*)$, we retrain a final RBF interpolant on all whitened data $\{(z_i, y_i)\}_{i=1}^n$. This yields a function

$$s^*: \mathbb{R}^d \to \mathbb{R}, s^*(z) = \sum_{j=1}^{n} \lambda_j^* \phi^*\left(\frac{\|z - z_j\|_2}{\varepsilon^*}\right) + p^*(z)$$

where ϕ^* is the selected kernel and p^* is the corresponding polynomial tail [7]. The final predictor in the original coordinate system is obtained by composing s^* with the whitening transform T,

$$\hat{f}(x) = s^*(T(x)) = s^*((x - \mu)L^{-1}), x \in \mathbb{R}^d.$$

For any new query point x, we first standardize it via whitening and then evaluate the RBF interpolant in the whitened space. This ensures full consistency between training and prediction and preserves the numerical advantages of working in a geometrically normalized coordinate system.

2.The experiments

2.1 Geometrically Complex Benchmark Function and Sampling Strategies

In order to assess the accuracy and robustness of the proposed interpolation methods, we introduce a synthetic benchmark on the unit square

$$\Omega = [0,1]^2 \subset \mathbb{R}^2$$

which exhibits a rich combination of anisotropic, multiscale and oscillatory features. This section provides a rigorous mathematical description of the test function and of the sampling strategies used to generate the training data.

2.1.1 Definition of the geometrically complex test function

Let $(x, y) \in \Omega$ and define the centered Cartesian coordinates

$$x_c = x - \frac{1}{2}, y_c = y - \frac{1}{2}$$

together with the polar variables

$$r = \sqrt{x_c^2 + y_c^2}, \theta = \text{atan2}(y_c, x_c) \in (-\pi, \pi]$$

The benchmark function $f: \Omega \to \mathbb{R}$ is constructed as a superposition of six components,

$$f(x,y) = f_{\text{gauss}}(x,y) + f_{\text{ring}}(x,y) + f_{\text{ridge}}(x,y) + f_{\text{hole}}(x,y) + f_{\text{strip}}(x,y) + f_{\text{tilt}}(x,y),$$

each of which is detailed below.

(i) Rotated anisotropic Gaussian bump. We first introduce a sharp anisotropic Gaussian centred at

$$(x_0, y_0) = (0.25, 0.70)$$

rotated by an angle $\alpha = 30° = \pi/6$. Let

$$R(\alpha) = \begin{pmatrix} \cos\alpha & \sin\alpha \\ -\sin\alpha & \cos\alpha \end{pmatrix}$$

be the rotation matrix, and define the rotated local coordinates

$$\begin{pmatrix} x_r \\ y_r \end{pmatrix} = R(\alpha) \begin{pmatrix} x - x_0 \\ y - y_0 \end{pmatrix}.$$

With anisotropic length scales

$$a = 0.08, b = 0.25$$

the Gaussian contribution takes the form

$$f_{\text{gauss}}(x,y) = 1.2\exp\left(-\left(\frac{x_r}{a}\right)^2 - \left(\frac{y_r}{b}\right)^2\right).$$

This term produces a sharp, elongated feature oriented along a non-axis-aligned direction, which is challenging for interpolation schemes that assume isotropy.

(ii) Warped ring with angular modulation. To generate a ring-like structure with angular oscillations we conside $f_{\text{ring}}(x,y) = 0.9\exp\left(-\left(\frac{r-0.35}{0.06}\right)^2\right)(1 + 0.3\cos(12\theta))$.

The Gaussian in r localizes the feature around the circle $r \approx 0.35$, while the factor $1 + 0.3\cos(12\theta)$ introduces a 12 -fold angular modulation. This term couples radial localisation with high-frequency angular behaviour.

(iii) Narrow diagonal ridge. We next add a narrow oscillatory ridge aligned approximately along the diagonal line $y = 1 - x$. Let $\sigma_{\text{ridge}} = 0.02$ and define

$$f_{\text{ridge}}(x,y) = 0.4\sin(8\pi(x+y))\exp\left(-\frac{(y-(1-x))^2}{2\sigma_{\text{ridge}}^2}\right)$$

The Gaussian factor creates a thin strip of width $\mathcal{O}\left(\sigma_{\text{ridge}}\right)$ around the diagonal, while $\sin(8\pi(x+y))$ imposes high-frequency oscillations along that strip.

(iv) Local anisotropic "crater". A localised negative feature (crater) is placed near the point (0.8,0.2). Let $\sigma_{x,\text{h}} = 0.03$ and $\sigma_{y,\text{h}} = 0.05$. The corresponding term is

$$f_{\text{hole}}(x,y) = -0.7\exp\left(-\frac{(x-0.8)^2}{2\sigma_{x,\text{h}}^2} - \frac{(y-0.2)^2}{2\sigma_{y,\text{h}}^2}\right)$$

Due to the different variances in x and y, this crater is anisotropic and illustrates the capability of the interpolation method to cope with highly localised depressions.

(v) Narrow oscillatory strip near $y \approx 0.7$. To further stress-test the method we place a narrow horizontally oriented oscillatory band. Setting $\sigma_{\text{strip}} = 0.015$, we define

$$f_{\text{strip}}(x,y) = 0.3\sin(10\pi x)\exp\left(-\frac{(y-0.7)^2}{2\sigma_{\text{strip}}^2}\right).$$

This component introduces fast oscillations in x confined to a thin strip in the y-direction.

(vi) Smooth polynomial tilt. Finally, a smooth background trend is superimposed via the bilinear term

$$f_{\text{tilt}}(x,y) = 0.1(x-0.5)(y-0.3).$$

This ensures that the global behaviour of f is not purely oscillatory and provides a low-frequency component that must also be captured by the interpolant.

Collecting all components yields the composite benchmark function:

- fring-like structures with angular modulation;
- diagonal ridges with high-frequency oscillations;
- localised negative craters;
- narrow oscillatory strips; and
- a smooth polynomial tilt.

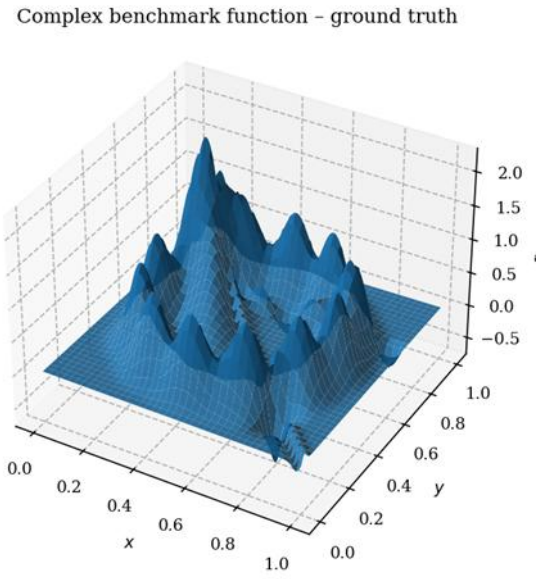


Figure 1. *Three–dimensional surface plot of the geometrically complex benchmark function defined in the domain* $[0,1]^2$.

This makes f a demanding test case for scattered-data interpolation and sampling strategies on Ω.

For convenience, when working with a point cloud $P = \{p_i\}_{i=1}^N \subset \Omega, p_i = (x_i, y_i)$, we use the shorthand

$$f(P) := \left(f(x_i, y_i)\right)_{i=1}^N,$$

which corresponds to the geo_complex_on_points function in the implementation when executing the python code.

2.1.2 Sampling strategies for training points

We now describe the strategies used to generate the set of training nodes $X_{\text{train}} \subset \Omega$. For a prescribed number of points N, we construct a point set $P_N = \{p_i\}_{i=1}^N$ according to one of the following schemes and optionally augment it with boundary points.

Latin Hypercube Sampling on $[\mathbf{0}, \mathbf{1}]^2$

In the Latin Hypercube Sampling (LHS) strategy, the interval [0,1] is partitioned into N disjoint strata of equal length. For each dimension we draw one point in each stratum and then apply a random permutation independently in each coordinate direction. [2]

Formally, let $\{\xi_i\}_{i=0}^{N-1}$ and $\{\zeta_i\}_{i=0}^{N-1}$ be independent random variables uniformly distributed on [0,1]. Define

$$u_i = \frac{i + \xi_i}{N}, v_i = \frac{i + \zeta_i}{N}, i = 0, \dots, N-1.$$

Let π_1 and π_2 be two independent random permutations of $\{0, \dots, N-1\}$. The N LHS points are then given by

$$p_i = \left(u_{\pi_1(i)}, v_{\pi_2(i)}\right), i = 0, \dots, N-1.$$

This construction enforces stratification in each coordinate and tends to reduce variance compared to purely random sampling.

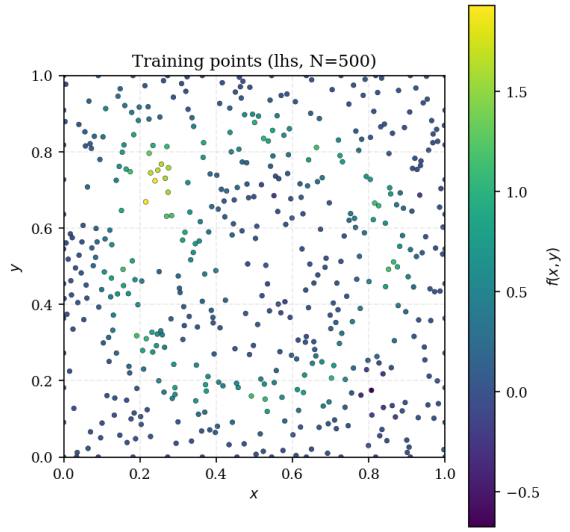


Figure 2. *Two-dimensional scatter plot of the training sample set within the domain* $[0,1]^2$*, generated using Latin Hypercube Sampling with a total of* $N = 500$ *nodes. The color encoding reflects the true function values* $f(x, y)$ *at each sample point, providing insight into spatial variation and the distribution of high-gradient regions prior to interpolation.*

Blue-noise sampling via farthest point strategy

The farthest point sampling (FPS) scheme aims at approximating a blue-noise distribution in Ω, i.e. a configuration of points that is both random and well-spaced [3]. Let M be the number of candidate points with

$$M = \max(10N, 2000)$$

and draw

$$C = \{c_j\}_{j=1}^{M} \subset \Omega$$

i.i.d. from the uniform distribution on $[0,1]^2$. The FPS algorithm constructs a subset $P_N = \{p_i\}_{i=1}^{N}$ as follows:

1. Choose an initial index j_0 uniformly from $\{1, \dots, M\}$ and set $p_1 = c_{j_0}$.
2. For $k = 1, \dots, N-1$:

- For each candidate c_j, compute its squared distance to the current chosen set $S_k = \{p_1, \dots, p_k\}$,

$$d^2(c_j, S_k) = \min_{p \in S_k} \|c_j - p\|_2^2$$

- Select

$$j_{k+1} = \arg\max_{1 \le j \le M} d^2(c_j, S_k)$$

and set $p_{k+1} = c_{j_{k+1}}$.

By repeatedly choosing the candidate point that maximises its distance to the already selected set, FPS produces a point cloud with relatively uniform inter-point distances.

Boundary augmentation

For improved global stability of the interpolation scheme, we systematically augment the interior samples with points on the domain boundary $\partial\Omega$. For a given integer $n_b \ge 2$, we define equidistant nodes

$$x_i = \frac{i}{n_b - 1}, i = 0, \dots, n_b - 1, y_j = \frac{j}{n_b - 1}, j = 0, \dots, n_b - 1,$$

and construct the sets

$$\Gamma_{\text{bottom}} = \{(x_i, 0) : i = 0, \dots, n_b - 1\}$$
$$\Gamma_{\text{top}} = \{(x_i, 1) : i = 0, \dots, n_b - 1\}$$
$$\Gamma_{\text{left}} = \{(0, y_j) : j = 0, \dots, n_b - 1\}$$
$$\Gamma_{\text{right}} = \{(1, y_j) : j = 0, \dots, n_b - 1\}$$

Together with the four corners $(0,0), (1,0), (0,1)$ and $(1,1)$, the boundary set is

$$B = \Gamma_{\text{bottom}} \cup \Gamma_{\text{top}} \cup \Gamma_{\text{left}} \cup \Gamma_{\text{right}} \cup \{(0,0), (1,0), (0,1), (1,1)\}$$

Given any interior point cloud $P \subset \Omega$, the augmented set is

$$Q = P \cup B$$

To avoid numerical artefacts due to nearly identical points, we merge points in Q that are closer than a small tolerance $\tau > 0$; this is implemented by rounding the coordinates to a prescribed number of digits and retaining unique rows.

If the augmented set Q contains more than N points, we apply a farthest point selection step (as above) to subsample Q down to N nodes while preserving good coverage of both the interior and the boundary.

Gradient-based adaptive sampling

To concentrate samples in regions where f exhibits large variations, we construct an adaptive strategy based on the magnitude of the gradient ∇f. The method proceeds in two steps [9].

Candidate cloud and gradient approximation. Given a target number of points N and a mixing parameter $\gamma \in (0,1)$, we choose

$$M = \max(30N, 5000)$$

candidate points $C = \{c_j\}_{j=1}^{M}$ uniformly in Ω. For each candidate $c_j = (x_j, y_j)$ we approximate the gradient using central finite differences with step size $h > 0$:

$$f_x(x_j, y_j) \approx \frac{f(x_j + h, y_j) - f(x_j - h, y_j)}{2h},$$
$$f_y(x_j, y_j) \approx \frac{f(x_j, y_j + h) - f(x_j, y_j - h)}{2h},$$

where the arguments are projected back to [0,1] if necessary. The gradient magnitude is then

$$g_j = \sqrt{f_x(x_j, y_j)^2 + f_y(x_j, y_j)^2}.$$

Probability distribution and sampling. We define a discrete probability distribution on the candidate set by

$$p_j = \frac{g_j + \varepsilon_0}{\sum_{k=1}^{M} (g_k + \varepsilon_0)}, j = 1, \dots, M,$$

where $\varepsilon_0 > 0$ is a small constant ensuring positivity. We then choose

$$N_{\text{ad}} = \lfloor (1 - \gamma) N \rfloor$$

points from C without replacement according to the probabilities $\{p_j\}$, and generate the remaining

$$N_{\text{un}} = N - N_{\text{ad}}$$

The final adaptive point set is the union of the gradient-weighted and uniform samples:

$$P_N^{\text{ad}} = \{c_{j_1}, \dots, c_{j_{N_{\text{ad}}}}\} \cup \{\tilde{c}_1, \dots, \tilde{c}_{N_{\text{un}}}\}.$$

By construction, regions with large $|\nabla f|$ receive more samples, while a fraction of uniformly distributed points preserves global coverage of the domain.

2.1.3 Unified training set construction

Given a prescribed sampling type

kind $\in$ { "uniform", "lhs", "blue", "adaptive" },

and a target size N_{train}, we define the training point set X_{train} as follows:

- If kind = "uniform", take N_{train} i.i.d. uniform samples in Ω.
- If kind = "lhs", construct an LHS design with N_{train} points as above.
- If kind = "blue", apply farthest point sampling (FPS) to obtain N_{train} blue-noise points in Ω.
- If kind = "adaptive", construct an adaptive point set based on the gradient magnitude of f as described above.

In all cases, we optionally augment the interior points with boundary nodes and, if necessary, downsample the combined set by FPS to obtain exactly N_{train} points. The corresponding training data are then

$$X_{\text{train}} = \{x_i\}_{i=1}^{N_{\text{train}}}, y_i = f(x_i), i = 1, \dots, N_{\text{train}}$$

For evaluation and visualisation, we also introduce a regular tensor-product grid of size $n_g \times n_g$,

$$G = \{(x_i^{\text{test}}, y_j^{\text{test}})\}_{i,j=1}^{n_g} \subset \Omega$$

on which the reference values $f\left(x_i^{\text{test}}, y_j^{\text{test}}\right)$ are computed. This grid is used to quantify the interpolation errors and to produce contour and surface plots of the true and reconstructed fields.

Numerical Experiments.

To rigorously evaluate the effectiveness of the proposed RBF–based interpolation framework, we conduct a systematic comparison against the multivariate polynomial interpolation scheme implemented in the MINTERPY package [7], [4]. MINTERPY generates global polynomial approximants using algebraic multi–index sets and unisolvent node configurations, whereas the proposed method employs radial basis functions enhanced through whitening transformations, nearest–neighbor length–scale normalization, and cross–validated selection of kernel types and shape parameters. Both approaches are applied to the same benchmark function under identical sampling conditions, enabling a direct and unbiased assessment of reconstruction accuracy, numerical stability, and sensitivity to sampling density and geometric complexity. The comparative study focuses on the error norms(L_1, L_2, L_∞) [11] computed over a dense evaluation grid. The results indicate that the RBF model consistently achieves higher accuracy in regions characterized by sharp anisotropy, steep gradients, and non–polynomial behavior, whereas MINTERPY performs competitively on smooth components that exhibit near–global polynomial structure.

All numerical experiments are carried out using Latin Hypercube Sampling on the unit square $[0,1]^2$. To analyze the impact of sample density, we consider three training set sizes: $N = 100, N = 500$, and $N = 1000$. For each configuration, we compute interpolation errors using the aforementioned norms and summarize the results in corresponding comparative tables, thereby elucidating how accuracy scales with increasing dataset resolution.

- **For $N = 100$**

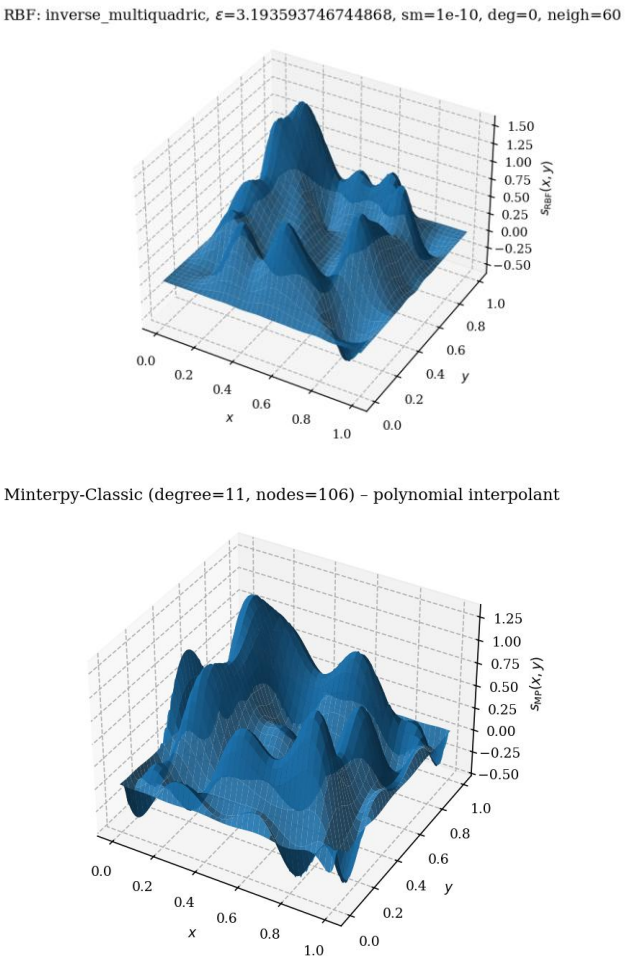


Figure 3. *Comparison of the reconstructed surface using the proposed RBF interpolation method and the MINTERPY polynomial interpolation scheme for N=100 training points.*

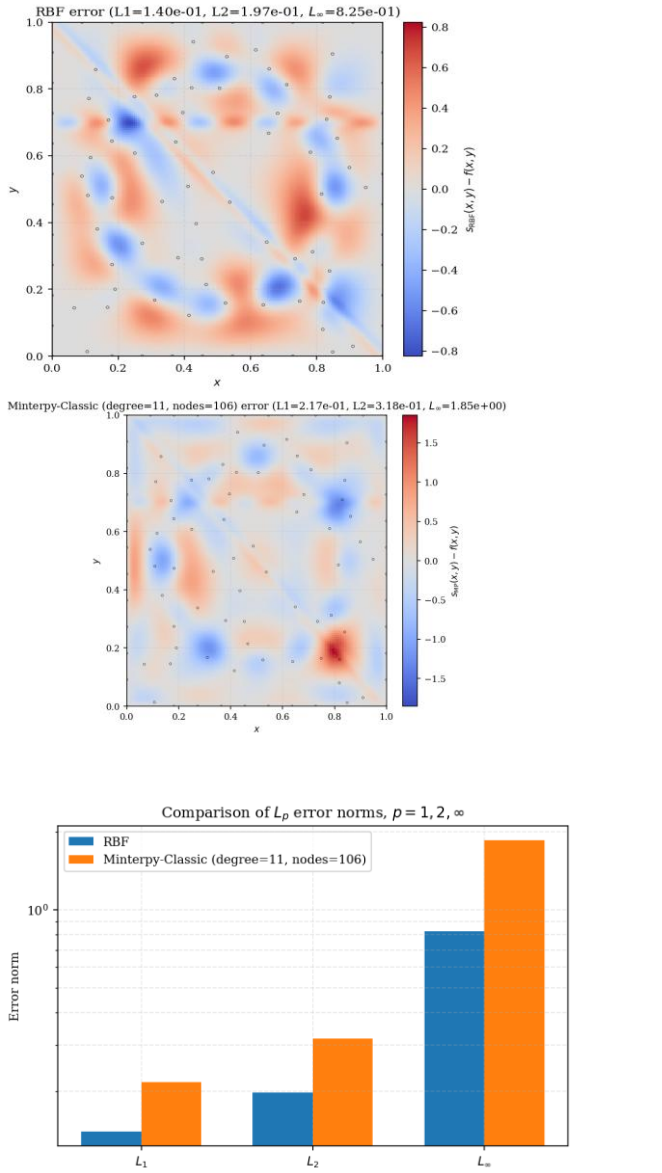


Figure 4. Evaluation of interpolation accuracy based on (L_1, L_2, L_∞) norms.

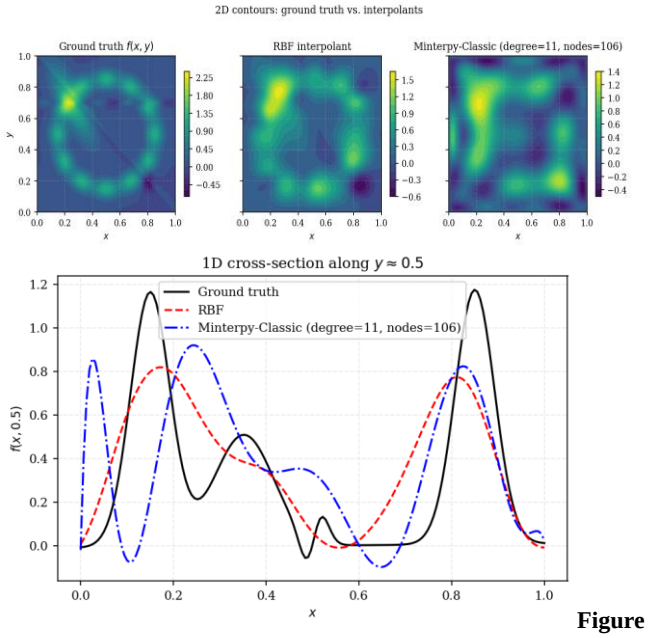


Figure 5. 1D cross–section comparison along y≈0.5 between the ground truth function, the RBF reconstruction, and the MINTERPY polynomial interpolant.

Method	L_1	L_2	L_∞
RBF	$1.397e-01$	$1.967e-01$	$8.251e-01$
Minterpy	$2.167e-01$	$3.183e-01$	$1.853e+00$

Tabela 1: Error norms for the two interpolation methods.

- **For N=500**

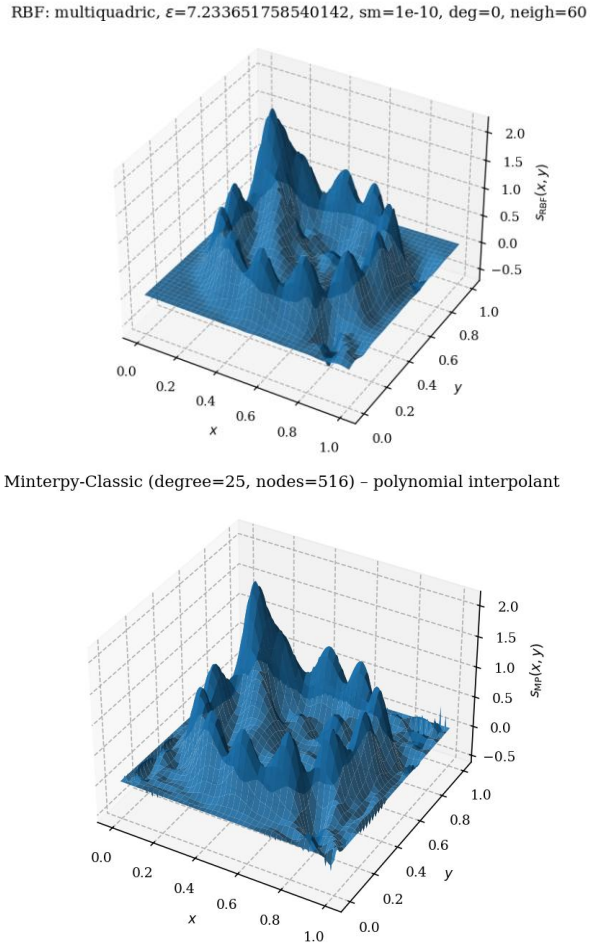
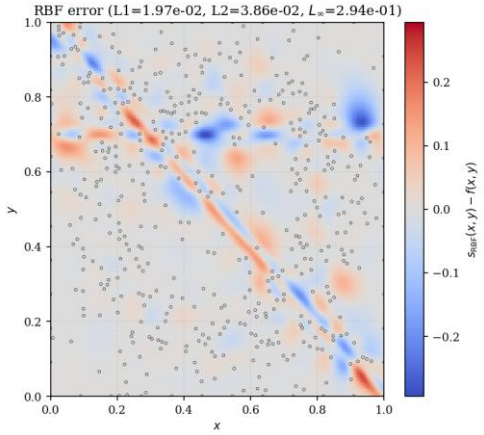


Figure 6. *Comparison of the reconstructed surface using the proposed RBF interpolation method and the MINTERPY polynomial interpolation scheme for N=500 training points.*



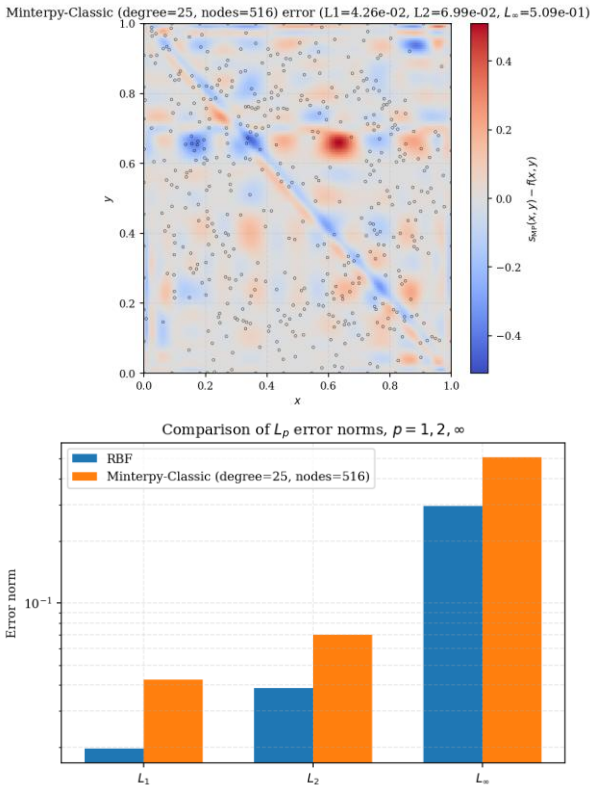


Figure 7. Evaluation of interpolation accuracy based on (L_1, L_2, L_∞) norms.

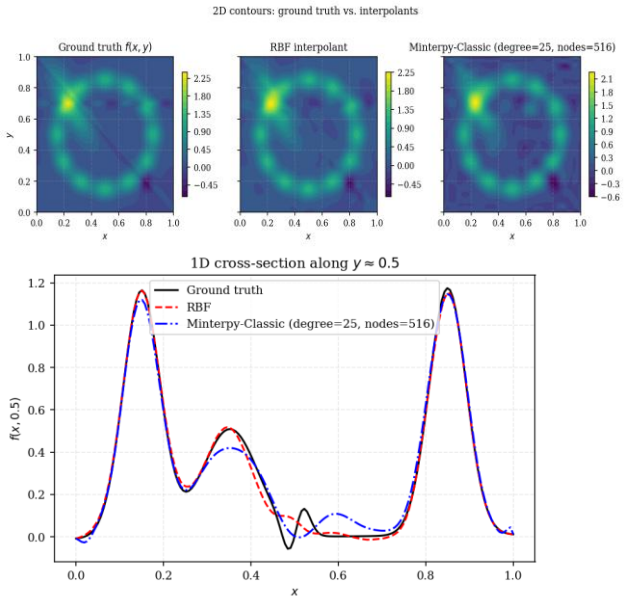


Figure 8. 1D cross–section comparison along y≈0.5 between the ground truth function, the RBF reconstruction, and the MINTERPY polynomial interpolant (N=500).

Method	L_1	L_2	L_∞
RBF	$1.972e-02$	$3864e-02$	$2943e-01$
Minterpy	$4.264-02$	$6.993e-02$	$5.094e-01$

Tabela 2: Error norms for the two interpolation methods.

- For N=1000

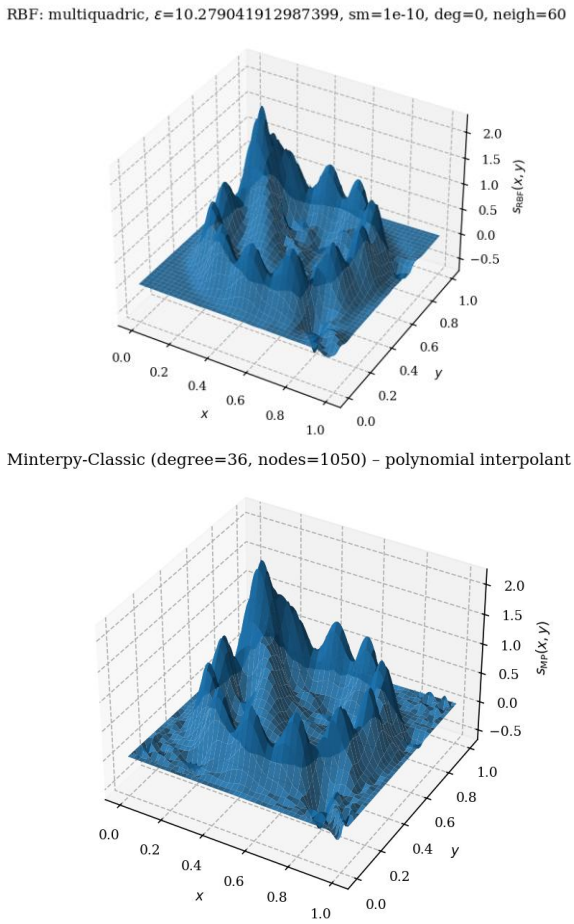
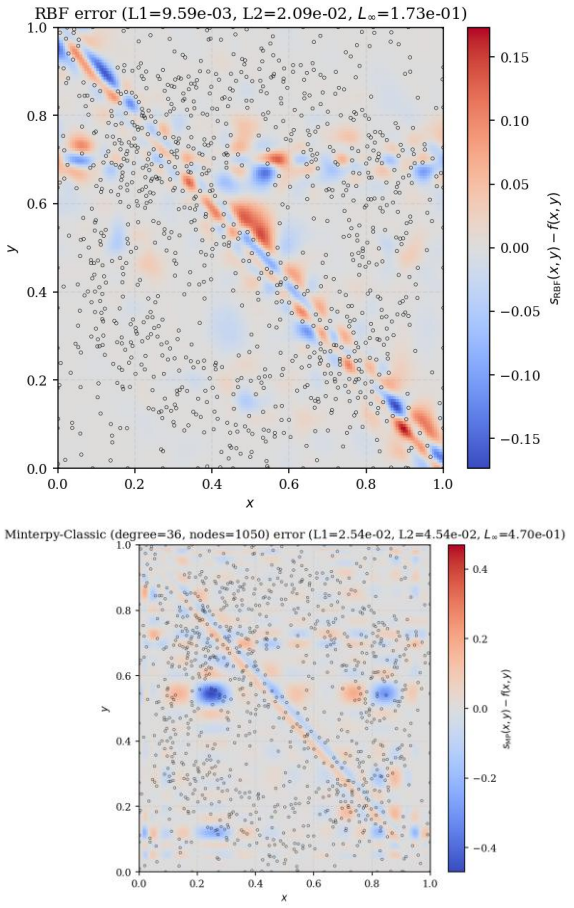


Figure 9. *Comparison of the reconstructed surface using the proposed RBF interpolation method and the MINTERPY polynomial interpolation scheme for N=500 training points.*



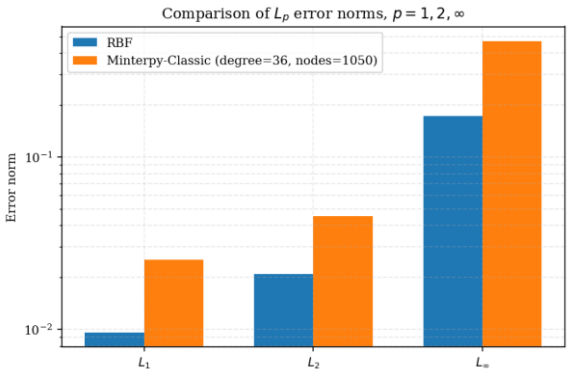


Figure 10. Evaluation of interpolation accuracy based on (L_1, L_2, L_∞) norms.

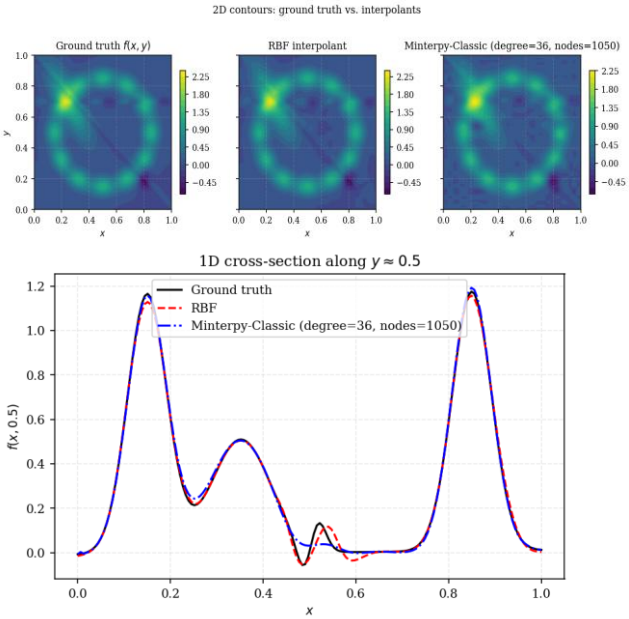


Figure 8. 1D cross–section comparison along y≈0.5 between the ground truth function, the RBF reconstruction, and the MINTERPY polynomial interpolant (N=1000).

Method	L_1	L_2	L_∞
RBF	$9.5952e-03$	$2.090e-02$	$1.734e-01$
Minterpy	$2.537-02$	$4.538e-02$	$4.696e-01$

Tabela 3: Error norms for the two interpolation methods.

Conclusion

In this work, we presented a stability–enhanced RBF interpolation framework designed to improve numerical robustness and accuracy when reconstructing complex multivariate functions on the domain$[0,1]^2$ By integrating whitening transformations, nearest–neighbour length–scale normalization, and cross–validated selection of kernel and shape parameters, the method addresses several well–known challenges of classical RBF schemes, including sensitivity to scale, instability at small shape parameters, and inconsistent performance under irregular sampling. Comparative numerical experiments demonstrated that the proposed method consistently outperforms the polynomial interpolation approach implemented in the MINTERPY library, particularly in regions characterized by high anisotropy, sharp gradients, and non–polynomial behaviour.

While MINTERPY remains competitive on globally smooth components due to its algebraic basis construction, the RBF method exhibits superior adaptability across heterogeneous geometric features. These findings indicate that hybrid strategies combining global polynomial structure with locally adaptive radial models may offer further improvements, especially for high–dimensional data or manifold- based geometries.

Future work will focus on extending the proposed approach in three directions:

1. **Adaptive multi–resolution refinement**, where sampling density and kernel parameters evolve dynamically according to local error indicators.
2. **Hybrid RBF–polynomial formulations**, designed to balance global smoothness with local feature resolution while reducing computational cost.
3. **Generalization to non–Euclidean manifolds and implicit geometric representations**, particularly in the context of level–set modelling, surface deformation, and PDE–driven simulations.

Overall, the proposed framework provides a promising step toward more stable, scalable, and high- fidelity numerical interpolation methods, with direct applicability to scientific computing, geometric modelling, and data–driven physical simulation.

References:

[1] Fasshauer, G., 2007. Meshfree Approximation Methods with Matlab. World Scientific Publishing Co.,Pages 53-61.
[2] M. D. McKay, R. J. Beckman and W. J. Conover ,A Comparison of Three Methods for Selecting Values of Input Variables in the Analysis of Output from a Computer Code,Source: Technometrics, Vol. 21, No. 2 (May, 1979), pp. 239-245 https://doi.org/10.2307/1268522
[3] Yuval Eldar, Michael Lindenbaum, Member, IEEE, Moshe Porat, Senior Member, IEEE, and Yehoshua Y. Zeevi, The Farthest Point Strategy for Progressive Image Sampling https://doi.org/10.1080/10789669.2009.10390836
[4] U. HERNANDEZ ACOSTA, S. KRISHNAN THEKKE VEETTIL, D. WICAKSONO, AND M. HECHT, MINTERPY - multivariate interpolation in python, https://github.com/casus/minterpy/, (2021).
[5] Buhmann, M. D. (2003).Radial Basis Functions: Theory and Implementations, Cambridge University Press.
[6] Kessy, A., Lewin, A., & Strimmer, K. (2018). Optimal whitening and decorrelation https://doi.org/10.48550/arXiv.1512.00809
[7] HECHT, M., HOFFMANN, K. B., CHEESEMAN, B. L. & SBALZARINI, I. F. (2018) Multivariate Newton interpolation. arXiv preprint arXiv:1812.04256.
[8] Wendland, H. (2005).*Scattered Data Approximation* Cambridge University Press.
[9] Strikwerda, J. C. (2004) *Finite Difference Schemes and Partial Differential Equations* SIAM.
[10] Stone, M. (1974) Cross-Validatory Choice and Assessment of Statistical Predictions. Journal of the Royal Statistical Society: Series B (Methodological), 36, 111-147.
[11] Kreyszig, E. (1978) *Introductory Functional Analysis with Applications* Wiley.

Modelling of LTL routes for eco-diversed transport application

Radosław Belka[1,*], Wojciech Belka[1]
Kielce University of Technology, Poland[1]
r.belka@tu.kielce.pl[*]

Abstract:
This study addresses the vehicle routing problem (VRP) for eco-diverse transport fleets, defined as fleets comprising vehicles with heterogeneous engine systems, resulting in varied payload capacities, access restrictions, and levels of cost-efficiency and environmental performance. The research is driven by the growing integration of alternative fuel vehicles (e.g., electric and hydrogen-powered) into conventional transport fleets, coupled with the implementation of Clean Transport Zones (EcoZones) that impose access restrictions on combustion (diesel) vehicles. A two-stage, highly scalable bi-objective optimization algorithm is proposed, evaluated using a real-world case study involving the distribution of 356 pallets across 188 destinations within an approximate 140 km radius of Kielce, with 25% of these destinations located in potential EcoZone areas. The analysis assesses feasibility, ecological and economic cost intensity, and workload distribution across fleet segments under energy and access constraints. The developed algorithm demonstrates significant potential for prescriptive analytics in optimizing routing strategies amid the energy transition in the transportation sector.

KEYWORDS: *ECO-DIVERSE FLEET, LTL TRANSPORT, VRP, MULTI-OBJECTIVE OPTIMIZATION, ITERATED LOCAL SEARCH, SIMULATED ANNEALING*

1. Introduction

The transportation sector is undergoing a profound transformation, driven by the need to enhance sustainability while maintaining operational efficiency. This shift necessitates innovative approaches to the management, coordination, and performance evaluation of vehicle utilization. A key challenge in this domain is optimizing less-than-truckload (LTL) transport, where cost efficiency is achieved through advanced routing strategies and sophisticated algorithms [1]. These strategies aim to develop feasible, cost-effective, and environmentally sustainable route plans that balance economic and ecological objectives, as exemplified by the Pollution-Routing Problem (PRP) or Green Vehicle Routing Problem (Green VRP) [2,3]. Over recent decades, the Vehicle Routing Problem (VRP) has been extensively studied, giving rise to several variants, including the Capacitated VRP [4], the Time-Windowed VRP [5], and the Multi-Depot VRP [6]. The increasing diversity in order volumes and customer requirements has spurred the adoption of heterogeneous fleets, which combine vehicles with varying capacities and characteristics to meet operator's demands [7,8]. In recent years, the integration of electric vehicles (EVs) into VRP frameworks has gained significant attention [9–12]. These studies introduce additional constraints, related to the limited energy capacity of EVs, which necessitates innovative solutions such as incorporating full or partial battery charging into route planning to mitigate range limitations [13]. Alternatively, scheduled battery-swapping procedures have been proposed as a viable approach to enhance operational feasibility [14,15]. A particularly promising strategy is the mixed (eco-diversed) fleet approach, which combines conventional diesel vehicles with eco-friendly battery electric vehicles (BEVs) [16]. This approach offers a pragmatic solution, aligning with global imperatives to reduce greenhouse gas emissions while preserving fleet transport capacity.

This study concentrates on the field of sustainable transportation by developing and evaluating optimized routing strategies for mixed-fleet operations. The primary contribution lies in the design and implementation of a prototype fleet management system that integrates a novel planning–optimization module tailored for eco-diverse fleets. This module employs a bi-objective optimization algorithm with an inter-criteria balancing function, enabling the identification of routing solutions that are feasible under energy and access constraints while minimizing both economic costs and negative environmental impact. To demonstrate the practical applicability of the proposed system, the study conducts a comprehensive analysis using a real-world case study involving the distribution of 356 pallets across 188 destinations. The analysis evaluates key performance metrics, including feasibility, ecological and economic cost intensity, and workload distribution segments, as functions of imposed energy constraints and access restrictions (e.g. EcoZones). By quantifying the trade-offs between economic and environmental objectives, this work provides actionable insights for logistics operators seeking to transition to sustainable fleet management practices.

2. Optimization Algorithm and Model

The analysis of routing strategies for eco-diverse heterogeneous resources was carried out using a proprietary planning algorithm developed within the research and development project TRAFFIC (Towards Route Autoplanning for Eco-diverse Fleet and Flow Management with Improved Coordination). The TRAFFIC system is primarily intended for companies providing LTL transport services in the context of deterministic delivery and demand scenarios. To solve the routing problem, a custom two-stage algorithm was applied, combining a pseudo-greedy heuristic of the Nearest Neighbour (NN) type [17] with an evolutionary Iterated Local Search (ILS) metaheuristic [18].

The general structure of the method is shown in Fig. 1. The algorithm assigns orders from the *Requests* list to the resource base stored in *TruckList*, using sets of inter-distance, inter-time, and eco-distance matrices, along with the characteristics of the destination list *DestPos*.

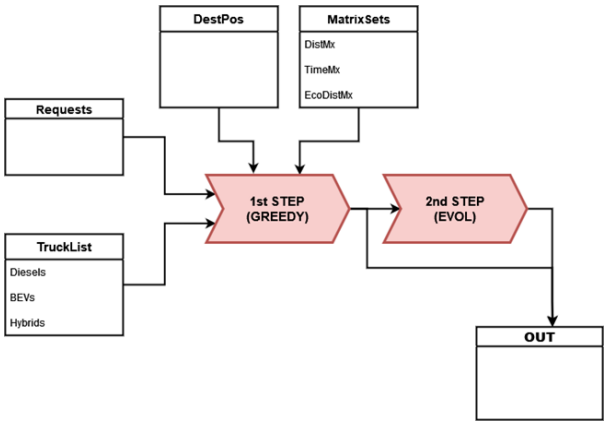


Fig. 1. Structure of the planning algorithm

The first stage of the planning algorithm (GREEDY) is deterministic in nature and is responsible for generating an initial, feasible, and quasi-optimal solution, by default engaging the smallest possible number of transport resources. In the second phase of the optimization procedure, a proprietary algorithm named EVOL was applied, based on iterated random mutations of feasible solutions. The primary optimization criterion of the EVOL phase is a generalized monetary cost function, defined as the sum of three components: the fixed cost associated with engaging a vehicle, the time-related cost, and the energy-related cos. The monetary cost generated by the i-th resource (vehicle) is expressed by Equation 1.

$$c_i = c^F{}_i + t_i \cdot u^h{}_i + e_i \cdot u^e{}_i \quad (1)$$

where:
c_i - total cost of the i-th resource
$c^F{}_i$ - fixed cost of the i-th resource
$u^h{}_i$, $u^e{}_i$ - unit monetary costs for Staff and Energy, respectively
t_i – total time engagement of the iii-th resource
e_i represents the energy resources consumed by the i-th resource.

In the developed model, it is calculated based on the traveled distance d and the required time t, taking into account the load weight of the resource (Equation 2).

$$e_i = \sum_{k\in\tau_i}\left[d_{i,k} \cdot \left(\beta^c{}_i + \beta^v{}_i \cdot m_{i,k}\right) + t_{i,k} \cdot \beta^t{}_i\right] \quad (2)$$

where:
τ_i – route of the i-th resource
$\beta^c{}_i, \beta^v{}_i, \beta^t{}_i$ - unit costs (energy consumption per unit length, mass, and time)
$m_{i,k}$ - load of resource i at the k-th point of the route
$d_{i,k}, t_{i,k}$ - distance and time to cover the k-th segment of the route

The consumption of energy resources e_i simultaneously affects the value of the so-called ecological cost, which becomes an additional, independently treated optimization criterion. Ultimately, the developed optimization algorithm is guided by the criteria of minimizing both monetary cost and ecological cost:

$$min \sum_{i\in\Pi} c_i \qquad min \sum_{i\in\Pi} e_i \cdot u^c{}_i \quad (3)$$

where: Π – the set of resources, $u^c{}_i$ - the unit ecological cost (CO_2 emissions per unit of energy).
The following constraints are imposed on the set of routes τ_i regarding total mass (MassLimit), volume (VolLimit), energy consumed (EnergyLimit), allowable resource activity time (MaxActivityTime), and maximum time of a single trip (MaxTripTime).

$$\bigwedge_{i\in\Pi} \sum_{k\in\tau_i} m_{i,k} < MassLimit_i \quad (4a)$$

$$\bigwedge_{i\in\Pi} \sum_{k\in\tau_i} v_{i,k} < VolLimit_i \quad (4b)$$

$$\bigwedge_{i\in\Pi} e_i < EnergyLimit_i \quad (4c)$$

$$\bigwedge_{i\in\Pi} t_i < MaxActivityTime_i \quad (4d)$$

$$\bigwedge_{i\in\Pi} \bigwedge_{j\in\tau^p{}_{i,j}} \sum_{k\in\tau^p{}_{i,j}} t_{j,k} < MaxTripTime_i \quad (4e)$$

where: $\tau^p{}_{i,j}$ - a single trip performed by the i-th resource
In the presence of EcoZone Θ_e an additional condition is a restriction on access for vehicles that do not meet the criteria. This means that each point k of the route τ_i must be accessible by a resource belonging to the set Π_e of eco-friendly vehicles.

$$\bigwedge_{k\in\tau_i,\Theta_e} i \in \Pi_e \quad (5)$$

The EVOL algorithm also incorporates the concept of simulated annealing [15], which involves conditionally accepting mutations characterized by a negative threshold, whose value is relaxed to zero during the evolution process. The algorithm performs a specified number of MaxIters iterations. The acceptance criterion (Acc) for the considered criterion in the current iteration *iter* is expressed by the following formula:

$$Acc(iter) = \begin{cases} 1 \;\; if\; \Delta c < s_0 \cdot \left(1 - \frac{iter}{MaxIters}\right)^2 \cdot R_{iter} \\ 0 \qquad\qquad otherwise \end{cases} \quad (6)$$

where:
s_0 - initial relative acceptance threshold,
Δc – cost change in the current iteration
R_{iter} – reference threshold, dynamically updated according to the formula:

$$R_{iter} = \rho \cdot |\Delta c_{iter}| + (1-\rho) \cdot R_{iter-1} \quad (7)$$

ρ – exponential filter coefficient.

In general, the algorithm is guided by a two-criteria cost measure, with independent acceptance conditions determined for each criterion (economic and ecological). To make the algorithm more flexible, the concept of probabilistic relaxation of conditions was introduced, represented by the *balance* coefficient, which belongs to interval <0–1>. The determination of the acceptance condition (*TotAcc*) in the weighted bi-criteria variant is calculated according to the general formula (8).

$$TotAcc = (Acc1 \vee rnd(1) < w_1) \wedge (Acc2 \vee rnd(1) < w_2) \quad (8)$$

where: *Acc* – a binary variable defining whether a given criterion is met, *rnd(1)* – a randomly selected number from the range 0–1, and w_1 and w_2 are determined from the value of *balance*. When *balance* = 0, the ecological criterion is always accepted; in this case, the algorithm operates under single-criterion optimization conditions (SOCO – Single Objective Combinatorial Optimization). When balance = 0.5, a mutation is accepted only if the both Acc are simultaneously satisfied, and the algorithm operates in the bi-criteria regime (BOCO – Bi-Objective Combinatorial Optimization).

The planning algorithm was implemented in Mathcad PRIME 8.0. Analyses were carried out on an MSI NoteBook, model MS179F, equipped with an Intel(R) Core(TM) i7-8750H CPU @ 2.20GHz and 8 GB RAM.

3. Results and discussion

3.1. Case description

The considered model case for the routing strategy assumes the delivery of 356 pallets to 188 destinations using a capacity-homogeneous, eco-diverse fleet. The order parameters are presented in Table 1.

Table 1. General characteristics of orders

Parametr	
Number of destinations	188
Average distance from base to destination	58.7km
Max. distance from base to destination	138.8km
Total order volume	356 pallets
Size of a single order	1 – 4 pallets
Average order volume	~1.9 pallets
Volume to eco-zones	89 pallets (25%)
Weight of a single pallet	400kg

The order size ranges from 1 to 4 pallets, with 25% of the orders directed to the EcoZone area. The destinations are dispersed over an area of nearly 50,000 km², with a certain tendency toward natural clustering. The maximum distance from the depot to a destination was 138 km, the minimum was less than 1 km, and the average distance was approximately 57 km. Real distance and travel time parameters were obtained from geographic information systems in the manner presented in [19]. In the considered case, the presence of two types of vehicles with identical transport capacities was assumed, differing in the type of drive: Diesel and BEV – Table 2. The parameters of energy resource consumption were estimated based on vehicle manufacturers' data, own observations, and observations from transport companies carried out within the TRAFFIC project.

Table 2. General characteristics of vehicles

Parameter	Diesel	BEV (Mixed1	BEV (Mixed2)
Trucks	28	12	
EnergyLimit	100 dm^3	100 kWh	200 kWh
MaxTripTime	8 h		6 h
InterTrip Time	0.5 h		2.5 h
$\beta^c{}_i$,	10 dm^3/100km	35 kWh/100km	
$\beta^v{}_i$,	1.3 dm^3/100km/t	4.5 kWh/100km/t	
$\beta^t{}_i$	1 dm^3/1h	3.5 kWh/1h	
u^e	1.5 Euro/ dm^3	0.5 Euro/kWh	
c^F	50 Euro	75 Euro	
u^c	2.5 kg/ dm^3	0.25 kg/kWh	
u^h	10 Euro/h		
VolLimit	10 pallets		
MassLimit	10Mg		
MaxActivityTime	12h		
LoadUnit Time	6 min/pallete		

The parameter values indicate a clearly higher economic cost and, at the same time, a lower ecological cost for the BEV segment. Two cases differing in the ability to replenish energy resources were analyzed. In the Mixed1 case, it was assumed that recharging during the MaxActivity Time is not possible. In the Mixed2 case, it was assumed that a one-time replenishment of energy resources is possible, which translates into a twofold increase in the energy resource limit, a reduction of the maximum trip duration (MaxTripTime) by 2 hours, and an increase in InterTrip Time by 2 hours respectively.

3.2. Migration to ecodiversed fleet

It was demonstrated that neither a fully combustion-engine fleet nor a fully electric fleet is capable of fulfilling all orders. In the case of the combustion-engine fleet, 25% of orders were not serviced due to the presence of clean transport zones. In the case of the fully electric fleet, approximately 7.6% of the order volume was not serviced due to excessive distance from the base to the destination. Full order coverage, however, is ensured by an eco-diverse fleet. In the further part of the study, a hypothetical reference case (Diesel-Only) was also considered, involving only a traditional fleet under conditions without the EcoZones.

Table 3 presents the calculated cost-intensity and energy-intensity parameters of the solutions for the Mixed1 and Mixed2 fleets, compared to the reference case (Diesel-Only). The differences in terms of total distance traveled, time-intensity, and the number of required trips for each of the three cases are statistically insignificant. Therefore, distance is not a reliable parameter for differentiating between the analyzed cases. As a result, the differences in cost-intensity of the solutions are mainly due to differences in the Fix Cost of fleet maintenance.

Table 3. Cost-intensity and energy-intensity parameters of the solutions for the respective fleet variants.

PARAMETER	Diesel-Only	Mixed1	Mixed2
Total Distance [km]	5311.22	5323.70	5308.24
Total Monetary Cost [euro]	3431.83	3716.22	3657.03
Energy Cost [euro]	1152.61	1189.44	1185.10
Staff Cost [euro	1489.22	1489.29	1486.93
Fix Cost [euro]	790	1037.5	985
Total Fleet Volumen [pallets]	158	177	172
Trips	36	36.2	36.2
Total Activity Time [h]	159.02	158.18	159.99
CO2 emmision [kg]	1921.01	1689.93	1684.99
Trucks needed	16	18	17-18

The transition to an eco-diverse fleet may require equipping it with a set of at least 6 BEV-type vehicles, while reducing the number of traditional vehicles by up to 4. Under conditions allowing recharging, the minimum number of BEV-type vehicles is 5. The analysis shows that migration to eco-diverse fleets is associated with an approximately 31% increase in fixed costs in the case of Mixed1 and about 25% in the case of Mixed2. At the same time, this leads to a reduction in CO_2 emissions of around 12%.

Subsequently, the activity time of individual resources (Truck Activity Time), resulting from the generated route plan, was analyzed. The load includes transshipment time as well as potential BEV vehicle recharging. The load of the reference fleet's vehicles (Diesel-Only) ranges from 7.4 to 11.77 hours – Fig. 2. In the case of the Mixed1 fleet, a noticeably lower load of the BEV segment is observed – an average vehicle of this type was engaged for only 5.8 hours, which is a consequence of limiting energy resources to 100 kWh.

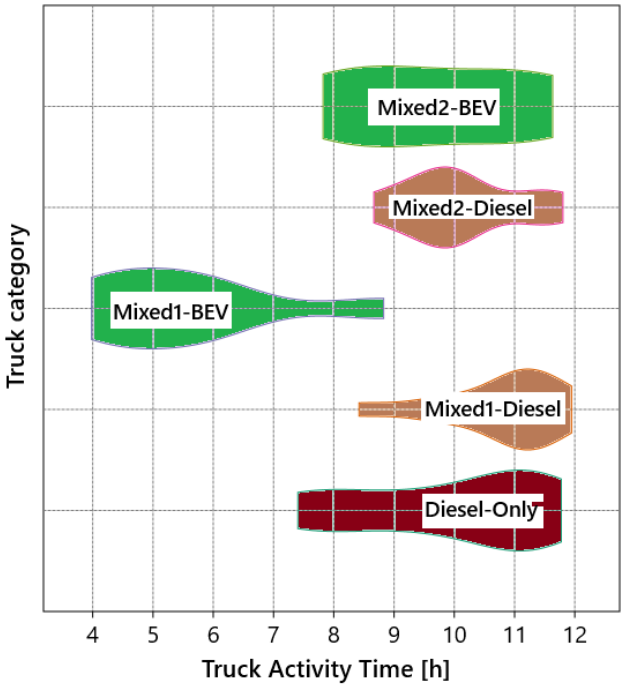


Fig. 2. Activity time of individual resource categories in the respective fleet variants

Under conditions allowing recharging, the activity of vehicles does not differ from the engagement level of the combustion-engine segment. A significant reduction (from 61 to 50 pallets) in the required total average volume of the BEV segment was observed. At the same time, no statistically significant difference was noted between the Mixed1 and Mixed2 fleets in terms of distance traveled, energy cost, or total cost. However, the benefits resulting from the reduction of fleet resources are offset by the increased fleet activity time (higher labor cost) caused by the time-consuming charging process.

3.3. Participation of the BEV segment in transport service delivery – SOCO vs. BOCO optimization

The participation of the BEV segment in the Mixed1 and Mixed2 fleets was analyzed in relation to various planning solution parameters, including the percentage of serviced orders, share in operating costs, distance traveled, and process time intensity. A series of routing optimizations was carried out in a single-criterion variant (monetary cost – SOCO) and a dual-criterion variant (monetary cost and CO_2 emissions – BOCO). The results are shown in Figure 3.

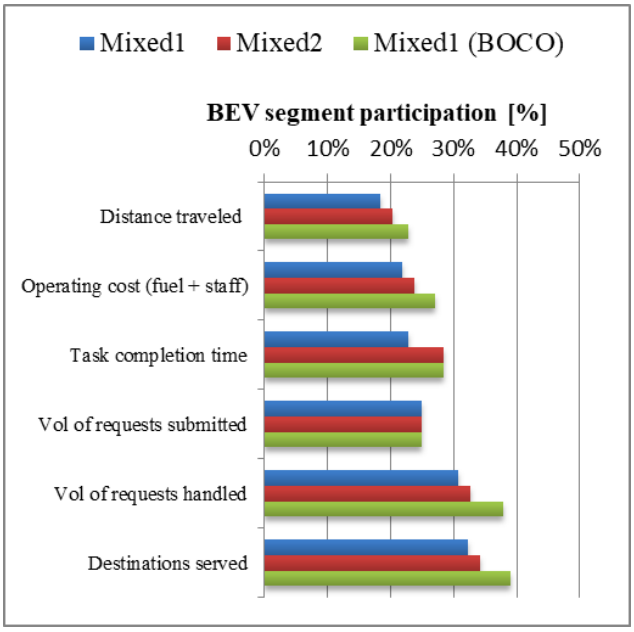


Fig. 3. Participation of the BEV segment in various planning solution parameters

In terms of the volume of serviced orders and visited destinations, the share of the BEV segment was clearly greater than that resulting from the share of the EcoZone. In the BOCO variant, electric vehicles serviced approximately 39% of destinations and delivered 135 out of 356 pallets (37.7%). This results from the optimization algorithm's tendency to minimize ecological cost, which favors BEV-type vehicles. In this latter case, 7 out of 12 (nearly 60%) deployed BEV vehicles were used, whereas Diesel vehicle utilization amounted to no more than 12 out of 28 (just over 40%). On the other hand, the BEV vehicles' share in the total distance traveled was relatively small. In the case of the Mixed1 fleet, these vehicles covered only about 18.4% of the total distance, while their share of the transport volume was over 34%. This is related to the imposed limitations on energy resources, which forces the algorithm to assign BEV vehicles to trips involving destinations located closer to the starting point (depot).

4. Conclusion

The study presented a detailed analysis of the costs of eco-diverse mixed fleets operating in a less-than-truckload transport regime. The analysis was conducted for a representative case of delivering 356 pallets to 188 delivery points, subject to access restrictions resulting from local conditions and the hypothetical location of so-called clean transport zones. It was shown that mixing the fleet may be a necessary requirement to achieve 100% capability to meet transport demands. In the considered case, full replacement of the combustion-engine fleet with a mixed fleet led to an increase in transport service cost of approximately 8.3%, resulting mainly from the higher purchase and maintenance costs of electric vehicles. No significant increase was observed in staff costs or energy costs. On the other hand, CO_2 emissions were reduced.

5. Acknowledgements

This research was founded by the European Union's Smart Growth Operational Programme 2014-2020, under grant agreement no POIR.01.01.01-00-0110/22 "Autonomous coordinator of eco-diverse transport assets"

6. References

1. G. Soleilhac, F. Lehuédé, J. Medina, O. Péton, IMT Atlantique, Département Automatique, Productique et Informatique, 44300 Nantes Cedex 3 (2022), hal-03860741
2. T. Bektaş, G. Laporte, Trans Res B: Methodological **45 (8),** (2011) p.1232
3. S. Erdoğan. E. Miller-Hooks, Trans Res E: Logistics and Transportation Review **48 (1)** (2012) p.100
4. R. Bernardino, A. Paias, Euro J Oper Res **314 (3),** 2024, p.836
5. J. Bramel, D. Simchi-Levi, Springer Series in Operations Research. Springer, New York, NY (1997)
6. N. Aras, D. Aksen, M. T. Tekin, Trans Res C: Emerging Technologies **19 (5)** (2011)
7. I.M. Chao, B.L. Golden, E.A. Wasil,. Operations Research/Computer Science Interfaces Series 9, Springer, Boston, MA (1997)
8. B.S. Vieira, G.M. Ribeiro, L. Bahiense (2023), Computers & Oper Res **153** (2023) p.106189,
9. J. Lin, W. Zhou, O. Wolfson, Trans Res Procedia **12** (2016) p.508
10. I. Kucukoglu, R. Dewil, D. Cattrysse, Comp & Industrial Eng **61** (2021) p.107650,
11. H. Qin, X. Su, T. Ren, Z. Luo,. Front. Eng. Manag. **8(3)** (2021) p.370
12. Sh. Zhang, H. Zheng, J. Tian. J Indust and Management Optimization **21(2)** (2025)
13. J. Xiao, Sh. Wang, J. Xiao, George Q. Huang, Trans Res E: Logistics and Transportation Review **192** (2024) p.103838,
14. D. Wang, Z. Hong, Appl Sci **11** (22) (2021) p.10779.
15. V. F. Yu, H. Susanto, P. Jodiawan, T. W. Ho, S. W. Lin, Y. T. Huang, IEEE Access **10** (2022) p.20764
16. Á. Felipe, M. T. Ortuño, G. Righini, G. Tirado, Trans Res E: Logistics and Transportation Review **71**, (2014) p. 111
17. R. F. Harahap and Sawaluddin, J. Phys.: Conf. Ser. **2421**, (2023) p. 012027
18. Y. Wu, H. Du, H. Song. Mathematics, **12**, (2024) p. 1712.
19. Belka, R., Godlewski, M.. Appl Sci, **11(22)** (2021) p. 10933.

Isentropic and exergy analyses of turbomachines from co_2 supercritical power plant

Mrzljak Vedran[1], Prpić-Oršić Jasna[1], Baressi Šegota Sandi[1], Lorencin Ivan[2]
[1]Faculty of Engineering, University of Rijeka, Vukovarska 58, 51000 Rijeka, Croatia
[2]Faculty of Informatics, Juraj Dobrila University of Pula, 52100 Pula, Croatia
E-mail: vedran.mrzljak@riteh.uniri.hr, jasna.prpic.orsic@riteh.uniri.hr, sandi.segota@riteh.uniri.hr, ivan.lorencin@unipu.hr

Abstract: *The results of three turbomachines (one turbocompressor and two turbines) isentropic and exergy analyses, which operate in supercritical CO_2 power plant are presented in this paper. Both observed turbines (Turbine 1 and Turbine 2) have higher improvement potential than Turbocompressor. Mechanical losses in power transmission between Turbine 1 and Turbocompressor are equal to 456.57 kW in real operation process. Turbocompressor has the highest isentropic efficiency of 96.87% and the highest exergy efficiency of 97.61% if all observed turbomachines are considered. Turbine 2 used for the electric generator drive has higher efficiencies (both isentropic and exergy) in comparison to Turbine 1, regardless of higher isentropic loss and higher exergy destruction. Increase in the ambient temperature from 5 °C up to 45 °C decreases Turbocompressor exergy efficiency for 0.31%, while the same ambient temperature increase decreases exergy efficiency of both turbines for 0.53% (Turbine 1) and for 0.52% (Turbine 2).*

KEYWORDS: TURBOMACHINES, ISENTROPIC ANALYSIS, EXERGY ANALYSIS, CO_2, SUPERCRITICAL POWER PLANT

1. Introduction

Open-cycle gas turbine power plants have nowadays various applications in the energy sector (as independent plants, or in a combination with some other mechanical power producers) [1, 2]. Closed-cycle gas turbine power plants are not widely distributed as open-cycle gas turbine power plants, but they may have some interesting applications [3, 4]. In recent years, closed-cycle gas turbine power plants in various arrangements are often used as waste heat recovery systems in marine sector [5, 6].

It is well known from the literature that closed-cycle gas turbine power plants efficiency change is much lower at partial loads in comparison to open-cycle gas turbine power plants, what is one of their notable benefits [7]. Moreover, the produced mechanical power in closed-cycle gas turbine power plants can be easily regulated by changing operating fluid mass flow rate [8]. However, closed-cycle gas turbine power plants are usually much more complex in comparison to open-cycle gas turbine power plants, operating fluids used in closed-cycle gas turbine power plants are expensive and they are not always available in the market, etc., so it is obvious that closed-cycle gas turbine power plants also have some disadvantages in comparison to open-cycle gas turbine power plants.

In this paper are analyzed three turbomachines (one turbocompressor and two turbines) which operate in supercritical CO_2 power plant from the isentropic and exergy viewpoint. Efficiencies and losses (destructions) of all turbomachines are compared and the guidelines for possible improvements are presented. Moreover, it is performed analysis related to the ambient temperature change influence on each turbomachine exergy efficiency and destruction.

2. Description of the analyzed CO_2 supercritical power plant and its turbomachines

General scheme of the CO_2 supercritical power plant in which operates turbocompressor and both turbines analyzed in this paper is presented in Fig. 1.

CO_2 with the lowest temperature in the process enters in the Turbocompressor (operating point 1, Fig. 1). Turbocompressor increases CO_2 pressure (and simultaneously CO_2 temperature) and delivers it to the recuperator (operating point 2, Fig. 1). Recuperator is a counter flow CO_2-CO_2 heat exchanger in which CO_2 after the expansion in Turbine 2 (operating point 6, Fig. 1) is used for heating the lower temperature CO_2 which enters in the recuperator from Turbocompressor. CO_2 with an increased temperature from the recuperator (operating point 3, Fig. 1) enters in the main heater which increases CO_2 temperature at the highest possible level in the plant (operating point 4, Fig. 1). After the main heater, CO_2 expands through Turbine 1 (the only task of Turbine 1 is mechanical power production for the Turbocompressor drive). From the Turbine 1 outlet (operating point 5, Fig. 1), CO_2 is delivered directly to the Turbine 2 inlet through which expands. Turbine 2 is used in this power plant for the electric generator drive and therefore for the electricity production. After the expansion in Turbine 2, CO_2 is send to recuperator (operating point 6, Fig. 1) inside which it transfers heat to colder CO_2. After heat transfer in recuperator (operating point 7, Fig. 1), CO_2 is sent to the main cooler inside which is cooled to the lowest possible temperature in the observed process (operating point 1, Fig. 1). For the cooling purposes in the main cooler can be used various fluids (however, the most used cooling fluid is water).

For the power plant presented in Fig. 1 are analyzed in this paper only the turbomachines because some fluid flow streams and their operating parameters for several heat exchangers are unknown, so the proper energy and exergy analyses cannot be performed for these components. For example, for the main heater are unknown operating parameters of the heating fluid at the main heater inlet and outlet as well as operating parameters of the cooling fluid at the main cooler inlet and outlet, so the proper energy and exergy analyses cannot be performed for these power plant components.

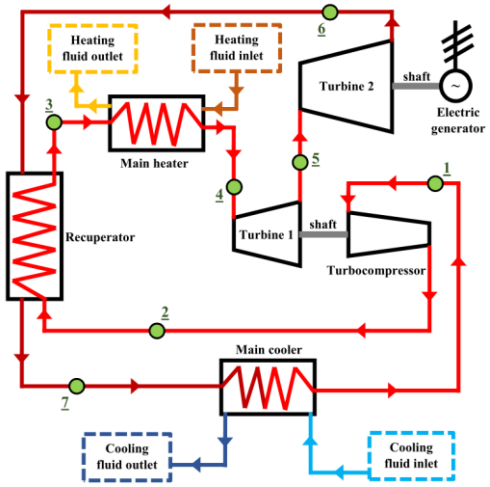


Fig. 1. *General scheme of the supercritical CO_2 power plant and operating points required for the turbomachines (Turbocompressor, Turbine 1 and Turbine 2) isentropic and exergy analyses*

Isentropic analysis of any turbomachine is a comparison of ideal (isentropic) and real (polytropic) compression or expansion process. Data of real (polytropic) compression or expansion processes are obtained from the measurements during the plant exploitation, while the data of ideal (isentropic) processes are obtained by mathematical calculations. Ideal (isentropic) process is the process between the same pressures and it uses the same mass flow rates as the real (polytropic) process, but in ideal process fluid (in this case CO_2) specific entropy remains constant, Fig. 2 [9]. For the observed turbocompressor and both turbines operating point at the end of ideal (isentropic) process is obtained by knowing fluid pressure at the end of the process and fluid specific entropy which remains the same as at the process beginning, Fig. 2. Ideal (isentropic)

compression or expansion process did not consider any losses, losses are considered in the real (polytropic) processes and they are proportional to the increase in fluid specific entropy.

The difference between turbocompressor and any turbine is that turbocompressor is the mechanical power consumer – in an ideal (isentropic) compression process turbocompressor will consume the lowest possible mechanical power, while in real (polytropic) compression process, due to losses occurrence, turbocompressor will consume higher mechanical power in comparison to ideal process. Turbine is a mechanical power producer – in an ideal (isentropic) expansion process turbine will produce the highest possible mechanical power, while in real (polytropic) expansion process, due to losses occurrence, turbine will produce lower mechanical power in comparison to ideal process. These considerations related to ideal and real compression and expansion processes are valid for any mechanical power consumer and producer, not only for the turbocompressor and turbines analyzed in this paper.

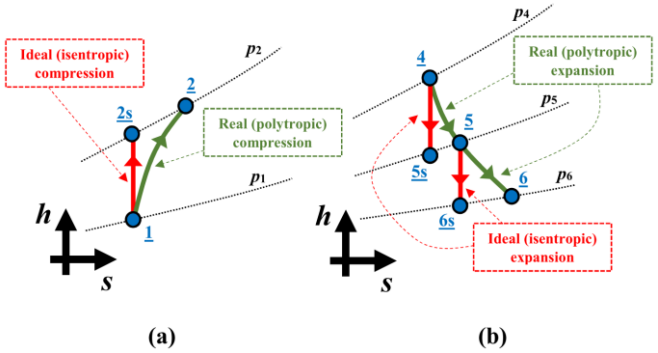


Fig. 2. *Comparison of ideal and real compression and expansion processes: (a) Turbocompressor; (b) Turbine 1 and Turbine 2*

3. Turbomachines analyses equations and principles

Isentropic and exergy analyses of all turbomachines from the observed CO_2 supercritical power plant are performed according to guidelines, recommendations and equations from the available literature [10-12]. Due to the limited space, baseline equations related to any turbomachine isentropic and exergy analyses are not presented in this paper, but they can be found in [13, 14].

The main difference between isentropic and exergy analyses of any turbomachine is that in the isentropic analysis are not considered the parameters of the ambient (ambient pressure and temperature) inside which turbomachine operate (turbomachine isentropic analysis is a comparison of ideal and real operating process), while exergy analysis considers the ambient parameters [7, 15]. Therefore, in exergy analysis can be investigated the influence of the ambient parameters change on the turbomachine (or any other component) operating characteristics [16, 17].

Isentropic and exergy analysis equations of each observed turbomachine are defined in accordance with operating points presented in Fig. 1 and Fig. 2. Exergy analysis equations of each turbomachine remain the same, regardless of the selected ambient parameters.

3.1. Turbomachines isentropic analysis equations

TURBOCOMPRESSOR

Consumed real (polytropic) mechanical power:

$$P_{\mathrm{re,TC}} = \dot{m}_1 \cdot (h_2 - h_1) , \tag{1}$$

where P is mechanical power, $\dot{m}$ is CO_2 mass flow rate and h is CO_2 specific enthalpy. Mechanical power which will be consumed in an ideal situation is:

$$P_{\mathrm{id,TC}} = \dot{m}_1 \cdot (h_{2s} - h_1) . \tag{2}$$

Turbocompressor isentropic loss is:

$$IS_{\mathrm{loss,TC}} = P_{\mathrm{re,TC}} - P_{\mathrm{id,TC}} , \tag{3}$$

while Turbocompressor isentropic efficiency is:

$$\eta_{\mathrm{IS,TC}} = \frac{P_{\mathrm{id,TC}}}{P_{\mathrm{re,TC}}} . \tag{4}$$

TURBINE 1

Produced real (polytropic) mechanical power:

$$P_{\mathrm{re,TURB1}} = \dot{m}_4 \cdot (h_4 - h_5) . \tag{5}$$

Ideal (isentropic) mechanical power is:

$$P_{\mathrm{id,TURB1}} = \dot{m}_4 \cdot (h_4 - h_{5s}) . \tag{6}$$

Turbine 1 isentropic loss is:

$$IS_{\mathrm{loss,TURB1}} = P_{\mathrm{id,TURB1}} - P_{\mathrm{re,TURB1}} , \tag{7}$$

while Turbine 1 isentropic efficiency is:

$$\eta_{\mathrm{IS,TURB1}} = \frac{P_{\mathrm{re,TURB1}}}{P_{\mathrm{id,TURB1}}} . \tag{8}$$

TURBINE 2

Produced real (polytropic) mechanical power:

$$P_{\mathrm{re,TURB2}} = \dot{m}_5 \cdot (h_5 - h_6) . \tag{9}$$

Ideal (isentropic) mechanical power:

$$P_{\mathrm{id,TURB2}} = \dot{m}_5 \cdot (h_5 - h_{6s}) . \tag{10}$$

Turbine 2 isentropic loss is:

$$IS_{\mathrm{loss,TURB2}} = P_{\mathrm{id,TURB2}} - P_{\mathrm{re,TURB2}} , \tag{11}$$

while Turbine 2 isentropic efficiency is:

$$\eta_{\mathrm{IS,TURB2}} = \frac{P_{\mathrm{re,TURB2}}}{P_{\mathrm{id,TURB2}}} . \tag{12}$$

3.2. Turbomachines exergy analysis equations

Exergy analysis of any observed turbomachine considers real (polytropic) compression and expansion processes only as well as fluid (CO_2) total exergy flows.

TURBOCOMPRESSOR

Turbocompressor cumulative exergy inlet is:

$$\dot{E}x_{\mathrm{inlet,TC}} = \dot{m}_1 \cdot \varepsilon_1 + P_{\mathrm{re,TC}} , \tag{13}$$

where $\dot{E}x$ is fluid total exergy flow and ε is fluid specific exergy. Turbocompressor cumulative exergy outlet is:

$$\dot{E}x_{\mathrm{outlet,TC}} = \dot{m}_2 \cdot \varepsilon_2 , \tag{14}$$

while Turbocompressor exergy destruction is:

$$\dot{E}x_{\mathrm{destruction,TC}} = \dot{E}x_{\mathrm{inlet,TC}} - \dot{E}x_{\mathrm{outlet,TC}} . \tag{15}$$

Turbocompressor exergy efficiency is:

$$\eta_{\mathrm{EX,TC}} = \frac{\dot{m}_2 \cdot \varepsilon_2 - \dot{m}_1 \cdot \varepsilon_1}{P_{\mathrm{re,TC}}} . \tag{16}$$

TURBINE 1

Turbine 1 cumulative exergy inlet is:

$$\dot{E}x_{\mathrm{inlet,TURB1}} = \dot{m}_4 \cdot \varepsilon_4 . \tag{17}$$

Turbine 1 cumulative exergy outlet is:

$$\dot{E}x_{\mathrm{outlet,TURB1}} = \dot{m}_5 \cdot \varepsilon_5 + P_{\mathrm{re,TURB1}} , \tag{18}$$

while Turbine 1 exergy destruction is:

$$\dot{E}x_{\mathrm{destruction,TURB1}} = \dot{E}x_{\mathrm{inlet,TURB1}} - \dot{E}x_{\mathrm{outlet,TURB1}} . \tag{19}$$

Turbine 1 exergy efficiency is:

$$\eta_{\mathrm{EX,TURB1}} = \frac{P_{\mathrm{re,TURB1}}}{\dot{m}_4 \cdot \varepsilon_4 - \dot{m}_5 \cdot \varepsilon_5} . \tag{20}$$

TURBINE 2

Turbine 2 cumulative exergy inlet is:

$$\dot{E}x_{\text{inlet,TURB2}} = \dot{m}_5 \cdot \varepsilon_5 \ . \quad (21)$$

Turbine 2 cumulative exergy outlet is:

$$\dot{E}x_{\text{outlet,TURB2}} = \dot{m}_6 \cdot \varepsilon_6 + P_{\text{re,TURB2}} \ , \quad (22)$$

while Turbine 2 exergy destruction is:

$$\dot{E}x_{\text{destruction,TURB2}} = \dot{E}x_{\text{inlet,TURB2}} - \dot{E}x_{\text{outlet,TURB2}} \ . \quad (23)$$

Turbine 2 exergy efficiency is:

$$\eta_{\text{EX,TURB2}} = \frac{P_{\text{re,TURB2}}}{\dot{m}_5 \cdot \varepsilon_5 - \dot{m}_6 \cdot \varepsilon_6} \ . \quad (24)$$

4. CO_2 operating parameters required for the turbomachines isentropic and exergy analyses

CO_2 operating parameters (temperatures and pressures) in each operating point from Fig. 1 are found in the literature [18] and presented in Table 1. It should be highlighted that CO_2 mass flow rate selected in this paper is notably higher than proposed in [18]. Other operating parameters presented in Table 1 which are not found in the literature are calculated by using NIST-REFPROP 9.0 software [19].

In exergy analysis of any system or component a definition of the base ambient state is required [20, 21]. In this paper, the base ambient state is defined by the ambient temperature of 25 °C and the ambient pressure of 1 bar.

CO_2 operating parameters in operating points from Fig. 2 related to ideal (isentropic) compression and expansion processes are presented in Table 2.

Table 1. *CO_2 operating parameters in each operating point from Fig. 1 – real (polytropic) compression and expansion processes*

O. P. *	Temp. (°C)	Pressure (bar)	Mass flow rate (kg/s)	Specific enthalpy (kJ/kg)	Specific entropy (kJ/kg·K)	Specific exergy (kJ/kg) **
1	65.56	105.49	57	431.49	1.7182	230.10
2	126.56	233.04		466.58	1.7210	264.35
3	582.61	229.60		1073.90	2.7602	561.85
4	732.22	227.53		1263.40	2.9660	689.97
5	696.94	176.67		1220.30	2.9723	644.97
6	637.50	113.76		1149.10	2.9821	570.81
7	132.06	106.81		545.01	2.0256	251.97

* O. P. = Operating Point (in accordance to Fig. 1)
** At the base ambient state (25 °C, 1 bar)

Table 2. *CO_2 operating parameters in operating points from Fig. 2 – ideal (isentropic) compression and expansion processes*

O. P.*	Pressure (bar)	Mass flow rate (kg/s)	Isentropic specific enthalpy (kJ/kg)	Specific entropy (kJ/kg·K)
1	105.49	57	431.49	1.7182
2s	233.04		465.48	1.7182
4	227.53		1263.40	2.9660
5s	176.67		1214.20	2.9660
5	176.67		1220.30	2.9723
6s	113.76		1140.10	2.9723

* O. P. = Operating Point (in accordance to Fig. 2)

5. Results and discussion

Real and ideal mechanical power (consumed by the turbocompressor and produced by the turbines) is presented in Fig. 3. In an ideal (isentropic) compression process Turbocompressor consumes lower mechanical power than in the real (polytropic) process (1937.43 kW in comparison to 2000.13 kW), because Turbocompressor is mechanical power consumer. Each turbine in ideal (isentropic) expansion process produces higher mechanical power than in real (polytropic) expansion process because turbine is a mechanical power producer (ideal and real mechanical power produced in Turbine 1 are 2804.40 kW and 2456.70 kW, while in Turbine 2 are 4571.40 kW and 4058.40 kW), Fig. 3. Ideal mechanical power consumed by Turbocompressor and produced in each turbine shows the best possible option, and these results can be used as the guideline for the improvements and losses reduction.

In the observed process, Fig. 1, mechanical power produced in the Turbine 1 is used for the Turbocompressor drive only. Therefore, in real (polytropic) process, Turbine 1 produces slightly higher mechanical power than is consumed by Turbocompressor, which means that mechanical losses in power transmission (real process) from Turbine 1 to Turbocompressor are equal to 456.57 kW.

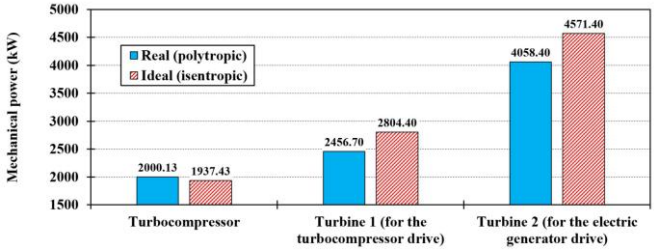


Fig. 3. *Real and ideal mechanical power (consumed by the turbocompressor and produced by the turbines)*

Isentropic and exergy analysis results of each observed turbomachine are presented in Fig. 4 and Fig. 5. From Fig. 4 and Fig. 5 is clear that both isentropic and exergy analyses show the same trends and general conclusions.

The lowest isentropic loss and the lowest exergy destruction of all observed turbomachines has Turbocompressor – consequentially, Turbocompressor has the highest isentropic efficiency of 96.87% and the highest exergy efficiency of 97.61% if all observed turbomachines are considered. Regardless of the fact that Turbine 2 used for the electric generator drive has higher isentropic loss and higher exergy destruction in comparison to Turbine 1, Turbine 2 has higher efficiencies (both isentropic and exergy) in comparison to Turbine 1. Turbine 2 isentropic efficiency is 88.78%, while its exergy efficiency is 96.01%.

In similar closed-cycle gas turbine power systems from the literature [5, 7] can be seen that efficiencies of the turbines (both isentropic and exergy) are higher in comparison to turbocompressors, while for the turbomachines from closed-cycle gas turbine power plant analyzed in this paper is obtained reverse conclusion. The reason for such occurrence can be found in the presented CO_2 operating parameters (Table 1) which seems to be optimal for the Turbocompressor and not fully optimal for Turbine 1 and Turbine 2.

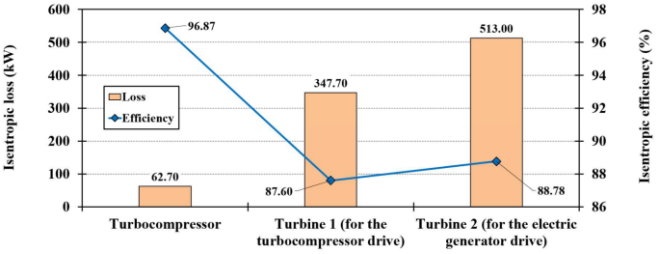


Fig. 4. *Isentropic loss and isentropic efficiency of turbocompressor and both turbines*

The last part of this research involves analysis related to the exergy parameters sensitivity to the ambient temperature change of all observed turbomachines. Exergy parameters sensitivity is investigated in the ambient temperature range from 5 °C up to 45 °C, while the ambient pressure remains the same as at the base ambient state (1 bar). For all analyzed turbomachines is valid a conclusion that increase in the ambient temperature simultaneously increases exergy destructions and decreases exergy efficiencies,

what is also valid for many other components from various power systems [13, 14]. Turbocompressor is the least sensitive to the ambient temperature change of all observed turbomachines, while the sensitivity of both turbines is very similar. Increase in the ambient temperature from 5 °C up to 45 °C decreases Turbocompressor exergy efficiency for 0.31%, while the same ambient temperature increase decreases exergy efficiency of both turbines for 0.53% (Turbine 1) and for 0.52% (Turbine 2). Finally, it can be concluded as in [22, 23] that exergy parameters of turbomachines in general are not highly influenced by the ambient temperature change.

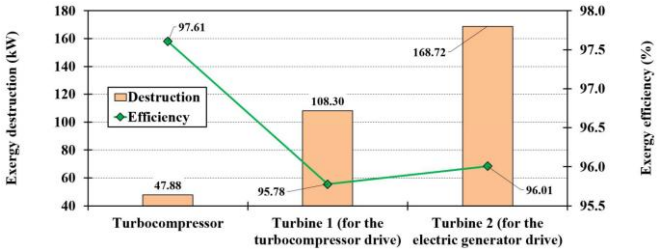


Fig. 5. *Exergy destruction and exergy efficiency of turbocompressor and both turbines at the base ambient state*

6. Conclusions

In this paper are presented results of three turbomachines (one turbocompressor and two turbines) isentropic and exergy analyses. Analyzed turbomachines operate in supercritical CO_2 power plant. The most important obtained conclusions are:

- Both observed turbines (Turbine 1 and Turbine 2) have higher improvement potential than Turbocompressor due to the higher difference between ideal and real mechanical power.
- Mechanical losses in power transmission between Turbine 1 and Turbocompressor are equal to 456.57 kW in real operation process.
- Turbocompressor has the highest isentropic efficiency of 96.87% and the highest exergy efficiency of 97.61% if all observed turbomachines are considered.
- Regardless of the fact that Turbine 2 used for the electric generator drive has higher isentropic loss and higher exergy destruction in comparison to Turbine 1, Turbine 2 has higher efficiencies (both isentropic and exergy) in comparison to Turbine 1. Turbine 2 isentropic efficiency is 88.78%, while its exergy efficiency is 96.01%.
- Increase in the ambient temperature from 5 °C up to 45 °C decreases Turbocompressor exergy efficiency for 0.31%, while the same ambient temperature increase decreases exergy efficiency of both turbines for 0.53% (Turbine 1) and for 0.52% (Turbine 2).
- In general, exergy parameters of turbomachines are not notably influenced by the ambient temperature change.

7. Acknowledgment

This work was supported by the Croatian Science Foundation under the project number HRZZ-IP-2022-10-2821 and by the University of Rijeka scientific grants uniri-iz-25-6 and uniri-iz-25-220 (Funded by the European Union – NextGenerationEU).

8. References

[1] Mrzljak, V., Poljak, I., Orović, J., & Prpić-Oršić, J. (2019). Numerical analysis of real open cycle gas turbine. In IV International Scientific Conference: High Technologies. Business. Society (pp. 51-54).

[2] Anđelić, N., Lorencin, I., Mrzljak, V., & Car, Z. (2024). On the application of symbolic regression in the energy sector: Estimation of combined cycle power plant electrical power output using genetic programming algorithm. Engineering applications of artificial intelligence, 133, 108213. (doi:10.1016/j.engappai.2024.108213)

[3] McDonald, C. F. (2012). Helium turbomachinery operating experience from gas turbine power plants and test facilities. Applied Thermal Engineering, 44, 108-142. (doi:10.1016/j.applthermaleng.2012.02.041)

[4] Olumayegun, O., Wang, M., & Kelsall, G. (2016). Closed-cycle gas turbine for power generation: A state-of-the-art review. Fuel, 180, 694-717. (doi:10.1016/j.fuel.2016.04.074)

[5] Mrzljak, V., Poljak, I., Prpić-Oršić, J., & Jelić, M. (2020). Exergy analysis of marine waste heat recovery CO2 closed-cycle gas turbine system. Pomorstvo, 34(2), 309-322. (doi:10.31217/p.34.2.12)

[6] Mrzljak, V., Jelić, M., Poljak, I., & Medica-Viola, V. (2023). Exergy analysis of supercritical CO2 system for marine diesel engine waste heat recovery application. Pomorski zbornik, 63, 39-62.

[7] Mrzljak, V., Poljak, I., Jelić, M., & Prpić-Oršić, J. (2023). Thermodynamic Analysis and Improvement Potential of Helium Closed Cycle Gas Turbine Power Plant at Four Loads. Energies, 16(15), 5589. (doi:10.3390/en16155589)

[8] Kostyuk, A., & Frolov, V. (1988). Steam and gas turbines. Mir Publishers.

[9] Medica-Viola, V., Baressi Šegota, S., Mrzljak, V., & Štifanić, D. (2020). Comparison of conventional and heat balance based energy analyses of steam turbine. Pomorstvo, 34(1), 74-85. (doi:10.31217/p.34.1.9)

[10] Erdem, H. H., Akkaya, A. V., Cetin, B., Dagdas, A., Sevilgen, S. H., Sahin, B., ... & Atas, S. (2009). Comparative energetic and exergetic performance analyses for coal-fired thermal power plants in Turkey. International Journal of Thermal Sciences, 48(11), 2179-2186. (doi:10.1016/j.ijthermalsci.2009.03.007)

[11] Mrzljak, V., Jelić, M., Poljak, I., & Prpić-Oršić, J. (2023). Analysis and Comparison of Main Steam Turbines from Four Different Thermal Power Plants. Pomorstvo, 37(1), 58-74. (doi:10.31217/p.37.1.6)

[12] Mrzljak, V., Kudláček, J., Baressi Šegota, S., & Medica-Viola, V. (2021). Energy and Exergy Analysis of Waste Heat Recovery Closed-Cycle Gas Turbine System while Operating with Different Medium. Pomorski zbornik, 60(1), 21-48. (doi:10.18048/2021.60.02)

[13] Aljundi, I. H. (2009). Energy and exergy analysis of a steam power plant in Jordan. Applied thermal engineering, 29(2-3), 324-328. (doi:10.1016/j.applthermaleng.2008.02.029)

[14] Ahmadi, G. R., & Toghraie, D. (2016). Energy and exergy analysis of Montazeri steam power plant in Iran. Renewable and Sustainable Energy Reviews, 56, 454-463. (doi:10.1016/j.rser.2015.11.074)

[15] Kanoğlu, M., Çengel, Y. A. & Dincer, I. (2012). Efficiency Evaluation of Energy Systems. Springer Briefs in Energy. (doi:10.1007/978-1-4614-2242-6)

[16] Mrzljak, V., Prpić-Oršić, J., Poljak, I., & Šegota, S. B. (2020). Exergy analysis of steam condenser at various loads during the ambient temperature change. Machines. Technologies. Materials., 14(1), 12-15.

[17] Kopac, M., & Hilalci, A. (2007). Effect of ambient temperature on the efficiency of the regenerative and reheat Çatalağzı power plant in Turkey. Applied Thermal Engineering, 27(8-9), 1377-1385. (doi:10.1016/j.applthermaleng.2006.10.029)

[18] Hoffmann, J. R., & Feher, E. G. (1971). 150 kwe supercritical closed cycle system. Journal of Engineering for Gas Turbines and Power, 93(1), 70-80. (doi:10.1115/1.3445409)

[19] Lemmon, E. W., Huber, M. L., & McLinden, M. O. (2010). NIST Standard Reference Database 23, Reference Fluid Thermodynamic and Transport Properties (REFPROP), version 9.0, National Institute of Standards and Technology. R1234yf. fld file dated December, 22, 2010.

[20] Mrzljak, V., Poljak, I., & Prpić-Oršić, J. (2019). Exergy analysis of the main propulsion steam turbine from marine propulsion plant. Brodogradnja: Teorija i praksa brodogradnje i pomorske tehnike, 70(1), 59-77. (doi:10.21278/brod70105)

[21] Kotas, T. J. (2012). The exergy method of thermal plant analysis. Paragon Publishing.

[22] Poljak, I., & Mrzljak, V. (2023). Thermodynamic Analysis and Comparison of Two Marine Steam Propulsion Turbines. NAŠE MORE: znanstveni časopis za more i pomorstvo, 70(2), 0-0. (doi:10.17818/NM/2023/2.2)

[23] Ameri, M., Ahmadi, P., & Hamidi, A. (2009). Energy, exergy and exergoeconomic analysis of a steam power plant: A case study. International Journal of energy research, 33(5), 499-512. (doi:10.1002/er.1495)

The solution of the boundary value problems of the transfer processes in multilayer enclosing structures

Renat Sadykov
Kazan State Power Engineering University, st. Krasnoselskaya, 51, 420066, Kazan, Russia
E-mail: sadykov_r_a@mail.ru

Abstract: *By means of generalized functions analytical closed solutions of non-stationary transfer in multilayer enclosing structures of canonical forms under asymmetric boundary conditions of the first, second, third and mixed kinds were obtained.*
KEY WORDS: MODELING, SOLUTION, MULTILAYER STRUCTURE, UNIT FUNCTION, THERMOPHYSICAL CHARACTERISTICS.

1. Introduction

The processes of heat and mass transfer and filtration of liquids and vapour-gas mixtures through the capillaries of multilayer enclosing structures are very complex and closely interconnected. In addition, depending on the period of the year, they are accompanied by physically related phenomena such as infiltration and exfiltration of ambient air; evaporative cooling or condensation heating. The implementation of the dense outer layer of the enclosing structures of buildings and structures is not possible in all cases, because such a constructive solution worsens the moisture condition of the enclosure due to difficulties in air permeability and, consequently, and its drying in the summer season [1,2].

Modern multilayer energy-saving enclosing structures (which in a broad sense, in addition to the enclosing structures, they also mean thermal, engineering and electrical networks, "clothing" of roads, tanks and reservoirs for heating, cooling or storing any liquids or gases, etc.) mainly consist of capillary-porous material, which are increasingly used not only in construction, but also in many other industries (high-temperature heat exchangers, turbine blades, rocket nozzles, cladding of high-speed flying machines, cladding of heat and power generating units, systems of nuclear reactors with internal cooling, etc.), where various elements of equipment where various items of equipment are subject to sufficiently high thermal stresses and pressures resulting from large gradients of transfer potentials (temperature, pressure and mass content) [3-9].

2. Main Body

In the most general case the nonlinear differential equation system of convective non-stationary transfer can be written in the vector-matrix form:

$$\begin{aligned} &\mathrm{D}\bar{\mathrm{S}}[\overline{\Pi}(\bar{\mathrm{x}},\tau)] + \bar{\tau}_{\mathrm{r}}\bar{\mathrm{S}}_{\tau\tau}[\overline{\Pi}(\bar{\mathrm{x}},\tau)] + \\ &\mathrm{sgn}[\bar{\mathrm{J}}] < \bar{\nabla},\ \bar{\mathrm{J}}[\overline{\Pi}(\bar{\mathrm{x}},\tau)] > + \mathrm{sgn}[\bar{\mathrm{I}}]\bar{\mathrm{I}}[\overline{\Pi}(\bar{\mathrm{x}},\tau)] = \bar{0} \end{aligned} \qquad ((1)$$

The system (1) also describes high-intensity, high-speed and high-temperature processes (second member of the equation), when the speed of propagation of the substance is comparable with the speed of the processes themselves (metal cutting, laser welding, etc.), i.e., when both the relaxation time of the densities of the flows of substances and the time of their damping $\nabla\overline{\Pi}(\bar{\mathrm{x}},\tau)$ can be taken into account. If to be based on the phenomenological theory of the transfer processes, then there will be no second member of the nonlinear differential equation system (1), because the propagation speed of the flows of substances tends to infinity, and $\bar{\tau}_r$ tends to zero [3,10]. In this case, the nonlinear differential equation system (1) comes over from the hyperbolic type to the parabolic type, which describes the irreversible processes of convective conjugate transfer and, in particular, heat and mass transfer processes.

Particularly posed are boundary-value problems when differential equations (DEs) are equations of mixed type, i.e. when in different parts of the considered region of independent variable multilayer construction the differential operator (D) belongs to different (hyperbolic, parabolic and elliptical) types [11,12], i.e. when $\nabla\overline{\Pi}(\bar{\mathrm{x}},\tau)$ in separate layers of multilayer construction differ from each other by significant values.

High-intensity technological processes of heat and mass transfer in modern technology нос have a non-stationary nonlinear character, because at sufficiently high concentrations (temperatures), the heat and mass transfer coefficients depend on the potentials themselves [K($\overline{\Pi}$)], then the corresponding nonlinear differential equation system (or nonlinear transfer equation) is solved only numerically or approximately by special methods [11-18, 22-28, 38, 44, 54]. For such transfer processes the nonlinear differential equation system in heterogeneous bodies of arbitrary geometric shape is reduced to the integration of the following system, presented in the vector-matrix notation:

$$\begin{aligned} D\overline{\Pi} + \sum_{i=2}^{n} \tau_{\bar{J}}^{i-1}\overline{\Pi}^{(i)} &= sgn\left[\bar{J}\right]\sum_{i=1}^{m}\tau_{\overline{\Pi}}^{i-1} < \nabla, \left[K\left(\overline{\Pi}\right)\right]\left[\nabla\overline{\Pi}\right]^{(i-1)} \\ &> + sgn\left[\bar{I}\right]\sum_{i=1}^{n}\tau_{\bar{J}}^{i-1}\,\bar{\tilde{I}}^{(i-1)} \end{aligned} \qquad (2)$$

or in the scalar notation

$$\begin{aligned} D\Pi_i + \sum_{i=2}^{n} \tau_{\bar{j}_i}^{i-1}\Pi_i^{(i)} &= sgn\left[\bar{J}_i\right]\sum_{i=1}^{m}\tau_{\overline{\Pi}_i}^{i-1} < \nabla, \left[k_{ij}\left(\Pi_j\right)\right]\left[\nabla\Pi_j\right]^{i-1} \\ &> + sgn[I_i]\sum_{i=1}^{n}\tau_{\bar{j}_i}^{i-1}\tilde{I}^{(i-1)}, \\ &\quad i = \overline{1,n} \end{aligned} \qquad (3)$$

With a constant matrix of coefficients of the nonlinear differential equation system (2) and (3) can be rewritten, accordingly, in the form:

$$\begin{aligned} D\overline{\Pi} + \sum_{i=2}^{n} \tau_{\bar{J}}^{i-1}\overline{\Pi}^{(i)} &= sgn\left[\bar{J}\right]\sum_{i=1}^{m}\tau_{\overline{\Pi}}^{(i-1)}\,[K]\left[\nabla^2\overline{\Pi}\right]^{i-1} \\ &\quad + sgn\left[\bar{I}\right]\sum_{i=1}^{n}\tau_{\bar{J}}^{i-1}\bar{\tilde{I}}^{(i-1)}, \end{aligned} \qquad (4)$$

$$\begin{aligned} D\Pi_i + \sum_{i=2}^{n} \tau_{J_i}^{i-1}\Pi_i^{(i)} &= sgn\left[\bar{J}_i\right]\sum_{i=1}^{m}\tau_{\Pi_i}^{i-1}\sum_{j=1}^{n}k_{i,j}\,\nabla^2\Pi_j^{(i-1)} \\ &\quad + \mathrm{sgn}\left[\bar{\mathrm{I}}_{\mathrm{i}}\right]\sum_{\mathrm{i}=1}^{\mathrm{n}}\tau_{J_i}^{i-1}\bar{\tilde{I}}_i^{(i-1)}, \qquad \mathrm{i} = \overline{1,\mathrm{n}}. \end{aligned} \qquad (5)$$

In the absence of convective transfer, the nonlinear differential equation system (2) can be rewritten in the form:

$$\begin{aligned} \sum_{i=1}^{n} \tau_{\bar{J}}^{i-1}\overline{\Pi}^{(i)} &= sgn\left[\bar{J}\right]div\sum_{i=1}^{m}[K][\tau_{\overline{\Pi}}^{i-1}\,\nabla\overline{\Pi}^{(i-1)}] \\ &\quad + sgn\left[\bar{I}\right]\sum_{i=1}^{n}\tau_{\bar{J}}^{i-1}\,\tilde{I}^{(i-1)}. \end{aligned} \qquad (6)$$

From (6), the nonlinear differential equation system of the inter-related and unrelated transfer by hypotheses follows:

1- Fourier (for n = 1 and m = 1), when there are no time derivatives of flows of substances and gradients of transport potentials (DE of parabolic type);

2- Cattaneo Vernotte (for n=2, m=1), taking into account the first time derivatives of the flows of transferred substances $\frac{\partial \overline{J}(\overline{x},\tau)}{\partial \tau}$ (DU of hyperbolic type);

3- Maxwell – Cattaneo - Lykov (for n=2 and m= 2) , taking into account the first derivatives of the flows and gradients of the potentials of substances $\frac{\partial \overline{J}(\overline{x},\tau)}{\partial \tau}$ and $\frac{\partial \nabla \overline{\Pi}(\overline{x},\tau)}{\partial \tau}$ (DU of hyperbolic type);

4- The nonlinear differential equation system and DE (for n ≥ 3 and m≥ 3), taking into account the second derivatives and higher in time by flows and gradients of transport potentials.

The physical justification for the need to take into account derivatives of a higher order is still not enough weight. Therefore, the adequacy of their accounting requires additional resolution using experimental-theoretical research. In addition, the appearance of additional terms in the nonlinear differential equation system and DE noticeably complicates the calculations of transient transfer processes [29–37, 39–52, 56].

If it is necessary to take into account the convective transfer, the convective component of the Lagrange derivative is added to the first term of the left-hand side of the nonlinear differential equation system(6). For example, according to the Fourier hypothesis, the nonlinear differential equation system of the heat and mass transfer in scalar form at $[k_{ij}]$=var, will be:

$$D\Pi_i = sgn[\overline{J}_i] < \nabla, \sum_{j=1}^{n} k_{i,j}\left(\Pi_j\right)\nabla\Pi_j > + sgn[I_i]I_i(\overline{x},\tau);$$

$$i = \overline{1,n}\,, \qquad (7)$$

for $[k_{ij}] = const$

$$D\Pi_i = sgn[\overline{J}_i] \sum_{j=1}^{n} k_{i,j}\nabla^2\Pi_j + \mathrm{sgn}[I_i]\mathrm{I}_i(\overline{x},\tau), \quad \mathrm{i} = \overline{1,\mathrm{n}}\,. \quad (8)$$

When setting the boundary-value problem (according to the Fourier hypothesis) in heterogeneous media, the matrix of transfer coefficients [K] mainly depends only on the spatial coordinates $\overline{x}$, but because the nonlinear differential equation system (or equation) of transfer includes the second derivatives of the required transfer potentials by variable $\overline{x}$, then it can no longer be reduced to the differential equation system with constant coefficients and it must be solved only by approximate methods. For example, for engineering calculations, approximate analytical methods for solving the boundary-value problem are widely used. These are variational methods (Ritz, Treffts, A.V. Kantorovich and others); methods of weighted residuals (Bubnov-Galerkin orthogonal method, collocations, moments, least squares, etc.); operational methods (Laplace, infinite and finite Fourier transforms, Hankel, etc.); integral methods of heat balance, averaging of functional corrections, methods of M. Bio, M.E. Shvets, A.I. Veinik and others, in which the model of potential disturbance is used (for example, the penetration depth of the thermal layer); methods for sharing accurate (separation of variables, integral transforms, thermal potentials, etc.) and the above approximate analytical methods [12-18, 28, 33, 36, 38].

One of the simple methods for an approximate solution is to replace $[\mathrm{K}(\overline{x})]$ ку with piecewise constant functions. For this, the intervals of change of $\overline{x}$ (all axes, semi-axes, or finite intervals) are divided into partial intervals $(\overline{x}_{i-1}, \overline{x}_i)$ and in each partial interval are considered $[\mathrm{K}]=[K_i(\overline{\xi}_i)]$ constant for $\forall\overline{\xi}_i \in (\overline{x}_{i-1}, \overline{x}_i)$, and then the posed boundary-value problem is already solved by known methods [11–13, 18, 24, 26, 54, 55] with the boundary conditions for "gluing" the solution. If $\overline{x}_i -$ is the division point (boundary or surface) of two adjacent partial intervals, then the transfer potentials $\overline{\Pi}(\overline{x}_i)$ in it are assumed to be continuous or the middle of the jumps of the functions $\overline{\Pi}(\overline{x}_i)$ at the points of a removable discontinuity $\overline{x}_i$ of the first kind (for example, when contact thermal resistance of two adjacent of multilayer construction layers is taken into account).

Somewhat simpler, but practically important, are the transfer processes passing through a finite number of layers, i.e. through a piecewise homogeneous medium. The mathematical formulation of the such boundary-value problem can be written in the form:

$$\frac{\partial \Pi_i}{\partial \tau} = k_i\Delta\Pi_i + I_i(\overline{x},\tau),\ i = \overline{1,n}\,, \qquad (9)$$

where the transfer potential $\Pi_i(\overline{x},\tau)$ means either the mass transfer potential (moisture content, substance concentration) or temperature, and k_i means the constants, respectively, either the diffusion coefficient or thermal diffusivity of the i-th layer of the multilayer construction.

The differential equation system of interconnected heat and mass transfer for piecewise homogeneous media under a number of simplifying assumptions (when $\mathrm{B}i_m > 100$, and $\mathrm{Lu} \gg 1$ or $\mathrm{Lu} \ll 1$) and the condition of the zonal method of calculation (or application of the local coordinate system), when the transfer coefficients are accepted independent of coordinates, are also reduced to consideration the differential equation system of unrelated transfer (9) [4]. The solution of such problems under various single-valued conditions can be found in [4, 14, 15, 25] and other sources.

For a generalized analytical solution by the Fourier method of similar linear boundary-value problems (parabolic, hyperbolic and elliptic types) with linear additional conditions (for example, when a linear combination of $\Pi(\overline{x},\tau)$ and its normal derivative is given on the surface (or contour) of the region) are preliminarily reduced to the simpler boundary-value problems, then their general solution is obtained from the superposition principle. The limiting problems of transfer processes are also solved in a same way.

It should be noted that when setting such boundary-value problems, due to the definiteness and continuity of $\overline{\Pi}(\overline{x},\tau)$ in the closed (considered) region and $\overline{\Pi}(\overline{x},\tau)$ satisfies the transfer equations in the open region, the continuity of the initial and boundary conditions and the requirement of their compatibility with each other follow. However, the conditions for the continuity of the initial value and the conditions for its conjugation with the boundary values are very restrictive and often exclude practically important cases from consideration. In these cases, the boundary-value problems are considered with piecewise continuous initial functions, not assuming that the initial function is associated with boundary conditions or the filtering property of the Dirac impulse function is used to construct the influence function (Green), which allows to find an integral solution of the heterogeneous DE satisfying homogeneous boundary conditions. To solve non-stationary boundary-value transfer problems in multilayer constructions, the mathematical theory of generalized functions is successfully used (the delta-Dirac function and its filtering property; Heaviside unit function, asymmetric unit function, other step functions), which allows one to adequately describe the distributions of different discontinuous physical characteristics of a piecewise homogeneous medium and in closed form to obtain analytical solutions of boundary-value problems by reducing multilayer constructions to single-layer ones [4,13-17].

In many important applied boundary-value problems of molecular diffusion and thermal conductivity for piecewise homogeneous media, one has to deal with boundary conditions, when the concentration (temperature) of the substance at the boundary of the layer is actually some given function of time (i.e. it is the solution of the boundary-value problem for the previous layer at its given thickness) and this value, due to the "gluing" condition, serves as the boundary condition for concentration (temperature) on the segment of the next homogeneous layer [11,12,18]. An analytical solution to such non-stationary boundary-value problem is applied for mathematical modeling (MM) of desalination of drinking water at the ultrafiltration nanomembrane combined water treatment plant for water and heat supply systems. An MM of the process of filtering a crude liquid with a given constant concentration of suspended colloidal particles, diffusion coefficient and fluid flow through the adsorbent layer, which contains a medium with its diffusion coefficient. From some initial moment of

time the diffusion process begins, during which it is necessary to determine the change in the concentration of suspended and colloidal particles in a given region of the event space (independent variables).

In a stationary formulation for non-linear heat transfer taking into account filtration (gas, steam-gas mixture, liquid) and the presence of internal volumetric drains (moisture) or heat sources under generally accepted assumptions [1,2] in the one-dimensional case as applied to canonical forms in the corresponding coordinate systems, the system (1) the system can be written in the form of an ordinary differential heterogeneous second-order equation [19-21].

In the physical description of the cooling processes of the enclosing structure (possibly evaporative) or heating (possibly condensation), thermal balances can be compiled similarly to equation (1) both for the region $r \in [-\infty, 0]$, and for the region $r \in [h, +\infty]$, which lead to new DEs of gas (or liquid) flows running towards the enclosing structure and moving away from the enclosing structure with boundary conditions corresponding to new closed intervals r. In this case, one or two second-order DEs and, accordingly, two or four boundary conditions are added to the nonlinear differential equation system (1) depending on the conditions of the problem. By this means, the generalized MM, even for stationary heat transfer in the building envelope, must contain three second-order DEs and six boundary conditions for finding the corresponding integration constants. In this case, the temperature field T(r) in the enclosing structure expressed through the ambient air temperatures (gas, liquid, coolant or refrigerant) on both sides. In a more simplified version, these boundary DEs for the enclosing structure are replaced by boundary conditions of the third kind, with possible consideration of surface runoff or heat sources at the boundary of the enclosing structure surfaces [3,22,23]. Conversely, equation (1) with boundary conditions of the third kind can be replaced by simpler boundary conditions of the first kind provided that constant fictitious (equivalent) boundary layers are introduced. An analysis of convective heat transfer shows that in this case the boundary conditions of the third kind are actually displayed in the boundary conditions of the first kind. Then, when integrating the DE (1) and the presence of two isothermal surfaces in boundary conditions, we can use the Kirchhoff transformation [22, 23], which through a new auxiliary variable and the average coefficient of thermal conductivity leads DE (1) to formalize the first boundary-value problem.

A boundary-value problem formalized in this way can be written through the Peclet criteria (Pe), Pomerantsev criteria (Po), dimensionless scales of temperature and thermal resistance, which is especially convenient as it allows to convert a multi-layer enclosing structure into a single-layer [19,20].

If the limits of variation of Pe and Po are known, then the sign of the signature in the boundary-value problem can be omitted and these criteria can be considered only in the closed interval [0,1], then the Peclet and Pomerantsev criteria can be written as: $\overline{\mathrm{Pe}} = (\mathrm{Pe} - \inf \mathrm{Pe})/(\sup \mathrm{Pe} - \inf \mathrm{Pe})$, $\overline{\mathrm{Po}} = (\mathrm{Po} - \inf \mathrm{Po})/(\sup \mathrm{Po} - \inf \mathrm{Po}) \in [0,1]$. In this case, all dependent and independent variables and parameters of the posed boundary-value problem are dimensionless and lie in a four-dimensional normalized unit space $(\mathrm{T}, \overline{\mathrm{R}}, \overline{\mathrm{Pe}}, \overline{\mathrm{Po}})$. The given transformations considerably simplify mathematical formalization of problems, eliminate physical dimensions and signs, and solve the issues of large-scale transition. The only thing that complicates the physical interpretation of problems, especially when graphic solutions to problems are built in the above space, where in fact the directionality of the flows and the sign of the heat source are "lost" due to the absence of negative values of the problem parameters in the closed interval [0,1], but this complication is easily eliminated by returning to the initial parameters of the posed physical or applied boundary-value problems.

3. Conclusions

A generalized MM of heat and mass transfer in piecewise homogeneous media for hyperbolic (reflective high-temperature, high-speed and high-intensity processes), parabolic and elliptic types under various single-valuedness condition is presented.

Boundary-value problems of both interconnected and unconnected stationary and non-stationary transfer and some algorithms of their solution for classical form bodies are considered.

Analytical solutions of direct boundary-value problems of the processes of transfer of substances are obtained under generalized conditions on the outer contour of the investigated region and its discontinuous physical properties inside, as well as with variable (in time) transfer potentials in the boundary conditions (first, second, third and mixed kinds).

Formalized MM, analytical and approximate solutions of the boundary-value transfer problem are normalize to the criterial form, which is convenient for large-scale transitions, practical applications, parametric analysis of the obtained solutions, setting objectives for optimization and automation of control systems. Based on the results of solving a number of applied boundary-value problems, their physical interpretation is given.

4. Designations

The proposed solution of problem (1) in the form (10) is of practical interest in calculating the rates of change of the corresponding transfer potentials. They allow one to quite simply link the problems of interrelated transfer with the problems of the classical theory of heat conduction and diffusion, determine the degree of influence of individual factors on the course of development of the process and, as a result, obtain simplified analytical expressions that are so necessary for engineering practice.

The results obtained serve the development of the general theory of mathematical modeling and can be useful in setting up experimental studies on non-stationary heat and mass transfer, in the analysis and calculation of exchange processes in industry and design [3-7].

5. References

1. Bogoslovsky V. N. Construction Thermal Physics. (Thermophysical Principles of Heating, Ventilation, and Air Conditioning). St. Petersburg: AVOK Severo-Zapad, 2006. 400 p.
2. Hugo Hens. Building Physics – Heat, Air and Moisture. John Willey & Sons Limited, 2007. 270 p.
3. Isachenko V. P., Osipova V. A., Sukomel A. S. Heat Transfer. Moscow: Energoizdat, 1981. 416 p.
4. Lykov A. V., Mikhailov Yu. A., Theory of Heat and Mass Transfer. Moscow-Leningrad: Gosenergoizdat, 1963. 535 p.
5. Tsoi P. V. System methods for calculating boundary value problems of heat transfer. – M.: Publishing house MPEI, 2005. 568 p.
6. Lukanin V.N., Shatrov M.G., Kamfer G.M. and others. Thermal engineering. M.: Higher school, 2000. 671 p.
7. Rudobashta S.P. Heat engineering. M.: Pero, 2015. 672 p.
8. Baskakov A.P. Thermal engineering / Baskakov A.P., Berg V.V., Witt O.K. and others. M.: Energoatomizdat, 1982. 264 p.
9. Matyukhov D.V., Nizovtsev M.I., Terekhov V.I., Terekhov V.V. Determination of Thermal Protection Characteristics of Thermal-Inertial Structures under Non-Stationary Heat Transfer Conditions. // Proceedings of the III Russian National Conf. on Heat Transfer. Vol. 7, MPEI Publishing House, 2002. pp. 184-187.
10. Lykov AV Heat and Mass Transfer (Handbook). Moscow: Energia, 1971. 560 p.
11. Tikhonov AN, Samarskii AA Equations of Mathematical Physics. Moscow: Nauka, 1977. 736 p.
12. Vladimirov VS Equations of Mathematical Physics. Moscow: Nauka, 1981. 512 p.
13. Vladimirov VS Generalized Functions in Mathematical Physics. Moscow: Nauka, 1979. 320 p.
14. Kudinov V.A., Kudinov I.V., Skvortsova M.P. Generalized Functions and Additional Boundary Conditions in Heat Conduction Problems for Multilayer Bodies // Journal of Computational

Mathematics and Mathematical Physics. (Moscow State University). 2015. Vol. 55, No. 4, pp. 669-680.
15. Kartashov E.M., Kudinov, Kalashnikov V.V. Heat and Mass Transfer Theory: Solution of Problems for Multilayer Structures. Moscow: Yurait, 2018. 436 p.
16. Kudinov I.V., Kudinov V.A. Analytical Solution of Parabolic and Hyperbolic Heat and Mass Transfer Equations. Moscow: Infa-M, 2013. 392 p.
17. Aziz A.A. A similarity solution for a laminar thermal boundary layer over a flat plate with a convective surface boundary condition. Commun Nonlinear Sci Numer Simulat 14 (2009), pp. 1064–1068.
18. Aramanovich, I. G., Levin, V. I. Equations of Mathematical Physics. Moscow: Nauka, 1969, 288 p.
19. Sadykov, R. A., Kraynov, D. V., Ivanova, R. V. Transfer processes in enclosing structures taking into account air permeability and heat sinks. Proceedings of the 3rd International Scientific and Technical Conference "Theoretical Foundations of Heat and Gas Supply and Ventilation". Moscow: MGSU, 2009, pp. 90–92.
20. Sadykov, R. A., Kraynov, D. V., Ivanova, R. V. Thermal insulation properties of enclosing structures in the presence of drains or heat sources and air filtration. // Scientific and technical journal M.: Vestnik MGSU. 2011. No. 7. Pp. 174-180.
21. Sadykov R. A., Maneshev I. O. Study of thermal conductivity coefficients of thin-layer heat insulators. // Kazan: Izvestia KSUACE. 2016. No. 1. Pp. 134-142.
22. Isaev S. I., Kozhinov I. A., Kofanov V. I., et al. Theory of heat and mass transfer (ed. by Leontev A. I.). Moscow: Vysshaya shkola, 1979. 495 p.
23. Kozdoba L. I. Methods for solving nonlinear heat conduction problems. Moscow: Nauka, 1975. 227 p.
24. Mikhlin S.G., Course of Mathematical Physics. Moscow: Nauka, 1968. 576 p.
25. Averin B.V. General scheme of solution for the boundary value problem of non-steady terminal conductivity with internal thermal sources for multi-layer constructions. Herald of Samara State Technical University. 2009. No. 2(19). P. 274-277.
26. Aramanovich I.G., Lunts G.L., Elsgolts L.E. Functions of a complex variable. Operational calculus. Stability theory. Moscow: Nauka, 1968. 416 p.
27. Tsirelman N.M. Direct and inverse problems of heat and mass transfer. Moscow: Energoatomizdat, 2005. 393 p.
28. Belyaev N.M., Ryadno A.A. Methods of Heat Conduction Theory. In 2 parts. Part I – Moscow: Higher Mathematics. 1982. 327 p. Part II - 304 p.
29. Cattaneo C. On a form of the equation of the chaleur that eliminates the paradox of an instantaneous propagation // Compte Rendus. Acad. Sci. Paris. 1958. Vol. 247, P. 431.
30. Vernotte P. Les paradoxes de la theory of the continued equation of the chaleur // Compte Rendus. Acad. Sci. Paris. 1958. Vol. 246, P. 3154.
31. Kaliski S. Wave equation for heat conduction /S.Kaliski//Bull. Acad. Pol. Sci. –1965. –Vol.XIII(4).–P.211.
32. Kirsanov Yu.A. Applied theory of heat conduction. Stationary and non-stationary thermal processes in porous and solid bodies /Saarbrücken, Germany: LAP LAMBERT Academic Publishing, 2012. 365 p.
33. Körner C., Bergmann H.W. The physical defects of the hyperbolic heat conduction equation // Appl. Phys. A, 1998. Vol.67, P.397.
34. Ahmadikal H., Rismanian M. Analytical solution of non-Fourier heat conduction problem on a fin under periodic boundary conductions // Journal of Mechanical Science and Technology. 2011. Vol.25(11), P.2919.
35. Majumdar A. Microscale Heat Conduction in Dielectric Thin Films // J. Heat Transfer. 1993. Vol.115(1), P.7.
36. Joshi A.A., Majumdar A. Transient ballistic and diffusive phonon heat transport in Thin films // Journal of Applied Physics. 1993. Vol. 74(1), P. 31.
37. Lykov A. V. Application of Methods of Thermodynamics of Irreversible Processes to the Study of Heat and Mass Transfer // Engineering-Physical Journal. 1965. Vol. 9. No. 3. P. 287.
38. Kartashov E. M. New Relationships for Analytical Solutions of Hyperbolic Transfer Models // Bulletin of the Academy of Sciences. Power Engineering. 2015. Vol. 4, P. 38.
39. Tzou D. Y. The Generalized Lagging Response in Small-Scale and High-Rate Heating // International Journal of Heat and Mass Transfer. 1995. Vol. 38, P. 3231.
40. Liu K. C., Chang P. C. Analysis of dual –phase–lag heat conduction in cylindrical system with a hybrid method // Applied Mathematical Modeling. 2007. Vol.31, P.369-380.
41. Guyer R.A., Krumhansl J.A. Soluyion of the Linerized Boltzmann Equation // Physical Review.1996.Vol.148, P.766.
42. Joseph D.D., Preziosi L. Heat Waves // Reviews of Modern Physics. 1989. Vol.61, P.41.
43. Al-Nimr M.A., Naji M., Arbaci V.S. Nonequilibrium Entropy Production Under the Effect of the Dual-Phase-Lag Heat Conduction Model // Journal of Heat Transfer. 2000. Vol.122, P.217.
44. Kudinov V.A., Kudinov I.V. Study of thermal conductivity taking into account the finite velocity of heat propagation // High Temperature Thermophysics. 2013. Vol. 51, No. 2, p. 301.
45. Roy Choudhuri S.K. On a thermoelastic three-phase-lag model // Journal of Thermal Stressis. 2007. Vol. 30, p. 231.
46. Miranville A.A., Quitanilla R. Phase-Field Model Based on a Three-Phase-Lag Heat Conduction // Applied Mathematics & Optimization. 2011. Vol. 63, Issue 1, p. 133.
47. Akbarzadeh A.H., Pasini D. Phase-lag heat conduction in multilayered cellular media with imperfect bonds // International Journal of Heat and Mass Transfer. 2014. Vol.75, P.656.
48. Li L., Zhou L., Yang M. An Expanded Lattice Boltzmann Method for Dual Phase Lag model // International Journal of Heat and Transfer. 2016. Vol.93, P.834.
49. Han S. Finite volume solution of two – step hyperbolic conduction in casting sand // International Journal of Heat and Mass Transfer. 2016. Vol.93, P. 1116.
50. Shomali Z., Abbassi A. Investigation of highly non-liner dual – phase – lag model in nanoscale solid argon with temperature – dependent properties // International Journal of Thermal Scinces. 2014. Vol.83, P. 56.
51. Tzou D.Y. Macro to Microscale Heat Transfer: The Lagging Behavior 2nd Edition // West Sussex, UK: John Wiley & Sons Ltd. 2015. 1289 p.
52. Torabi M., Zhang K. Multi-dimensional dual-phase-lag heat conduction in cylindrical coordinates: Analytical and numerical solutions // International Journal of Heat and Mass Transfer. 2014. Vol. 78, pp. 960 – 966.
53. Bolgarsky A. V., Mukhachev G. A., Shchukin V. K. Thermodynamics and Heat Transfer. Moscow: Vysshaya shkola, 1975, 495 p.
54. Zeldovich Ya. B., Myshkis A. D. Elements of Applied Mathematics. Moscow: Nauka, 1965. 616 p.
55. Pismenny D. T. Lecture Notes on Higher Mathematics. Moscow: Airis-Press. 2019. 608 p.
56. Yudakin, A.E. Study of Heat Conduction Models under Fast Thermal Processes in Low-Thermal-Conductivity Solids. Abstract of Cand. Sci. (Eng.) Diss., Kazan State Power Engineering University. Kazan, 2017.-20 p.

The theory of transfer processes with short-term contact phases

Renat Sadykov, Airat Osipov, Artem Akhmerov
Kazan State Power Engineering University, st. Krasnoselskaya, 51, 420066, Kazan, Russia
E-mail: sadykov_r_a@mail.ru, nord7077@yandex.ru, akhm@mail.ru

Abstract: *Using the methods of systemic, mathematical and numerical analysis, as well as general physicochemical and thermodynamic laws, a complex of theoretical and experimental studies of transfer processes during short-term contact of phases has been carried out. These studies made it possible to fully reveal the regularities of external and internal heat and mass transfer, to find scientifically grounded ways to intensify the processes of vacuum, conductive and combined drying methods. Within the framework of linear nonequilibrium thermodynamics, a mathematical model of filtration-diffusion energy and mass transfer has been developed with a correct estimate of the orders of the terms in the system of differential equations of energy and mass transfer, taking into account the composition of the vapor-air mixture in the capillary-porous body. The limits of applicability of the hypothesis of short-term contact of phases according to the Fourier criterion for the transfer inside and outside the surfaces of the canonical shape (plate, cylinder, sphere) and wedge are estimated from the standpoint of the accuracy of calculating interphase flows. It is shown that in a number of cases the contact is not short-lived due to the curvature and the presence of angles on the contact surface, and not due to the finiteness of the dimensions of the contacting phases.*
KEY WORDS: *DRYING, DYNAMICS, SHORT-TERM CONTACT, PHASE, SURFACE, FOURIER CRITERION, MATHEMATICAL MODELING, HEAT AND MASS TRANSFER, ANALYSIS.*

1. Introduction

The properties of the product at the outlet of the apparatus and the choice of the optimal technological mode of its processing are mainly determined by interrelated processes occurring inside the contact (boundary) layer of the material being processed (heat and mass transfer) and in the boundary layer of the environment (heating wall, air, inert coolant, steam, catalyst, etc.), since changes in environmental parameters change the conditions for the transfer of matter in the whole system, and the intensification or decrease in the material of physicochemical and phase transformations affects the structure of the boundary layer. A qualitative analysis of the mechanism of transfer processes is associated with finding non-stationary fields of transfer potentials (temperature, concentration, pressure, etc.), the evolution of which makes it possible to theoretically investigate the kinetics and dynamics of the process and outline the optimal conditions for its implementation. Modern intensification of materials processing technology leads to an increase in the role of non-stationary interconnected exchange processes in comparison with stationary unrelated ones. This fact has not yet found sufficient reflection in the field of solving problems of energy and mass transfer at low Fourier numbers - with short-term contact of the phases.

2. Theory and results

One of the effective means of intensifying the transfer processes, for example, with a conductive energy conduit, is mixing the product, which constantly renews the contact layer of the material and equalizes the temperature, pressure, concentration of the processed medium (possibly three-phase) in its bulk, which makes it possible to obtain large flows through the interface. Often the physical model of these processes is a series of short-term contacts product with heating surface , and the transfer rate strongly depends on the contact time τ_k For example, for drum, rake, roller, cylindrical dryers, where mixing is associated with rotation, τ_k is defined by the formula τ_k=ψ/ω where ω is the angular velocity of rotation of the mixing devices, and ψ is the characteristic angle. For shelf dryers, belt dryers, disc dryers, vibrating dryers, etc. depending on the organization of mixing τ_k determined by the period of shaking, the frequency of vibration, the residence time of the product on a given plate, conveyor belt, etc. In the packet theory of fluidized and in the simplified model of gushing beds τ_k is determined by the speed of movement of the product (package) on the heating surface [8,9].

Let us consider separately the physical and mathematical aspects of modeling transfer processes during short-term contact of phases.

Physical model of short-term contact of phases. Multiple repetition of contact interactions up to several thousand times makes it possible to describe heat transfer as stationary, using the heat transfer coefficient, the values of which are determined by unsteady heat and mass transfer during one contact.

Methods of organizing the contact of the product with the heating surface In the analysis of short-term contact, the concept of heat transfer coefficient is introduced [3].

$$\alpha(\tau) = \frac{q(\tau)}{F(T_{гп} - T)}, \#$$

and it is called instant [8], conditional [10], contact [9], given [5]. For the average value α (τ) for the time of one contact, the expression [3,7,8,10] is used

$$< \alpha^k >_{\tau_k} = \frac{1}{T_k}\int_0^{\tau_k} \alpha(\tau)d\tau = 2\frac{\sqrt{\lambda c\rho}}{\sqrt{\pi\tau_k}}, \#(2)$$

where λ is the coefficient of thermal conductivity, $\sqrt{\lambda c\rho_0}$is the coefficient of heat assimilation (thermal activity) of the product [6]. Formula (2) was obtained by O. Krisher [3] under the following assumptions due to the small thickness of the heated contact layer of the material. A flat heating surface is placed at the point x = 0, and the material occupies the entire half-space x> 0; the heat conduction problem is one-dimensional, i.e. isothermal surfaces are parallel to the heating surface. The initial temperature distribution is assumed to be uniform, due to the presence of mixing:

$$T(x, 0) = T_0. \#(3)$$

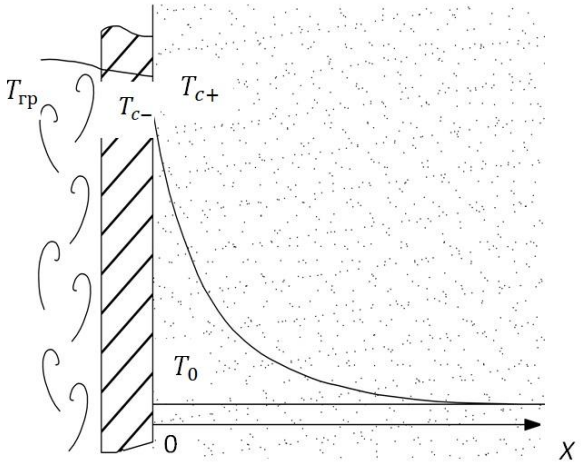


Fig. 1. On the formulation of the problem of short-term contact

Since the main thermal resistance is concentrated in the contact layer of the material, where the temperature gradients are many times higher than those in the heating agent and the shell, the temperature T_c. is assumed to be constant, and T_c is considered in the first approximation to coincide with T_c ($T_{гп}$). The condition for the applicability of (2) in [3, 7, 10) is assumed (in the dimensions of the SI system) the inequality

$$Fo_k = \frac{a\tau_k}{H^2} \le 0{,}106. \#(4)$$

which is fulfilled as equality when the temperature at the outer boundary of the body changes by 0,03 $|T_{ГП} — To|$. Here $a = \lambda/c\rho_0$

is the thermal diffusivity, H is the thickness of the material layer, which either changes in an obvious way, or requires some kind of averaging. The averaged values of H for cylindrical dryers are given in [7]. Through the criterion Fo_k , expression (2) can be represented in the form

$$< \alpha^k >_{\tau_k} = \frac{2\lambda}{H\sqrt{\pi Fo_k}}.$$

In many devices, the heating surface is often curved, and the limitations of the applicability of the short-term contact model may be determined not by the thickness of the H layer, but by the curvature of the heating surface R. Estimates of type (4), taking into account the curvature of the heating surface, will be obtained below. In addition, it is known that internal evaporation, thermal diffusion, filtration of moisture contribute to heat transfer, and (2) was obtained by solving the problem of pure thermal conductivity. Finally, the coefficient $< \alpha >$ is influenced by the composition of the remote multicomponent liquid mixture [11 - 15]. Taking these effects into account is an urgent task for the development of technological calculation and analysis of local changes in temperature and composition of the liquid phase of products. The physical model of short-term contact of phases is a powerful tool for analyzing transfer processes, since in a number of cases it has properties that make it possible to obtain relatively simple solutions of the posed boundary value problems, including multi-frontal problems of the Stefan type (freezing (thawing), evaporation, drying, filtration, sorption, adsorption , crystallization, etc.)

Mathematical models, self-similarity and invariants of solutions. In the general case, any mathematical description of processes in heterogeneous media, which include wet dispersed materials (suspensions), is based on the phenomenological theory of the multi-velocity continuum and is represented as a system of balance equations for conservation of mass, momentum, and energy. Further, depending on the considered medium and process, the multi-fluid (multi-velocity) model is generalized and closed (concretized) by attracting the mechanical and thermodynamic properties of the phases.

In the framework of nonequilibrium thermodynamics [16-17], on the basis of integral conservation laws, the interrelated heat and mass transfer in stationary dispersed media and capillary-porous bodies containing multicomponent liquid mixtures can be described using the following inhomogeneous system of nonlinear parabolic equations written in the vector-matrix form and resolved with respect to time derivatives (in this form, they are usually given by the system of differential equations of the transport theory).

$$C\frac{\partial \vec{\Pi}}{\partial \tau} = \mathrm{div}\left(L\mathrm{grad}\vec{\Pi}\right) + \vec{I}, \#(5)$$

where $\vec{\Pi}$ is the n-dimensional vector of transfer potentials, L is the matrix of kinetic coefficients, C is the diagonal matrix of capacitance coefficients, I is the power vector of sources (or sinks). If there is an interaction of two phases, then in (5) the index i = 1,2 is added, which we omit to simplify the notation, the operators of divergence and gradient are applied in (5) separately to each component of the corresponding vectors. It should be noted that system (5) can be written with respect to each of the interacting phases with the corresponding boundary conditions of uniqueness, including at the interface, similarly multi-frontal problems of the Stefan type. If the presence of sources is caused only by liquid-vapor phase transitions, and the vector of potentials includes the vector of moisture contents of the components Ux or the total moisture content U, then the vector I can be excluded from (5). To do this, it is sufficient to use the method of introducing the criterion of internal evaporation (phase transformation) ε, which is the ratio of the change in moisture content due to evaporation to its total change U_T. which is widespread in the theory of drying. In the case of an multicomponent liquid mixture, the ε values for the components can be different, this criterion will be a vector. After introducing e from (5), within the framework of the model of short-term contact of phases, we obtain

$$C\vec{\Pi}_T = \left(L_\varepsilon, \vec{\Pi}_x\right)_x, \#(6)$$

where L_ε is a matrix of kinetic coefficients that takes into account phase transitions. In the case when C and L_ε do not explicitly depend on coordinates and time (an explicit dependence on the complex $x/\sqrt{\tau}$ is admissible), but are functions of transport potentials, the Boltzmann substitution $\xi = \frac{x}{2\sqrt{\tau}}$ reduces (6) to a nonlinear system of homogeneous second-order ordinary differential equation

$$2\xi C\vec{\Pi}' + \left(L\vec{\Pi}\right)' = \vec{0}. \#(7)$$

Here and in what follows, the prime means differentiation with respect to ξ, and the subscript ε for L is dropped.

Using the assumption of the uniform distribution of $\vec{\Pi}$ at the time τ = 0, we obtain the boundedness condition as $\xi \to \infty$

$$\vec{\Pi}(\infty) = \vec{\Pi}_0. \#(8)$$

When formulating the boundary conditions in the form

$$P^{II} - \vec{\Pi}(0) = \vec{\Pi}_C \#(9)$$

(the task of linear relationships of the $\vec{\Pi}$ components on the heating surface) or

$$P^{II} \cdot L\vec{\Pi}'^{(0)} = \vec{0} \#(10)$$

(the condition of impermeability of the heating surface for certain flows) the entire problem of short-term contact of phases (7) - (10) becomes self-similar. In (9) P^1 and in (1.10) P^{11} are orthogonal projectors, not necessarily orthogonal to each other ($P^I \cdot P^{II} \neq 0$). In the case when the fluxes of energy or matter through the HP are specified, the condition for self-similarity is their proportionality $\tau^{-0.5}$[21].

When solving problems with equations of the type (6) in the region x > 0, τ > 0, most researchers use in addition to the initial and boundary conditions of semi-boundedness (or conditions at infinity) as $x \to \infty$ in three different forms:

$$\vec{\Pi}_x(\infty, \tau) = \vec{0}, \vec{\Pi}(\infty, \tau) = \vec{\Pi}_0, \lim_{x\to\infty} \vec{\Pi}(x, \tau) = \vec{\Pi}_0. \#(11)$$

The last two conditions in (11) for the self-similar problem coincide with condition (1.8), which reflects the initial state of the product. Therefore, additional conditions of semi-boundedness were not considered.

In the case of constants L and C, which is most studied in the theory of drying when removing individual liquids, the problem of short-term contact of phases becomes linear and greatly simplified. To solve such problems, the superposition method is often used [2, 6, 19]. Eigenfunction expansions and integral transformation methods provide systematic schemes for constructing such solutions.

If the matrix $C^{-1} \cdot L$ has real, positive and different eigenvalues v_i^2, $i = \overline{1,n}$, the solution (7) - (10) by the superposition method is reduced to finding the constants A_i in the representation

$$\vec{\Pi}(\xi) = \vec{\Pi}_0 + \sum_{i=1}^{n} A_i f_i \mathrm{erfc}\left(\frac{\xi}{v_i}\right), \#(12)$$

from the conditions on the heating surface (9) and (10). In (12), the linearly independent eigenvectors f_i of the matrix $C^{-1} \cdot L$ correspond to the eigenvalues v_i^2. Direct verification can make sure that when specifying $\vec{\Pi}(\xi)$ in the form (12), equation (7) and condition (8) are satisfied automatically.

The constancy of L and C is an idealization of real relationships, however, it provides rich material for a qualitative analysis of the influence of various parameters on the transfer process. At the same time, even without this condition, the model of short-term contact due to the self-similarity of the problem

(7) - (10) has great advantages. Self-similar solutions can be used as "standards" in evaluating approximate methods for solving more complex problems; in addition, self-similarity simplifies the calculation and presentation of the characteristics of the phenomenon. In particular, assuming only the existence of a solution $\vec{\Pi}(\xi)$ one can establish the existence of a series of invariants of internal heat and mass transfer.

An integral component of $\vec{\Pi}$ in a non-isothermal process is temperature T, and its change at any point in the material can be considered monotonic: $T_\tau(x, \tau) > 0$ during heating. Therefore, from the solution T (ξ), one can obtain a unique dependence ξ (T) and write $\Pi^{\rightarrow}(\xi)$ in the form

$$\vec{\Pi}(\xi) = \vec{\Pi}(T). \#(13)$$

Thus, in the theory of short-term contact of phases, there are n - 1 invariants of internal interconnected heat and mass transfer, according to the number of acting potentials that determine this transfer. The relationships between the local values of temperature, moisture content, composition of the multicomponent liquid mixture and pressure, which are independent of time and coordinates, can serve to analyze the combined effect of heating and dehydration in various technological processes.

Such an analysis is especially relevant for biological products, since their thermal and xerolability is due precisely to the combined effect of these factors.

In connection with the large role of the model of short-term contact of phases in the study of processes with stirring, a more detailed analysis of the limits of applicability of this model is required.

The limits of applicability of the model of short-term contact of phases. The conditions under which the contact can be considered short-term depend on what characteristics of the contact are being investigated. O. Krisher's restriction (4) is associated with a change in temperature on the free surface of the body by 3% of the total temperature head, and is used as a characteristic of the applicability of formula (2) for the heat transfer coefficient. It is of interest to elucidate the influence of the finiteness of body dimensions and the shape of the heating surface directly on the heat transfer coefficient. Let us consider in the framework of pure thermal conductivity the problems for an unbounded plate (G = 0), an infinite cylinder (G = 1) and a ball (G = 2) - Fig.2.

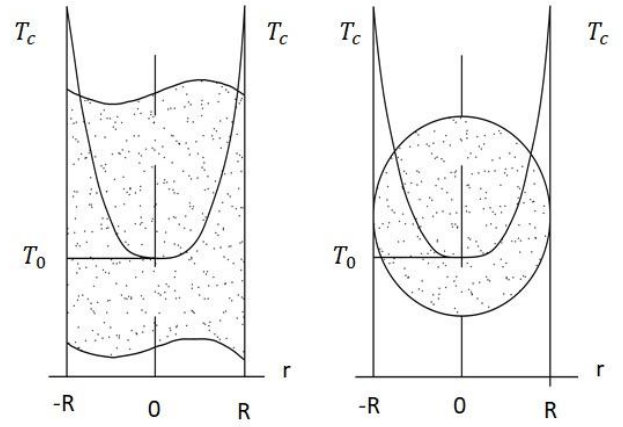


Fig. 2 On the formulation of heat conduction problems for bodies of canonical form

All three tasks have a common formulation

$$T_\tau - a\left(T_{rr} + \frac{\Gamma}{r}T_r\right) = 0, \#(14)$$

$$T(r,0) = T_0, \qquad T(\pm R, T) = T_c$$

and the same kind of solution [6]:

$$T(Fo,\eta) = T_c + (T_0 - T_c)\sum_{i=1}^{\infty} A_i \varphi(\mu_i \eta)\exp\left(-\mu_i^2 Fj\right), \#(15)$$

Where

$$\eta = \frac{r}{R}, \qquad Fj = \frac{a\tau}{R^2}, \#(16)$$

and μ_i- are the positive roots of the characteristic equation numbered in ascending order

$$\varphi(\mu) = 0.$$

The eigenfunctions of problems (14) and the coefficie - are determined by the formulas in Table. 1.

Table 1. Parameters of solutions for heat conduction

G	0	1	2
$\varphi(\mu_i\eta)$	$\cos(\mu_i\eta)$	$J_0(\mu_i\eta)$	$\frac{\sin(\mu_i\eta)}{\mu_i\eta}$
A_i	$(-1)^{i+1}\frac{2}{\mu_i}$	$\frac{2}{\mu_i J_1(\mu_i)}$	$(-1)^{i+1}\cdot 2$

Here J_0 and J_1 are the Bessel functions of the first kind of the zero and first orders, respectively. Taking into account the Fourier law, α (τ) is determined by the value

$$\alpha(\tau) = \frac{\lambda}{R(T_c - T_0)}T_\eta\big|_{\eta=1}. \#(18)$$

Formal term-by-term differentiation of series (15) at different G gives a general expression

$$\alpha(\tau) = \frac{2\lambda}{R}\sum_{i=1}^{\infty}\exp\left(-\mu_i^2 F_o\right), \#(19)$$

in which the shape of the heated body is reflected only through the sets μ_i i=1,2, ... Formal term-by-term integration (19) in accordance with (2) gives

$$<\alpha>_{\tau_k} = \frac{2\lambda}{RF_{ok}}\sum_{\cdot i=1}^{\infty}\frac{1-\exp\left(-\mu_i^2 F_{ok}\right)}{\mu_i^2}. \#(20)$$

A discussion of the convergence of series (19), (20) and estimates of their remainders are given in [1]. Note that the summation of these series in the problem of short-term contact of phases must be carried out at small F_o, when there is no predominance of the first terms. Therefore, the numerical calculation of the sums (19), (20) was carried out on the basis of a given maximum permissible relative inaccuracies $\delta = 10^{-3}$. Separate task is the calculation of several hundred roots J_0 (it is precisely these quantities that are necessary for $\delta = 10^{-3}$.. This problem was solved sequentially in i, starting with the value $\mu_1 \approx 2{,}4$. The iterative rule of false position was used, and for the localization of the roots, the segments

$$\mu_{i+1} \in \left[\mu_i + \pi - \frac{0{,}1415}{i}, \mu_i + 3{,}1416\right],$$

the position of which is associated with the almost periodic nature of the growth of μ_i [19]. Due to the precise localization of the roots, their values were calculated with a relative error of no more than 10^{-6} for 2 - 3 iterations, with this level of error it was possible to determine 250 roots. The results coincide with the above accuracy with the data [19], where the first 60 roots of J_0 with 5 - 7 significant digits are given.

However, it should be noted that the classical solution in the Fourier form, consisting of the product of two functions, taking into account, respectively, the change in temperature in time and along the radius (thickness), is convenient for large Fo. For small Fo, solutions obtained by methods of operational calculus are convenient, in particular, solutions in the Laplace form (Laplace transform), which represent the well-known combination of the functions erf and erfc. In these cases, you can always limit yourself to a few first (or only the first) members of the series, discarding all the rest. In addition, operational methods make it possible to obtain a number of approximate solutions with any degree of accuracy, which are quite simple and can be used in technical calculations.

An analysis of the obtained expressions $\alpha(Fo)$ for various G shows that

$$\lim_{F_o\to 0}\left[\frac{\alpha(Fo)}{\alpha^k(Fo)}\right] = 1,$$

those. the formulas for calculating α (τ) for small Fo asymptotically coincide with the formulas used to calculate $\alpha^k(\tau)$.

By generalizing (4) to. the case of multicomponent energy and mass transfer in a plate is the same condition, in which, instead of the thermal diffusivity (or diffusion) coefficient, one should use the largest of the eigenvalues of the matrix C^{-1} L [22]. Depending on the objectives of the study, the level of permissible fluctuations of various components II at the outer boundary x = II can be different, therefore, it is possible to weaken or strengthen condition (4), or a combination of this type of conditions. In a specific case, such estimates are carried out quite simply using solutions of the form (12).

The same approach is obviously extended to the case of contact between two plates of finite thickness. However, the very origin of the condition - guaranteeing the accuracy of the calculation of the potential fields in a plate of finite dimensions - has disadvantages. It is not connected with the main task of calculating energy and mass transfer with the determination of the intensity of metabolic processes and therefore does not say anything about the accuracy of calculating the fluxes of transported substances.

In addition, in real situations, a limitation associated with the curvature of the contact surface (the surface of a granule, a gas bubble, a cylindrical shell, etc.), and not with the surface of the dimensions of the contacting bodies, may be active. A significant limitation can also be the presence of two generators of length l during the contact time of the heat flux through the surface; consideration of the asymptotics as $k \to \infty$ and the subsequent approximation make it possible to determine the desired error.

When evaluating heat transfer from a cylinder of circular cross section and a sphere to the outer region, the solution was used [23]. In fig. 3 the calculated dependences of the ratio of the heat transfer coefficient to its base value calculated for the flat boundary of the half-space according to O. Krisher [3] are constructed.

As can be seen from the figure, the model of short-term contact of phases is suitable for estimating $< \alpha >_{\tau_k}$ at larger Fo than in the case of estimating $\alpha(\tau)$ - regardless of the shape of the heating surface. With an approximate coincidence of the characteristic size of the body H with the radius of curvature of the heating surface R, the applicability of the model of short-term contact of phases is limited precisely by the presence of the curvature of the heating surface. For roller dryers H << R it is necessary to analyze the influence of both factors. For dryers with flat heating surfaces - the applicability of the model of short-term contact of phases is determined by the thickness of the product layer. Fig. 3 it can also be seen that Krisher's constraint (4) is unreasonably strict for engineering estimates of heat transfer from a flat heating surface.

For example, for industrial drum and rake dryers, the τ_k value does not exceed 60 s. For a $= 10^{-7}$ м$^2/c$ and the radius of curvature of the heating surface R = 1 m, the corresponding $Fo_к$ do not exceed $6 \cdot 10^{-6}$, then is the influence of the curvature of the heating surface in accordance with table. 2 can be neglected. Taking the average thickness of the product layer H = 0.2 m, we get $F_o \leq 1{,}5 \cdot 10^{-4}$. Thus, for these dryers, the application of the short-term contact model can be considered justified.

The maximum thickness of the layer heated by 3% of the total temperature head, in accordance with (4), here is no more than 8 mm. However, for cabinet, roller, etc. devices with a small layer thickness H, the question of the applicability of the short-term contact model requires a separate analysis in each case. In the presence of a large number of mates of the heating surface with small radii of curvature, additional analysis based on table. 2 may be needed for drum and stroke.

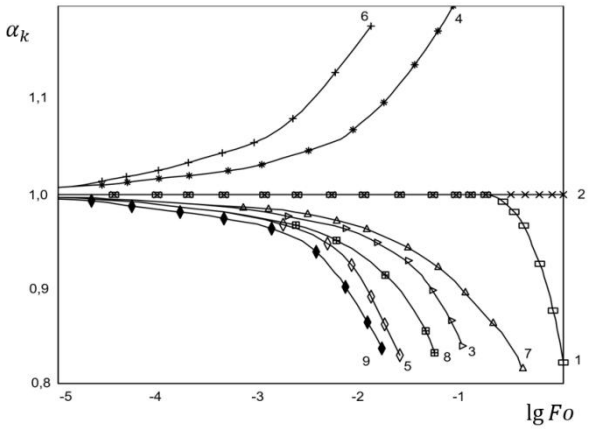


Fig. 3. The ratio of the calculated heat transfer coefficient to its value according to O. Krischer, depending on the Fourier number during heat transfer: 1.2 - respectively, into the interior and exterior of an infinite plate; 3.4 - into the interior and exterior of an endless cylinder; 5.6 - into the interior and exterior of the sphere; 7,8,9 - into the inside of an unlimited wedge with an opening angle of 150, 120 and 90 °, respectively.

Coefficient heat transfer	Heating surface shape	Plane		Cylinder		Sphere	
	Error level, %	3	5	3	5	3	5
$\alpha(\tau)$	$F_{0_{max}} \cdot 10^{-3}$	247	279	1,12	3,09	0,269	0,646
$\alpha(\tau_k)$	$F_{0k_{max}} \cdot 10^{-3}$	447	537	4,47	1,2	1,26	3,35

Table 2. The largest Fourier numbers at which the relative error in calculating α according to Krisher's formulas does not exceed 3% and 5%

When switching to multicomponent transfer, for a rough estimate, you can also substitute v_{max}^2 for a (or D). When considering the heat and mass transfer in two contacting phases, a more specific analysis is required, however, here v_{max}^2 plays a decisive role as well. devices.

3. Conclusions

The limits of applicability of the hypothesis of short-term contact of phases according to the Fourier criterion for the transfer inside and outside the surfaces of the canonical shape (plate, cylinder, sphere) and wedge are estimated from the standpoint of the accuracy of calculating interphase flows. It is shown that in a number of cases the contact is not short-lived due to the curvature and the presence of angles on the contact surface, and not due to the finiteness of the dimensions of the contacting phases.

Within the framework of linear nonequilibrium thermodynamics, a mathematical model of filtration-diffusion energy and mass transfer has been developed with a correct estimate of the orders of the terms in the system of differential equations of energy and mass transfer taking into account the composition of the vapor-air mixture in a capillary-porous body.

Depending on the value of the phase transformation criterion, the system of differential equations is simplified to three different systems of equations with the number of coupled equations in each no more than 2, describing the fields of temperature, humidity (concentration) and pressure, and the eigenvalues of the matrices of their coefficients are real, positive and different.

It has been established that during the transfer of a liquid, in the main one, in the form of vapor, the filtration-diffusion heat and mass transfer is expressed by the equations of diffusion heat and mass transfer with an increased coefficient of mass conductivity.

Boundary-value problems of diffusion and diffusion-filtration heat and mass transfer are solved under mixed boundary conditions of the first and second kind, on the basis of which integral kinetic dependences of drying processes (drying and heating rates), formulas for calculating heat and mass transfer coefficients, Rebinder numbers, temperature coefficients and subkinetic drying parameters.

Thus, a complex of theoretical and experimental studies has been carried out.

(using the methods of systemic, mathematical and numerical analysis, as well as general physicochemical and thermodynamic laws) transfer processes during short-term contact of phases (using the example of vacuum, conductive and combined drying methods), which made it possible to most fully reveal the laws of external and internal heat and mass transfer, to find scientifically grounded ways to intensify the considered processes

4. References

1. Sadykov R.A. Heat and mass transfer in vacuum drying processes and hardware design of the drying technology for labile biological products: Diss. ... Doctor of technical sciences. Kazan: 1990, 517s.
2. Lykov A.V., Mikhailov Yu.A. Theory of heat and mass transfer. M.-L .: Gosenergoizdat, 1963.536s.
3. Krisher O. Scientific basis of drying technique. Moscow: Foreign Literature, 1961.539 p.
4. Mathematical software for ES computers. Minsk .: Institute of Mathematics of the Academy of Sciences of the BSSR, 1973.
5. Strek F., Dudezak J. Modelowanie matematyczne procesu kontaktowego suszenia prozniowego materialow ziarnistyeh // Jn 2. Chem. 1974 V. 4, No. 3. P. 482-502.
6. Lykov A.V. Heat conduction theory. M .: Higher school, 1967.600 p.
7. Krasnikov V.V. Conductive drying. M.:. Energy, 1973.288 p.
8. Romankov P.G., Frolov V.F. Heat exchange processes of chemical technology. L .: Chemistry, 1982.288 p.
9. Zhuchkov P.A., Samoilo V.N. Experimental study of contact drying of various types of fibrous materials // In the book: Chemistry and technology of paper. L., 1982. Issue. 10.S. 38-44.
10. Lykov M.V. Drying in the chemical industry. Moscow: Chemistry, 1970.426 p.
11. Kheifets L.I., Neimark A.V. Multiphase processes in porous media. M .: Chemistry. 1982.320 s.
12. Palancz B., Parti M. Digital simulation of multi-component drying // Acta Technika Academia! Scientiarum Hungarical. 1975. V. 81, No. 1-2. P. 317-328.
13. Dayan A .. Self-similar temperature, pressure and moisture distributions within an intensely heated porous half space // International Journal Heat and Mass Transfer. 1982. V. 25, No. 10. P. 1469-1476.
14. Nigmatullin R.I. Dynamics of multiphase media: 2 hours. Moscow: Nauka, 1987. Part 1. 464 p.
15. Ovsyannikov L.V. Lectures on the basics of gas dynamics. Moscow: Nauka, 1981.368 p.
16. S. De Groot, P. Mazur. Non-equilibrium thermodynamics. Moscow: Mir, 1984.456 p.
17. Prigogine I. Introduction to the thermodynamics of irreversible processes. M .: Foreign literature, I960. 185 s.
18. Kvasnikov I.A. Thermodynamics and Statistical Physics. Theory of nonequilibrium systems. Moscow: Moscow State University Publishing House, 1987.559 p.
19. Tsoi N.V. Methods for calculating heat and mass transfer problems. Moscow: Energoatomizdat, 1984.414 p.
20. Yanke E., Emde F., Lem F. Special functions. Moscow: Nauka, 1977.344 p.
21. Kozdoba L.A. Methods for solving nonlinear problems of heat conduction. Moscow: Nauka, 1975.228 r.
22. V. V. Migunov The problem of heat and mass transfer in a short-time phase shift // IFZh. 1991, T. 60, No. 6, S. 955-963.
23. Carlslow G., Jaeger D. Thermal conductivity of solids. M., 1964.488s.

Numerical analysis of substrate influence on fracture mechanisms in PVD deposited TiN coatings

Bartlomiej Kowal, Konrad Perzynski, Lukasz Madej
Faculty of Metals Engineering and Industrial Computer Science, AGH University of Krakow, Mickiewicza 30 av., 30-059 Krakow, Poland
bartekkowal@agh.edu.pl

Abstract: *Coatings of titanium nitride (TiN) are widely used due to their high hardness and wear resistance, making them suitable for protective, decorative, and semiconductor applications. However, their tendency toward brittle cracking and low fracture toughness limits their performance in demanding environments. Understanding and accurately modelling fracture behaviour in TiN is therefore essential to improving reliability in microelectronics, protective coatings, or biomedical devices. This work presents a first approach to modelling fractures in TiN films by explicitly representing their columnar morphology. A procedure for generating statistically representative digital microstructures and incorporating them into finite element simulations is described. The approach uses a hybrid cohesive–XFEM fracture model to capture crack initiation and propagation under complex deformation states, particularly during nanoindentation. The numerical results are validated with results from a scanning electron microscopy (SEM) investigation.*
KEYWORDS: COATINGS, CZM, XFEM, FRACTURE MECHANISMS, OPENCV

1. Introduction

Nowadays, there is a growing demand for new methods to extend the functionality of devices used across key industrial areas. Therefore, composites comprising multiple thin films of conventional materials are increasingly used to improve the properties of the final product. One of the most popular techniques for creating these composites is the PVD (Physical Vapor Deposition) method. It consists of the material's target evaporation and its synthesis with the substrate, characterized by nanoscale accuracy in the creation of thin films and coatings [1]. Another technique used in this work is the PLD (Pulsed Laser Deposition), schematically shown in Fig. 1a. This method is based on laser ablation, which involves local evaporation of the target material using a laser beam. The plasma containing the material atoms is then transported to the substrate, where it condenses to form the thin film structure (Fig. 1b).

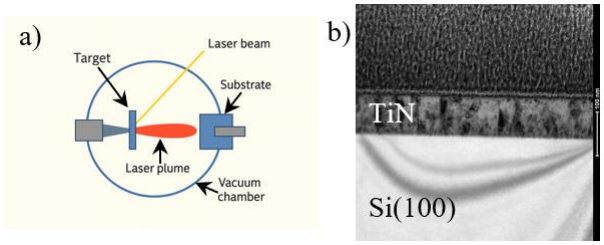


Fig. 1. a) Concept of PLD, b) TEM image of TiN film on Si(100) substrate.

2. Thin films morphology

Since the deposition process involves transporting plasma onto the substrate, the resulting morphology often depends on the chamber's operating parameters. Thornton's model has extensively described the possible film morphologies. This model is one of the basic diagrams illustrating the possible growth of the polycrystalline microstructure of thin films deposited physically from the gas phase [2]. The growth of the columns is represented as a map with four distinct zones, each corresponding to different column density and composition characteristics as shown on Fig. 2. The horizontal axis represents the ratio between the substrate temperature and the melting temperature of the deposited material.

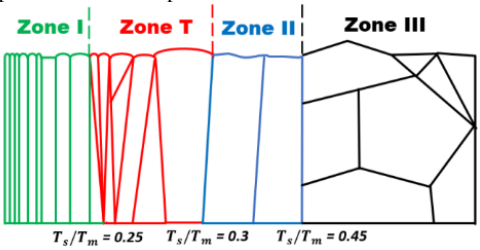


Fig. 2 Schematical illustration of Thorton's model.

Film behaviour under loading conditions is often evaluated using the nanoindentation technique. Since it probes extremely small volumes, nanoindentation is especially valuable for thin films and coatings where conventional mechanical testing is not feasible.

3. Numerical model of the nanoindentation test

As mentioned, nanoindentation is used to analyse the mechanical properties of films and coatings. It involves inserting a diamond tip of a specific shape into the material's surface while simultaneously monitoring the applied force and the corresponding displacement. From this data, information on the material's mechanical response can be extracted [3].

In this work, a numerical model for this test was created using a plug-in implemented in Abaqus CAE software, which automated the process of creating models ready for nanoindentation analyses. Based on this plug-in, a 2D planar model was created, including:

- Conical indenter with a spherical tip with a radius of 1µm, which was considered as an analytical rigid shell.
- Thin film 0.1µm thick and 15µm wide, consisting of 100 funnel-shaped columns representing film morphology, defined as a deformable shell.
- Substrate of the selected material, defined as a deformable shell with dimensions of 30×50µm.

Additionally, the concentrated force was applied to the indenter, with a value of 1 gf (0.0098 N). Fig. 3 illustrates the developed 2D model used to conduct numerical simulations of the nanoindentation process.

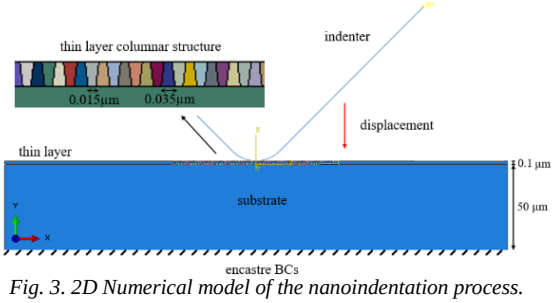


Fig. 3. 2D Numerical model of the nanoindentation process.

The aim of this work was to determine the crack characteristics of the Titanium Nitride (TiN) thin film deposited on 2 different material hardness bases: stainless steel (SS316L) and aluminum (Al 1050). Material data were derived from literature[4, 5]. A simplified rheological model of Swift-type hardening was used (1) $\sigma = (A + B \cdot \varepsilon^n)$).

$$\sigma = (A + B \cdot \varepsilon^n) \tag{1}$$

where: σ – yield stress, A – initial yield strength, B – strain hardening constant, ε – plastic strain, n – strain hardening exponent.

In the presented model, two numerical methods were used to model fracture mechanisms: the cohesion zone method (CZM) and the extended finite element method (XFEM). The CZM method is based on a traction-separation law that represents the fracture mechanism at the boundary of TiN microstructure columns (Fig. 4a) and at the delamination between the thin film and the substrate (Fig.

4b). The XFEM model depends on the maximum nominal stress at the crack tip and can predict fractures within the columns (Fig. 4c).

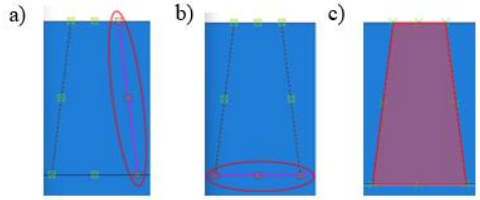


Fig. 4. Assignment of the CZM to a) intercolumn boundary, b) column-substrate boundary and XFEM to c) intracolumn area.

These models assume initial linear-elastic behaviour, followed by crack formation and propagation. To simulate fracture development, it is necessary to define a crack initialization and propagation criteria, in which the maximum nominal stresses (σ_{max}) and total displacement (δ_c) can be specified. These parameters were analytically determined using the critical stress-intensity K_{IC} factor calculated according to the formula (2) $K_{IC} = \sqrt{\frac{1}{2}\sigma_{\max}\,\delta_c E}$) [4]. Values for crack initialization and propagation are listed in Table 1.

(2) $$K_{IC} = \sqrt{\frac{1}{2}\sigma_{\max}\,\delta_c E}$$

where: E – Young modulus, $\sigma_{\max}$ – maximal nominal stress, δ_c – total displacement.

Table 1. Fracture parameters for crack nucleation and growth for CZM (intercolumn, delamination) and XFEM (intracolumn).

	CZM		XFEM
criterion	intercolumn	delamination	intracolumn
σ_{max} [GPa]	5	10	5.5
δ_c [µm]	1E-05	1E-05	1E-05

4. Simulation results

Numerical simulations were conducted using a hybrid (CZM, XFEM) method, which resulted in the formation of numerous cracks in thin TiN films on all base materials. Fig. 5 presents the result of combining both CZM and XFEM methods, where all three fracture mechanisms: intercolumnar, intracolumnar, and delamination are simultaneously visible.

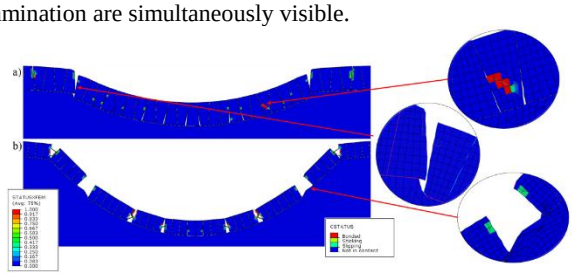
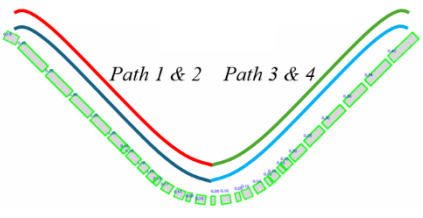


Fig. 5 Hybrid CZM and XFEM fracture model of a thin TiN film on a) SS316L and b) Al 1050.

The OpenCV library was used to develop a script that automates the verification of the dimensions of structures formed in a thin TiN film deposited on an Al1050 substrate after the nanoindentation simulation as presented in Fig. 6.



Structure no.	Width [µm]
1	0.15
2	0.4
3	0.35
4	0.3
...	...
27	0.05
28	0.1
29	0.05
30	0.1
mean	**0.168**

Fig. 6 Calculated widths of the structures after numerical simulation.

The average structure sizes in individual simulations were then compared with the average structure sizes obtained from 4 different paths, determined from SEM imaging of the sample surface after nanoindentation, as shown in Fig. 7.

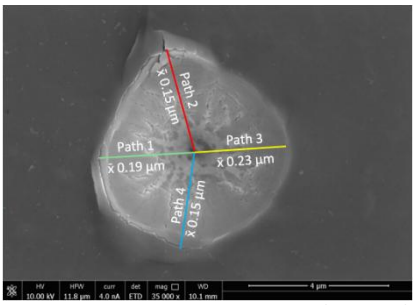


Fig. 7 Average TiN-Al 1050 structure sizes of 4 paths from [3].

Table 2 shows the accuracy of the simulation results compared to the laboratory results, calculated as the relative error.

Table 2. Calculated relative error of the mean structure sizes.

	Simulation 1	Simulation 2	Simulation 3	Simulation 4
Path 1	88.13%	96.86%	89.75%	69.72%
Path 2	87.78%	76.67%	85.71%	88.77%
Path 3	88.52%	77.48%	86.47%	88.18%
Path 4	71.94%	79.06%	73.26%	56.91%

5. Conclusion

The aim of this work was to demonstrate the potential of finite element method calculations in conjunction with OpenCV image analysis techniques to predict fracture in thin films.

The key factor enabling the observation of cracking was the development of a model representing the columnar morphological structure of a thin TiN film, in which cracks were modelled using CZM and XFEM methods.

The presented numerical method can be widely used in the virtual testing of thin films. Numerical simulations enable the prediction of the impact of various parameters, such as the thickness of deposited films, the properties of the base material, or the film's morphology, saving time and resources that would otherwise be required to conduct a series of costly laboratory experiments.

Acknowledgements. This study was conducted thanks to polish computing infrastructure PLGrid (HPC Center: ACK Cyfronet AGH) providing computer equipment and support under the computing grant no. PLG/2025/018413. Research was supported by the program "Excellence initiative – research university" for the AGH University of Krakow.

6. References

1. *S. M. Al Azar i M. Ahmad A., „Mechanical and physical methods for the metal oxide powders production," Metal Oxide Powder Technologies, pp. 169-187, 2020.*
2. *J. A. Thornton, "Influence of apparatus geometry and deposition conditions on the structure and topography of thick sputtered coatings" J. Vac. Sci. Technol. 11, pp. 666–670, 1974.*
3. *A. Paar, „NHT³ Nanoindentation Tester," Anton Paar GmbH, 2025.*
4. *K. Perzyński, G. Cios i Ł. Madej, „Prediction of fracture evolution in the TiN/Al thin films based on a full-field modelling approach," International Journal of Solids and Structures, Volume 283, 2023.*
5. *K. Perzyński, G. Cios i Ł. Madej, „Method of determination thin film hardening characteristics from the as-deposited sample with nanoindentation test and inverse analysis." Archives of Civil and Mechanical Engineering, Volume 25, 2025.*

CFD and Differential Evolution Optimization of an Air-To-Air Heat Recovery System for an Industrial Dryer

Oğulcan Sogut[1*], Y.Yağız Simsek[1], M. Baris Yildiz[1], Yusuf Sahinoglu[1], Nesrin Sen[1], Onur Cimen[1], I. Etem Saklakoglu[1-2]
KANSAN R&D Center, Izmir, Turkiye[1]
Ege University, Department of Mechanical Engineering, Izmir, Turkiye[2]
ogulcansogut@kansanmak.com

Abstract: *This study details the thermal and fluid dynamic performance analysis and geometric optimization of a compact plate heat exchanger designed for waste heat recovery in industrial drying systems. The objective is to preheat fresh process air (25°C) to a target temperature range of 65–70 °C by recovering heat from high-temperature exhaust air (84 °C inlet, 36,000m³/h flow rate). The methodology integrates fundamental thermodynamic assessment (LMTD and ε methods) with Computational Fluid Dynamics (CFD) for detailed flow and temperature mapping. Critically, a Differential Evolution (DE) algorithm was applied to optimize plate geometry, channel size, and profile arrangement, subject to a mass constraint, to maximize heat transfer. Results confirm that the optimized design achieves 18-25% natural gas savings and 27.5% higher efficiency compared to conventional systems. This hybrid approach validates the optimized heat exchanger as a highly sustainable and economically viable solution for industrial thermal management.*
Keywords*: HAET RECOVERY, THERMAL MANAGEMENT*

1. Introduction

Industrial dryers are significant energy consumers within manufacturing facilities due to their reliance on high-volume, high-temperature air. Operations across nonwoven, textile, paper, food, and chemical sectors incur substantial energy costs by utilizing fossil fuels (natural gas) or electricity for air heating. Drying is globally recognized as one of the most energy-intensive industrial processes, typically accounting for 10-20% of total industrial energy use in developed nations, primarily due to the necessity of supplying the latent heat of evaporation [1]. Furthermore, convective dryers often exhibit inherently low thermal efficiencies, sometimes below 50% [2]. Minimizing this energy expenditure is crucial for operational sustainability.

The exhaust air discharged at the end of the drying process typically retains substantial thermal energy, frequently ranging from 70-120 oC. This waste heat represents a potential recovery of 20-30% of the total process energy input [3]. Studies estimate that around 29% of the energy supplied to industrial dryers is often wasted or rejected as heat losses [4]. Historically, this energy is vented, resulting in economic loss and adverse environmental consequences, including elevated CO2 emissions. Effective heat recovery strategies are therefore vital, offering the potential to reduce the specific energy demand of drying processes by 20-80% [5].

This research focuses on the optimized design and analysis of an air-to-air heat recovery unit to exploit this waste energy. The system targets a process where 36,000 m3/h of 84 oC exhaust air preheats the fresh air supply (inlet temperature 25 oC) to 65-70 oC . This preheating action effectively reduces the thermal load demanded from the main burner, thereby significantly improving the system's thermal efficiency and contributing to the reduction of the carbon footprint.

While extensive studies address the general application of heat exchangers, research specifically targeting the geometric optimization of compact plate designs for high-flow industrial exhaust, coupled with both detailed CFD modeling and advanced evolutionary algorithms like Differential Evolution (DE), remains limited. Existing literature often relies on steady-state analytical solutions or focuses solely on fixed geometries. This paper distinguishes itself by employing a rigorous numerical approach, utilizing the DE algorithm to systematically optimize multiple geometric parameters of a high-capacity counter-flow heat exchanger, ensuring both thermal performance maximization and compliance with critical physical constraints (e.g., mass and pressure drop limits).

This paper details the combined theoretical, numerical (CFD), and evolutionary optimization approach used to develop this high-performance heat recovery system.

2. Methodology

2.1. System Configuration and Design Parameters

The heat recovery unit utilizes a compact plate heat exchanger configuration. It is constructed from 399 AISI 316 stainless steel profiles measuring 40×40×2 mm. A counter-flow arrangement is employed, where exhaust air flows externally over the profiles, and fresh air flows internally through the rectangular channels. This configuration inherently maximizes the Log Mean Temperature Difference (LMTD) for enhanced energy transfer. The design and operating parameters are summarized in Table 1:

Table 1: The design and operating parameters

Parameter	Exhaust Air (Hot Side)	Fresh Air (Cold Side)
Inlet Temperature	84∘C	25∘C
Outlet Temperature	75–76∘C	65–70∘C (Target)
Flow Rate	36,000 m3/h	18,000 m3/h
Pressure Drop	300–400 Pa	300–1000 Pa

The heat exchanger casing incorporates a 1.5∘ sloped bottom surface to facilitate gravity-assisted drainage of any condensation.

2.2. Thermodynamic Modeling (LMTD and Energy Transfer)

The LMTD method was used to calculate the average temperature difference (ΔTlm) driving the heat transfer (Q).
The LMTD calculation based on design temperatures is:
$LMTD=\ln(\Delta T2\Delta T1)\Delta T1-\Delta T2$

For the counter-flow design:
- $\Delta T1=Th,in-Tc,out=84\circ C-70\circ C=14\circ C$
- $\Delta T2=Th,out-Tc,in=75\circ C-25\circ C=50\circ C$

The resulting LMTD is approximately 29.2∘C.

The total theoretical heat transfer (Q) is calculated using the energy balance for the cold fluid (fresh air):

$Q=\dot{m}\cdot cp\cdot\Delta T$

With a mass flow rate ($\dot{m}$) of approximately 5.8 kg/s (derived from the 18,000 m3/h flow rate at standard air density) and a target ΔT of 45∘C, the theoretical heat transfer is Qtheoretical≈262.2 kW. Actual field measurements and optimized analysis target a recovered heat range of 120–135 kW.

3. CFD and Optimization

CFD analysis was performed according to the technical specifications of the resulting heat exchanger, and analysis data was obtained. Analysis attempts were made with different profile lengths, layout combinations, and profile offsets. These simulations were used to understand the flow and temperature distribution of the baseline heat exchanger geometry and to create an initial data set for the optimization process.

A Python code utilizing the Differential Evolution (DE) algorithm was developed to optimize the output of a mathematical model created based on specific physical parameters (x: number of vertical profiles, y: number of horizontal profiles, p: profile offset, L: profile length, and D: profile diameter); to best fit this model to the CFD (Computational Fluid Dynamics) results; and simultaneously to determine the optimum geometric and physical parameters that maximize heat transfer, while not exceeding a specific mass limit (approximately 1142 kg). The regression analysis data is presented in Table 1.

Table 1: The regression analysis data

	1S1	1S2	1S3	2S2	P2S3	P3S2	P3S3	P4S2	P4S3	P5S2	P5S3
Horizontal Profile Count (units)		0	4		6	6	6	6	6	6	6
Vertical Profile Count (units)					8	4	4	4	4	4	4
Profile Offset (mm)	0	0	0	0	20	30	40	20	20	20	20
Profile Length (m)					1	1	1	1.5	2	1	1
Circle Diameter (mm)	0	0	0	0	40	40	40	40	40	50	60
Q Heat Transfer Amounts (W)	161	875	430	340	8600	3946	3829	5919	7596	3907	3805

Regression analysis was performed using the analysis data in the table 1, and the following code was structured based on the results of this analysis.

Python

```
import numpy as np
from scipy.optimize import differential_evolution

# Constants
b = 1.5 # mm
rho = 7990 # kg/m^3

# Mass calculation function
def mass(x, y, L, D):
    x = int(round(x))
    y = int(round(y))
    A = (D * b - b**2) * 1e-6 # mm² → m²
    V = 4 * np.pi * x * y * L * A # m³
    return rho * V # kg

# Q function
def Q_total(x, y, p, L, D):
    x = int(round(x))
    y = int(round(y))
    q_x = -4.9688 * x**2 + 758 * x - 208.125
    q_y = 10.125 * y**2 + 988.25 * y + 46
    q_p = 0.49 * p**2 - 46 * p + 4885
    q_L = -202 * L**2 + 4041 * L + 322
    q_D = 0.76 * D**2 - 93.8 * D + 6697
    return q_x + q_y + q_p + q_L + q_D

# Objective function
def objective(vars):
    x, y, p, L, D = vars
    x = int(round(x))
    y = int(round(y))
    m = mass(x, y, L, D)
    penalty = abs(m - 1142) * 1000
    return -Q_total(x, y, p, L, D) + penalty

# Variable bounds
bounds = [
    (2, 10),     # x (integer)
    (2, 70),     # y (integer)
    (20, 30),    # p (mm)
    (1, 1.5),    # L (m)
    (30, 40)     # D (mm)
]

# Optimization
result = differential_evolution(
    objective,
    bounds,
    strategy='best1bin',
    maxiter=1000,
    tol=1e-6,
    seed=42
)

# Results
x_opt, y_opt, p_opt, L_opt, D_opt = result.x
x_opt = int(round(x_opt))
y_opt = int(round(y_opt))

m_opt = mass(x_opt, y_opt, L_opt, D_opt)
Q_opt = Q_total(x_opt, y_opt, p_opt, L_opt, D_opt)

# Print
print("\n--- OPTIMAL VALUES (x, y integer) ---")
print(f"x = {x_opt}")
print(f"y = {y_opt}")
print(f"p = {p_opt:.2f} mm")
print(f"L = {L_opt:.2f} m")
print(f"D = {D_opt:.2f} mm")
print(f"Q (heat transfer) = {Q_opt:.2f} W")
print(f"m (mass) = {m_opt:.2f} kg")
```

Key Results Obtained from CFD Analysis are shown in Table 2.

Table 2: Key Results Obtained from CFD Analysis

Parameter	***Value***
Fresh Air Outlet Temperature	313.57 K(≈40.4∘C)
Total Heat Transfer Rate	-120,412.22 W
Exhaust Air Outlet Temperature	341.98 K(≈68.9∘C)
Fresh Air Pressure Drop	1003.25 Pa
Exhaust Air Pressure Drop	377.89 Pa

The initial 40.4∘C outlet temperature shows that the baseline design did not meet the 65–70∘C target. This outcome highlighted the necessity for systematic optimization, providing the empirical foundation for the subsequent optimization phase. The reported Heat Transfer Rate (120.4 kW) represents the recovered energy in the unoptimized state.

3.2. Geometric Optimization via Differential Evolution (DE)

The low $T_{c,out}$ of 40.4 ^{o}C relative to the design target necessitated a systematic optimization of the heat exchanger geometry. The optimization problem was formulated to maximize the total

recovered heat (Q) while strictly adhering to dimensional and mass constraints, thereby minimizing the parasitic energy consumption (fan power) associated with high pressure drops [11].

The Differential Evolution (DE) algorithm [12] was employed to iteratively solve this constrained maximization problem. DE is a robust, population-based search technique well-suited for non-linear, multi-dimensional objective functions encountered in thermal system design.

The optimization problem is defined as:
Maximize Q(X) Subject to constraints

Where X is the vector of geometric design variables:
X = {x, y, p, L, D\}
(where x and y are integer-constrained profile counts, p is the offset, L is the length, and D is the profile diameter).

Objective Function and Constraints

The objective function f(X) was designed to maximize the heat transfer rate Q while penalizing solutions that violated the mass limit (Mmax):

Objective Function = Minimize [-Q(X) + C . max (0, M (X) – Mmax)]

Where:
Q(X): The heat transfer rate (derived empirically from CFD data).
M(X): The mass of the heat exchanger, calculated as a function of the geometric variables X.
Mmax approx 1142 kg: The maximum allowable mass constraint.
C: A large penalty constant to enforce the mass constraint [13].

The geometric boundaries for the DE search space were defined to ensure physical feasibility and are crucial for the algorithm's convergence efficiency. The constraints primarily focused on the maximum allowable mass and the maximum allowable pressure drop (Δ Pmax) across the fresh air circuit, as this dictates the size and power of the industrial fan [11].

The successful convergence of the DE algorithm identified the optimal combination of profile counts (x, y) and dimensions (p, L, D). This ensured the final heat exchanger geometry achieved the thermal target (Tc,out = 65-70 oC) while balancing the trade-off between heat transfer maximization and hydraulic performance (i.e., maintaining ΔP within acceptable limits). The resulting design represents a techno-economically optimal solution for industrial integration [13].

Graphical values for the designed heat exchanger are given in Figures 1-5, the Temperature Gradient is given in Figure 6, and the Inlets and Outlets of the Designed Heat Exchanger are given in Figure 7.

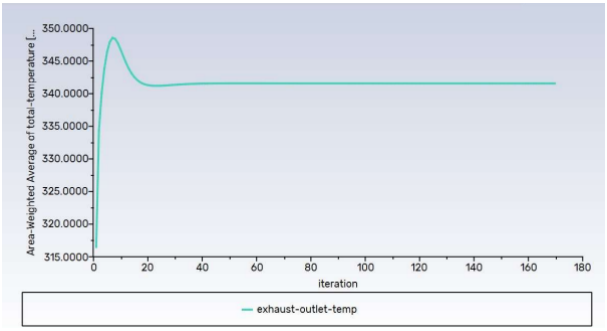


Figure 1. Exhaust Temperature Profile at the Outlet

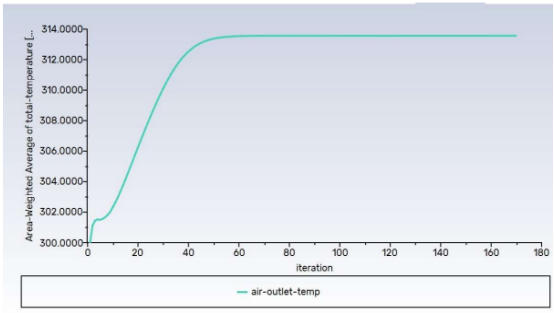


Figure 2. Fresh Air Temperature Profile at the Outlet

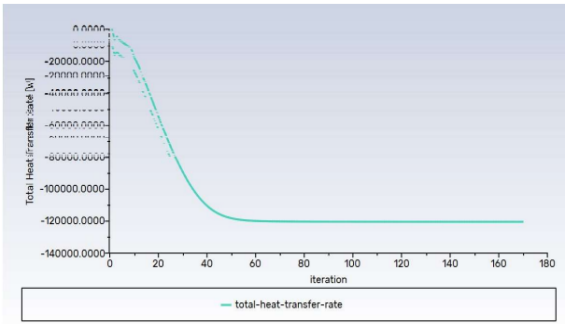


Figure 3. Total Heat Transfer

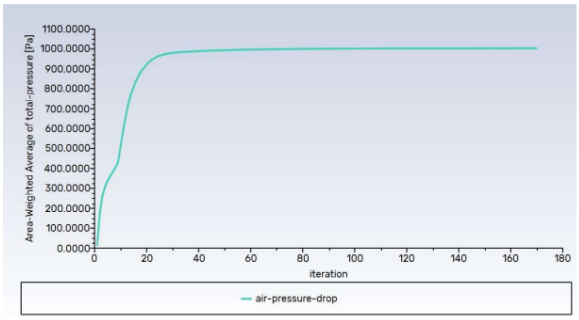


Figure 4. Fresh Air Pressure Drop

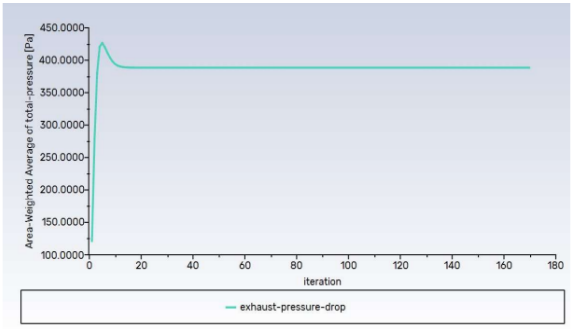


Figure 5. Exhaust Pressure Drop

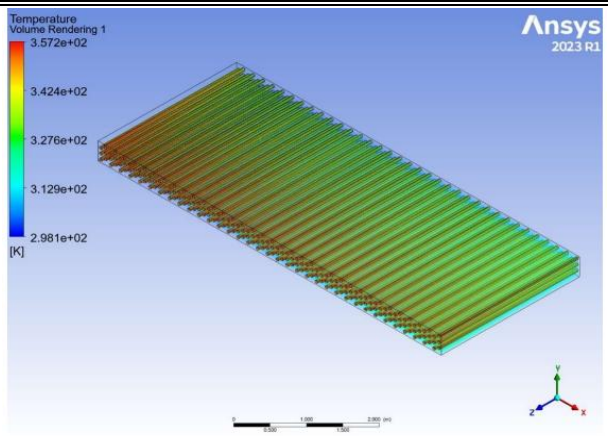


Figure 6. Temperature Gradient

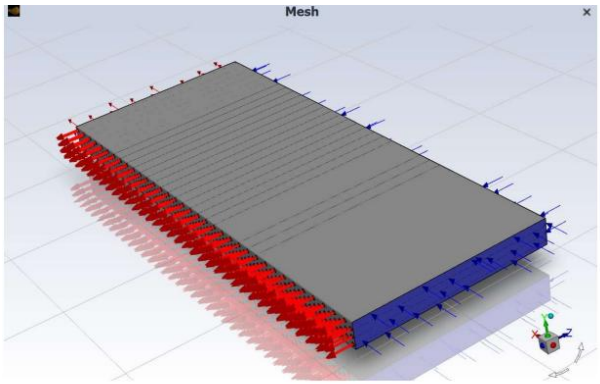


Figure 7. Inlets and Outlets of the Designed Heat Exchanger

4. Results and Economic Impact

The implementation of the optimized air-to-air heat recovery system results in significant energy savings and operational cost reductions.

1. Thermal Energy Savings:
The system provides a steady preheating capacity that corresponds to a 18-25% reduction in annual natural gas consumption. Furthermore, analysis shows that the optimized heat exchanger exhibits an efficiency improvement of 27.5% over older, non-optimized systems commonly used in the industry, highlighting the significant impact of the design methodology.

2. Economic Impact:
The substantial decrease in fuel consumption translates into annual energy cost savings estimated between 3000 – 600 0 € . Such rapid return on investment (ROI) is crucial for justifying the capital expenditure associated with the heat recovery unit [15].

3. Environmental Benefits:
The reduction in natural gas combustion directly leads to a 10-20% decrease in annual CO_2 emissions, significantly improving the environmental profile of the industrial operation and aligning the facility with sustainability goals [16].

The synthesized results confirm that the designed waste heat recovery system is an KANSAN innovative engineering solution that simultaneously addresses three key industrial concerns: energy cost reduction, process stability enhancement, and environmental mitigation.

5. References

1. Kudra, T. (2013). Energy in drying. Drying Technology, 31(15), 1746–1754.
2. Pu, W., Zhang, B., Chen, Z., & Zhang, H. (2020). Current status and development trends of industrial heat recovery technologies in China. Applied Energy, 259, 114138.
3. Zheng, X., Ma, Z., & Han, W. (2017). Economic and thermodynamic analysis of a waste heat recovery system for industrial drying processes. Energy Conversion and Management, 148, 1269–1280.
4. Jafari, M., & Zarrin, S. (2019). Optimization and energy analysis of a heat recovery system in a textile dyeing and finishing plant. Applied Thermal Engineering, 151, 100–110.
5. Mujumdar, A. S. (2014). Handbook of industrial drying (4th ed.). CRC Press.
6. M. Şekkeli ve Ö. F. Keçecioğlu, "Scada based an energy saving approach to operation of stenter machine in a textile plant using waste heat recovery system," Tekstil ve Konfeksiyon, cilt 22, sayı 3, ss. 248–257, 2012.
7. Çomaklı, K. (2011). Bölgesel Isıtma Sistemlerinde Atık Baca Gazının Ekserji Analizi. Enerji Verimliliği Dergisi, 17(2), 142–151.
8. Karanfil, G., Ruşen, S. E., Poyraz, Ş. N., & Can, M. (2020). Atık Isı Geri Kazanım Sistemleri ve Isıl Verim Parametrelerinin Deneysel İncelenmesi. European Journal of Science and Technology, 19, 127–137.
9. Terhan, M. (2015). Doğalgaz Yakıtlı Bir Kazanda Baca Gazından Enerji Geri Kazanımı ve Yoğuşma Olayının Enerji, Ekserji ve Ekonomik Yönden İncelenmesi. Doktora Tezi, Atatürk Üniversitesi, Fen Bilimleri Enstitüsü, Makine Mühendisliği ABD.
10. Yaman Karadeniz, N., Coşkun, S., & Can, M. (2007). Tekstil endüstrisinde atık ısı geri kazanımının plakalı eşanjör ve ısı pompası ile değerlendirilmesi. Enerji Kongresi ve Fuarı Bildiriler Kitabı, Bursa.
11. Wang, X., Li, X., & Liu, Z. (2018). Multi-objective optimization of plate-fin heat exchangers based on heat transfer performance and pressure drop. Applied Thermal Engineering, 137, 72-81.
12. Storn, R., & Price, K. (1997). Differential Evolution – A simple and efficient adaptive scheme for global optimization over continuous spaces. Journal of Global Optimization, 11(4), 341-359.
13. Hesselgreaves, J. E. (2015). Compact Heat Exchangers: Selection, Design, and Operation. Woodhead Publishing.
14. Shao, Y., & Li, Y. (2021). An economic and environmental assessment of waste heat utilization in industrial sectors. Energy, 235, 121307.
15. Ebrahimi, M., & Vafai, K. (2018). Economic and thermodynamic optimization of waste heat recovery systems. Energy Conversion and Management, 164, 452-463.
16. Wang, Q., & Li, Z. (2022). Reduction of carbon emissions by optimized industrial waste heat utilization. Journal of Cleaner Production, 350, 131460.

Statistical analysis of data on electricity generated from a small-capacity hydro power plant

Svilen Rachev[1], Milena Racheva[1], Lyubomir Dimitrov[1]
Technical University – Gabrovo [1], Republic of Bulgaria
srachev@tugab.bg

Abstract: *The widespread use of hydro power plants is well known. In addition to such plants that have been in operation for decades, there is currently an increased interest in the design and construction of new plants. In this regard, the accumulation of statistical data on the change in certain quantities and parameters for different periods of time and operating modes is important. On the other hand, subsequent processing of such accumulated data according to certain rules is possible. The main goal of this paper is statistical processing of data for a specific hydro power plant, in order to identify certain trends and prepare recommendations for improving activities.*

Keywords**:** *RENEWABLE ENERGY SOURCES, HYDROELECTRIC POWER GENERATION, GENERATORS, STATISTICAL ANALYSIS*

1. Introduction

The increased interest in renewable energy sources (RES) is driven by two key reasons – environmental sustainability and energy savings. Taking into account the rising and difficult to predict electricity prices, as well as the penalties associated with increasingly strict carbon emissions legislation, it is clear why in recent years the focus has been on the role of RES in reducing and/or stabilizing energy costs.

Sustainability is a multifaceted concept that is gaining increasing importance in our lives. The ways and practices to achieve it are green technologies – they can transform production and consumption patterns. European policies to promote renewable energy sources through legislative initiatives and financial instruments outline good prospects for hydro electric energy.

Water has been a traditional source of energy for centuries – look back to mills, fulling machines and other water-powered facilities. Harnessing its kinetic energy has been around for hundreds of years.

Hydro power plants (HPPs) convert the potential energy of water into electrical energy by driving a turbine. This type of power plant is relatively widespread in Bulgaria due to its mountainous terrain. The electrical energy produced by HPPs is included in the country's electricity balance.

Hydro power ranks first in the renewable energy sector and is expected to grow in importance worldwide over the next 10 years. Today, 70% of the world's renewable energy and 16% of total electricity are hydro power energy [1].

In Bulgaria, the share of electricity produced by HPPs is less than 20%. According to data from the Transmission System Operator (TSO), large HPPs generate approximately 14.37% of energy, and small ones – 2.66%. Currently, around 260 HPPs are operating in Bulgaria. In 2015, the total installed capacity of HPPs in Bulgaria was approximately 2,350 MW. By the way, it is believed that 2900 liters of water are needed to produce 1 kWh of electricity.

Hydro power is the world's largest source of green energy, overshadowing solar and wind. As such, hydro power enjoys a positive reputation in the media and in many academic papers. However, most of the 45,000 large dams worldwide are built for flood control, water storage, agricultural irrigation, fisheries, or recreation. Only about 25% of these facilities include hydro power.

As of 2019, the world's total renewable energy capacity stood at 2,351 GW, of which about half, or 1,172 GW, was hydro power. This includes both large dams and so-called run-of-river HPPs. Two-thirds of the world's major rivers are used for power generation. In Asia, dams construction is increasing, most of them enormous. This means deforestation, loss of land and wildlife, and changes in river patterns. As with other renewables, Asia is once again in the spotlight [2].

By the way, China has presented a plan to accelerate the implementation of artificial intelligence (AI) technologies in the energy sector. According to official documents, by 2027 the country should create an innovative system for integrating AI into the energy sector and achieve the first significant technological breakthroughs. By 2030, China intends to establish effective coordination between computing power and energy supply. It is planned to use AI technologies in the control of energy grids, the development of RES and nuclear power [1].

Experts emphasize that HPPs use only the kinetic energy of water. In fact, the power plants do not use any water resources, and after processing the appropriate amounts, they return to the riverbed. Hydro power engineers specify that the advantage of hydro power is not the price, but the zero carbon footprint of the process of its production.

For now, water remains among the most used RES in Bulgaria, and this is due to its wide application potential. Hydrological analyses show that Bulgaria is relatively poor in water resources. According to existing data, there are between 1600-2000 m^3 of water per capita per year. An advantage is the mountainous nature of a significant part of the territory. Thanks to this, the hydro potential, according to experts, reaches 26 billion kWh in an average runoff year. At the same time, the technically usable potential is within 57% of the theoretical one and is estimated at 15 billion kWh [3].

The existing technical and economic potential for the construction of large HPPs in Bulgaria is already almost exhausted or is unusable due to environmental protection considerations. This is one of the reasons for the increased investment interest in the construction of hydro power facilities with a maximum capacity of up to 10 MW, conditionally designated as small HPPs. Other reasons include the long period of operation of the facilities and the low costs associated with their production and maintenance, as well as the security of the investment, albeit with a relatively long payback period. Another advantage is the fact that small run-of-river HPPs do not use pre-reserved large volumes of water, thus avoiding the construction of a dam wall and the formation of a water storage basin.

The requirements regarding the quality of the electricity produced by small HPPs do not differ from the general requirements for other plants in the general energy system. In order to obtain maximum power from small HPPs, it is necessary for the turbines to operate at the maximum possible head, which requires, on the one hand, maintaining maximum volumes in the upper water storage basin (if any), and on the other hand, effective regulation of the hydro power units. With a relatively constant schedule of energy consumption, the production of electricity from small HPPs can easily be automated, thereby achieving higher efficiency.

2. Advantages and disadvantages of small hydro power plants

In addition to relatively low capital investment, small HPPs are also characterized by lower requirements regarding safety, automation, production cost, purchase price and personnel qualification. These characteristics predetermine the possibility of quickly starting construction and investing capital in the long term with minimal financial risk.

Small HPPs can be built on running waters, on drinking water pipes, on the walls of dams, as well as on some irrigation canals in the hydro-ameliorative system. They are suitable for users remote from the electricity grid. In addition, they are relatively easy to connect to the energy grid.

Another very important advantage of HPPs is that of all traditional energy sources, they start producing energy the fastest. It literally takes 2 to 5 minutes for a HPP to run and start generating energy. Hydro power plants, compared to other types of power plants, have much higher maneuverability. They start and stop quickly and can be loaded to their rated power in a short time, i.e. they can operate with power from zero to rated. Therefore, they have a special importance as a reserve and are very suitable for controlling the frequency and power in the electric supply system.

A disadvantage of small HPPs is their strong dependence on rainfall. As a result, they have a low rate of runoff utilization (up to 60%). Last but not least, their energy production must comply with the irrigation or water supply schedule when they are built in such systems.

Sometimes a very large length of the river is radically changed after the construction of a HPP. In recent years, many studies have come out that show that there is practically no dam that does not have an impact on fish. No fish passes have a 100% success rate. The other thing is that the water downstream changes – it becomes colder, with less oxygen or with variable quality, or with variable temperature, which, of course, affects all the organisms that are inside the river further downstream. And a very serious effect of HPPs is that downstream the sediments and the various chemical elements that are in the water are stopped by the dams and accordingly one of the very characteristic effects is that, for example, there is not enough sand to accumulate around the deltas of the rivers.

On the issue of HPPs – on the one hand, we need energy, on the other hand, these facilities must be built competently and not impact nature.

3. Potential for development of the hydro power plant energy branch

A number of expert analyses indicate that in Bulgaria there are about seven hundred sites with technological possibilities for the construction of small run-of-river HPPs. Most of them are located on mountain rivers, where the water quantities are larger and more constant over the years, despite the lower water pressure. Suitable sites are also provided by about one hundred water supply dams for the construction of sub-dam HPPs. However, the most attractive are small HPPs located on derivation systems. The reason is that when the relevant system is a water supply one, a constant water quantity and fixed hourly usability are ensured. There are also opportunities for installing hydro power equipment on water supply systems and wastewater treatment plants, which usually have a significant hydraulic head.

Hydro power plants use the most efficient technology for generating energy with high conversion efficiency and rapid recovery of the capital used to build the system. However, there is a need for small but significant improvements in technological development in many areas.

If the assessment of a given HPP shows that its condition is unacceptable, it is necessary to take the most appropriate actions to eliminate the problems. There are three options for this – repair and maintenance, modernization or reconstruction. When a given power plant reaches the age of 30-40 years, it is a good idea to carry out a study for possible modernization of the equipment and components. Advances in technology allow increasing the efficiency of turbines in many existing HPPs.

In many cases, the modernization of old HPPs is more expedient than the construction of new ones – the costs, environmental impact, social impacts and implementation period are relatively smaller. The renovated HPPs have increased power and efficiency. This includes completely new turbines, overhauled generators, and completely replaced hydraulic control and lubrication systems, which are modern and use less energy. They are more environmentally friendly and easier to maintain, which leads to fewer accidents.

Replacement of equipment (e.g. turbine impellers, generator windings, excitation systems, turbine governors, control panels, etc.) can provide higher efficiency, reliability and flexibility, as well as reduced operating costs. Overall, the potential for improvements in the rated power of existing HPPs is between 10 and 30%. It is financially justified to carry out modernization of hydro electric turbines, which will lead to an increase in efficiency by 4-8%. That is, it is reasonable to invest in modernization of existing facilities to produce more energy, rather than building new ones.

The main goal of power system control is to maintain a balance between production and consumption for a period of several seconds to years ahead. This requires ensuring the necessary reserves and system services from power plants in real-time control; short-term (hours, days) and medium-term (weeks, months) planning of the power system operation, as well as the development of long-term (years, decades) plans for the development of the power system.

The basic balancing and regulating capacities in the electric power system of Bulgaria are the large HPPs. During the spring high water freshet, increased electricity production from the HPPs is dispatched. During the summer season, the operation of the HPPs is entirely subordinate to the schedules for irrigation, drinking and industrial water supply, as well as to the ecological needs for moistening the riverbeds. Depending on the climatic conditions during the winter and autumn seasons, the HPPs operate to cover the electrical loads.

In addition to HPPs, priority production capacities include high-efficiency cogeneration and other RES (wind power plants, photovoltaics, biomass, etc.). The increase in the share of RES will strengthen the role of hydro electric power in managing fluctuations in wind power generation.

Investment in HPPs is not a ‘goldmine’ from yesterday. The beginning of the great interest in the hydro power business in Bulgaria dates back to 2002-2003, when the order for the construction of small HPPs was changed and a real boom in the issuance of construction permits occurred. The great interest in this business is dictated by the preferential purchase prices of this type of electricity from a renewable source. It is important that the hydrology in a country is relatively good. That is, there is a certain amount of water, and also high mountains, so the water can gain speed and strength. This way, more energy is obtained from less water, which increases efficiency. In case there is no high head, it can be created constructively through the water flow in an artificial way.

Nowadays, building a HPP costs a lot of money – from €0.5 million upwards. But once built, the plant receives preferential purchase prices for certain years ahead and a good profit is guaranteed.

In addition, the owner of the HPP simply receives the river terrain for eternal free use, since rivers are public state property and cannot be acquired by private individuals and companies. They are not even given out for concession. Thus, the owner of the HPP does not have to invest in land, like the owner of photovoltaics or wind generators, who must also change the purpose of the terrain.

The only annual cost paid to the state is the fee for the river water used, which is insignificant. For a plant producing about 0.5 MW and generating revenue from the sale of electricity during the year for about €100,000, the fee for the water used is only approximately €1,000. The preferential purchase prices are formed so that the investment for the HPP is returned over a period of 8-12 years, assuming that all requirements are met.

In summer, the operation of HPPs is limited due to the reduction of water in the rivers. However, many of them still work – they close the sluices, fill a water tank of a certain volume, including the pipe to the power plant, work for 1 hour, then collect water for 5 hours again. In fact, the power plants work on pulses (urges), which dry up the river not only between the water intake and the power plant building, but also do not release any water downstream. In summer, you can see many rivers with "working hours", which flow at intervals due to illegally operating HPPs.

According to some opinions, it is mandatory to immediately proceed with the preparation of an impact assessment of the already built HPPs on a national scale – from a hydrological, hydrotechnical and hydrobiological point of view, in order to establish what the effects are, what the benefits are and what the harms are. Only then will it be normal to carry out new design and construction with some benefits for society, and not just for the owners.

4. Describing of the considered hydro power plant

Pursuant to the Law on Energy from Renewable Sources (based on relevant acts of European legislation - directives and regulations, in force from 03.05.2011) a preferential price is set for the purchase of electrical energy produced from RES, including electrical energy, produced by HPPs with a total installed capacity of up to 10 MW. Hydro power plants with an installed capacity greater than 10 MW are not treated as RES, because other phenomena occur with them – e.g. change of the local climate in the presence of dams, etc. [4].

The Tazha HPP in question, with an installed capacity of 4.9 MW, was built to produce electricity and is a source of revenue for National Electric Company JSC, Bulgaria [5].

With its carbon-neutral energy production from one of the key renewable sources – water, National Electric Company JSC contributes to the achievement of the ambitious goals of Bulgaria and the European Union to achieve climate neutrality. With the energy produced by the HPPs, National Electric Company JSC is the largest producer of electricity from RES in Bulgaria.

National Electric Company JSC owns 31 hydro power plants (28 HPPs and 3 pumped storage hydro power plants, PSHPPs) with a total installed capacity of 2 737 MW in turbine mode and 931 MW in pumped storage mode. Before the privatization of HPPs in Bulgaria began in 2000, National Electric Company JSC owned a total of 73 HPPs. It turns out that HPPs are a very sought-after commodity on the market.

National Electric Company JSC plays a crucial role in ensuring the country's electricity security. Large HPPs play a significant role in the control of the electricity system. They are the main regulating capacities in Bulgaria. They balance the operation of the only nuclear power plant (NPP) and thermal power plants (TPPs) to date the variable loads of solar and wind power plants, as well as household consumers. Their main advantages are flexibility in system control and reliable mastery of peak load fluctuations, security and speed in replacing emergency shutdown capacities, primary and secondary frequency and exchange capacity regulation, and voltage regulation.

With the capacities from HPPs, National Electric Company JSC actively participates in the regulated, free and balancing markets and in the control and regulation of the energy system of Bulgaria. With energy from HPPs, National Electric Company JSC guarantees on the regulated market the security of supplies to end suppliers to meet the consumption of household and business customers connected at low voltage. On the free market, the company trades on all platforms of the Independent Bulgarian Energy Exchange (IBEX), founded in January 2014. In the balancing market, National Electric Company JSC-owned HPPs and PSHPPs are a major player with their fast-reacting capacities and wide coverage range.

With the development of the liberalized market, National Electric Company JSC's commitments as a public supplier of electricity for the regulated market will decrease, which will also allow for optimal use of the opportunities of HPPs and PSHPPs on the free market [5].

The Tazha HPP was built on the Tazha River, near the geographical center of Bulgaria. The idea for the construction of the plant was conceived by the Gramada Water Company, city of Gabrovo, Bulgaria. The stage of in-depth studies was before 1944. The construction itself began in 1945. The turbines were ordered from the Italian company SAN GIORGIO GENOVA-SESTRI. The construction of the Tazha HPP and its hydro technical facilities lasted from 1945 to 1951. In 1951, the water of the Tazha River was diverted and released through the diversion and the pressure pipeline. Water samples were successfully carried out. In December 1951, the turbines were put into operation for 72-hour tests, and on January 1, 1952, the power plant was put into operation. The generated electricity is transmitted by a 20 kV power line to the Kazanlak substation.

There are four water intakes – the Tazha River, the Babka River, the Dalboka River and the Svetishka Vada River. A water intakes coordinates (decimal): 42.688305, 25.038916; 42.683388, 25.038749; 42.688305, 25.038944; 42.674721, 25.054333. Water catchment elevation: Tazha River catchment at elevation 699.75 m; Dalboka River catchment at elevation 704.15 m; Babka River catchment at elevation 699.50 m; Svetishka Vada River catchment at elevation 699.0 m. Minimum water quantity after the water intake (liters/second): 438 – Tuzha River, 64 – Babka River, 69 – Dalboka River, 48 – Svetishka River.

The Tazha HPP has a water storage basin with an area of 25,458 m² and a net head of 150 m at an elevation of 534.5 m – Fig. 1. The Tazha HPP is a 4.9 MW power plant with three hydro groups. Annual electricity production: 10 000 – 15 000 MWh (1999 – 15 271 900 kWh; 2000 – 9 712 020 kWh; 2001 – 10 532 604 kWh). The plant has a permit to use water up to 4,000 liters/second from a water storage basin with a total volume of 40,000 m^3. The water storage basin and derivation channels of the Tazha HPP fall within the territory of the Central Balkan National Park [6].



Fig. 1 *Water storage basin of Tazha HPP.*

The technical basis of this HPP is as follows:

- ✓ own buildings (machine room, control room and substation);
- ✓ hydro facilities – pressure pipelines and channels – Fig. 2;
- ✓ energetic machines – hydro groups; control panel, measurement, protection, automation and signaling; indoor switchgear; transformers – 2 units; battery with rectifier for excitation of the generators**;**
- ✓ measuring instruments and tools.

The power part with hydro groups consists of:

- ✓ three Francis type horizontal axis turbines; one turbine has a design capacity of 2 540 kW, and the other two have a capacity of 1 265 kW each;
- ✓ three synchronous generators;
- ✓ two power transformers with rated power 5 600 kVA;
- ✓ indoor switchgear 20 kV.



Fig. 2 *Pressure pipeline of Tazha HPP.*

These three hydro groups are located indoors, in an machine room. The primary electrical circuit of the Tazha HPP is based on the 'generator-transformer block' principle.

Generator data:

- ➢ Generator 1: rated apparent power S_n = 3 440 kVA;

  rated voltage U_n = 6.3 kV; $\cos\varphi = 0.7$;
- ➢ Generator 2 and Generator 3: rated apparent power S_n = 1 720 kVA; rated voltage U_n = 6.3 kV; $\cos\varphi = 0.7$.

Each hydro group comprises a turbine, a synchronous generator, a line, a step-up transformer. Parallel work to the country's electric energy system is carried out on 20 kV buses to operator of the electric distribution grid EVN Bulgaria.

The excitation system of synchronous generators currently uses static thyristor exciters. Each exciter provides:

- ✓ automatic excitation supply when the generator is connected to the grid using the self-synchronization method, as a function of the frequency and phase of the electromotive force lag in the excitation winding;
- ✓ excitation supply during idle running of the generator when the exciter is powered from the own needs grid;
- ✓ maintaining a constant set excitation current with an accuracy of ±5% when the supply voltage fluctuates within the range of 70 to 110% of the rated and changes in the rotor temperature;
- ✓ local control of the set value of the excitation current in the range from the minimum to the rated excitation current;
- ✓ maintaining operability during short-term (no more than 60 s) changes in the supply voltage within the range of 50 to 140%;
- ✓ boosting excitation in case of emergency reduction of 10 to 15% of the rated value of the stator voltage;
- ✓ limitation of minimum and maximum excitation current.

In 2016, after an auction with offers held by National Electric Company JSC and selection of a contractor, turbine equipment was delivered for Hydro generator 2 of the Tazha HPP for rehabilitation purposes – polymer anti-friction self-lubricating materials, friction clutches, bronze pipe and stainless steel blanks for the reconstruction of the depreciated guiding apparatus of the hydro generator.

On September 18, 2024, a public procurement contract has been announced by National Electric Company JSC with the subject 'Supply of a three-phase transformer 20/6.3 kV, 3.15 MVA for the Tazha Hydro power Plant for the purpose of replacing the transformer for Hydro generator 1', which unfortunately, for a number of reasons, has been terminated on January 10, 2025. The problem is that any transformer operating at idle has losses that are greater if the transformer is over-rated, as is the case here.

Each power transformer is one of the most important electrical equipment in the power system and reducing power loss is of great economic importance for the power grid. Among the main directions in the improvement of power transformers is the reduction of losses.

No-load losses occur in the transformer core whenever the transformer is energized (even when its secondary winding is open, i.e. when it is not connected to any load). They are also called core losses and are constant. They consist of hysteresis losses and eddy current losses. No-load loss is a very important value, representing a significant amount of energy loss over the life of the transformer and unnecessary costs. Therefore, no-load losses should be minimized as much as possible.

No-load losses occur mainly due to the following reasons:

- ✓ core losses: the main component of no-load losses that occurs in the core is mainly due to hysteresis and eddy current losses;
- ✓ parasitic losses: although the proportion of these losses is relatively smaller, they contribute significantly to the total no-load loss; parasitic losses are created by stray eddy currents or confined magnetic fluxes and their impact on the total energy consumption can accumulate over time;
- ✓ flux distribution: uneven magnetic flux distribution can seriously affect core losses and magnetizing current.

Newly manufactured transformers have reduced components of all power losses, with particularly low no-load losses. Thanks to the development of magnetic materials, power losses are significantly reduced. Manufacturers choose high-quality and highly magnetic silicon steel sheets or even amorphous alloys as magnetic materials. This ensures uniform distribution of the magnetic flux and minimal noise during operation.

The no-load current is a basic parameter, and at no-load it is equal to the magnetizing current. It has a highly inductive nature and this is natural, since without consumption on the secondary side the transformer is one large choke (coil with a core). The no-load current as a value is 1-10% of the nominal current of a given transformer.

Reactive power losses in transformers also have two components: losses from the dissipation of the magnetic flux in the transformer ΔQ, depending on the square of the load current, and losses caused by the magnetization of the transformer ΔQμ, independent of the load current.

The last losses (magnetic) can be determined from the technical passport data using the no-load current i_{nl} and the rated apparent power S_{rated}:

$$\Delta Q_{\mu} = i_{nl} \frac{S_{rated}}{100}, kVAr \qquad (1)$$

The most commonly used static electronic electricity meters measure active and reactive power, as well as their sign, that is, the direction of energy flow. As a conclusion in this case – it is necessary to minimize all types of losses affecting monthly and annual energy payments.

What is the difference between reactive power and active power? Active power, also called real power, is the power that does the actual work. Reactive power comes from a variety of sources. Synchronous generators and capacitor banks are the main providers. Synchronous generators produce reactive power as part of their operation, while capacitors store it and release it when needed. Inductive loads, such as induction motors and transformers, also play a role by consuming reactive power.

Reactive power helps the grid operate more efficiently. When the grid does not have enough reactive power, it has difficulty transferring active power efficiently. This inefficiency leads to higher energy losses during power transmission.

Reactive power plays a critical role in electrical power transmission and distribution systems. It helps maintain voltage levels, ensuring the smooth flow of electrical power through the grid. Without it, there will be voltage instability and inefficient power transmission. With the increasing importance of RES, reactive power control becomes even more important for a stable and reliable electrical supply.

The production of active and reactive power by synchronous generators is regulated in several ways. Active power in synchronous generators is regulated by changing (increasing or decreasing) the mechanical power that the turbine supplies to the generator. Reactive power is regulated by changing the excitation current in the rotor – if the excitation current is greater than required, the generator supplies reactive power to the grid, if the excitation current is less than required, the generator consumes reactive power from the grid (operates in inductive load mode).

The production of active and reactive power is interrelated. When the synchronous generator is overloaded with active power, the generator voltage may drop if the excitation is not regulated properly, which requires correction of the excitation current. In principle, any rotating electrical machine is reversible and can be used as a generator or a motor. If the driving machine (turbine in this case) fails (shuts down), the generator continues to rotate as a synchronous motor, powered by the grid to which it is connected.

Renewable energy sources such as wind and solar are vital for a sustainable future. However, their variable nature creates challenges for grid stability. As renewable energy is increasingly connected to the grid, reactive power control becomes essential to maintain reliability and prevent power outages.

Table 1 below presents data on the generated and sold active and reactive energy for a period of two years. On Figure 3 and Figure 4 the changes in generated active and reactive energy by year are depicted.

Table 1: *Active and reactive energy sold.*

Month	Active electric energy sold, kWh	Reactive electric energy sold, kVArh
January I year	206 680	109 080
FebruaryI year	479 390	119 130
March I year	986 050	173 670
April I year	1 916 120	99 040
May I year	1 557 300	143 530
June I year	767 880	416 240
July I year	394 700	100 470
August I year	8 040	100 470
September I year	206 680	111 950
October I year	146 400	127 740
November I year	146 690	117 694
December I year	213 860	109 080
January II year	236 820	91 140
FebruaryII year	566 940	107 650
March II year	1 952 000	218 170
April II year	3 258 120	126 300
May II year	1 564 470	28 700
June II year	1 198 470	47 360
July II year	957 340	47 360
August II year	2 264 890	364 560
September II year	957 340	186 590
October II year	117 690	57 400
November II year	1 530 020	28 700
December II year	1 571 650	258 350

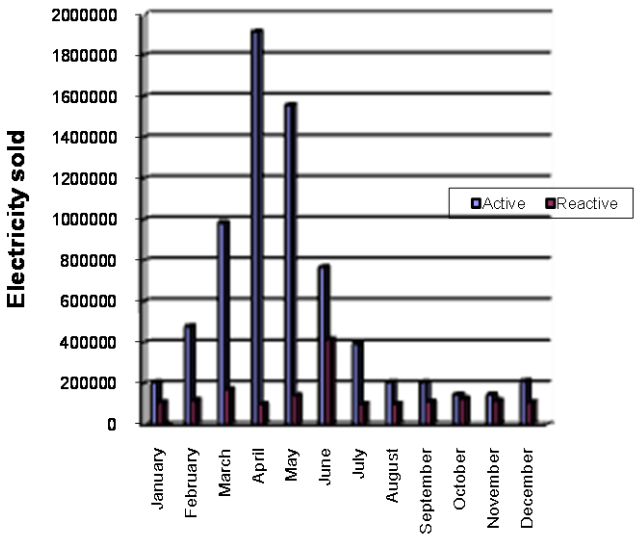


Fig. 3 *Chart of electricity sold by month for the first year, [kWh].*

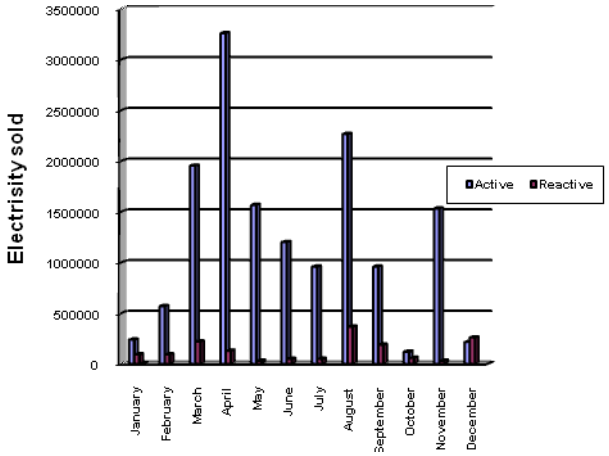


Fig. 4 *Chart of electricity sold by month for the second year, [kWh].*

The HPP in question has obviously produced and continues to produce reactive energy over the years, when necessary, according to the requests of the responsible operator.

5. Summary indicators for statistical processing of registered data

Mathematical statistics is applied as a tool facilitating the carry out of scientific research and the accumulation of data in the field of technology. Statistical methods are applied in a wide range of fields, such as the natural, social and engineering sciences, public administration, and business [7].

Cumulative data can generally be thought of as measurements of certain properties of objects selected from some large *population*. Information on certain characteristics of the elements is registered by *sampling*. Elements of the population are the so-called *statistical units* [4, 8, 9].

With the help of *samples* from measurements, some statistical indicators are determined, which are used to draw conclusions about some quantitative characteristics or parameters of the source *population* from which the sample was taken.

Position characteristics

There are several characteristics of the state of the empirical data population [9]. The most common is the *arithmetic mean*

value. In short, the *arithmetic mean* is the value about which the entire empirical distribution can be "balanced".

For ungrouped data $x_1, x_2, \ldots\ldots x_n$ the *arithmetic mean* is,

$$\bar{x} = n^{-1}.\sum_{i=1}^{n} x_i \qquad i = 1,2,\ldots\ldots n \tag{2}$$

As a characteristic of the position, a *geometric mean* value can also be used. In the case of sample volume n, the *geometric mean* is defined as:

$$\bar{\sigma} = \left(x_1 x_2 \ldots\ldots x_n\right)^{\frac{1}{n}} \tag{3}$$

Dispersion characteristics

One of the most commonly used characteristics of data dispersion is *arithmetic mean deviation δ.* For ungrouped data it is calculated this way:

$$\delta = \frac{\sum \left| x_i - \bar{x} \right|}{n} \tag{4}$$

Another characteristics of data dispersion is the *mean square deviation*. First, the square of this quantity, called the *variance*, is determined.

For a sample of ungrouped data, the *variance* is defined as:

$$s^2 = \frac{\sum_{i=1}^{n} \left(x_i - \bar{x}\right)^2}{n-1} \tag{5}$$

The *mean square deviation* is defined as the positive square root of the variance. For ungrouped data:

$$s = \sqrt{\frac{\sum_{i=1}^{n} \left(x_i - \bar{x}\right)^2}{n-1}} \tag{6}$$

6. Results obtained

The data on the generated active and reactive energy for a period of 2 years are similar to another previously considered HPP, with the difference being about 5 times in installed capacity [4].

This population of statistical units, which in this case are empirical data for active and reactive energy (representing power multiplied by time duration), has been processed, which allows certain regularities to be established based on analysis. The tables that have been done, including calculation results, are implemented according to the rules of statistics [4, 8, 9, 10].

The so-called scattering measures are presented in tabular form [4, 8, 9], respectively *arithmetic mean*, *geometric mean*, *arithmetic mean deviation*, *mean square deviation*.

Table 2 and Table 3 present calculated summarizing indicators of the produced active electricity for the two years under consideration.

Table 2: *Statistical indicators, determined for the first year set for a month.*

Arithmetic mean $\bar{x}$, *kWh*	**Geometric mean $\bar{\sigma}$, *kWh***	**Arithmetic mean deviation *δ*, *kWh***	**Mean square deviation *s*, *kWh***
585 816	544 179	480 681	518 100

Table 3: *Statistical indicators, determined for the second year set for a month.*

Arithmetic mean $\bar{x}$, *kWh*	**Geometric mean $\bar{\sigma}$, *kWh***	**Arithmetic mean deviation *δ*, *kWh***	**Mean square deviation *s*, *kWh***
1 347 979	1 269 216	975 546	1 087 900

According to the data from Table 1, it is established that the arithmetic mean value of the plant's operation for the first year under consideration is 19,260 kWh per day, which means 3.95 (≈4.0) hours of operation per day. For the second year under consideration, the arithmetic mean value is 44,317 kWh per day, which means 9.08 (≈9.0) hours of operation per day.

7. Conclusions

After examining the HPP as a source of electricity and presenting the features of the activity of the Tazha HPP, the main goal has been achieved, namely the summarizing indicators for the plant's activity have been derived based on data for a two-year period.

Using statistics, scattering measures have been determined – arithmetic mean, geometric mean, arithmetic mean deviation, and mean square deviation.

The results obtained are of interest from an applied point of view in order to establish certain trends during relevant analyses.

It is worth noting that despite the installed capacity of 4.9 MW, according to the calculated statistical characteristics, the maximum value of the generated and, accordingly, delivered to the energy system and sold active power reached almost 0.6 MW for the first year under consideration and 1.35 MW for the second year. This raises the question of whether the business plan for the construction of such a plant, prepared before the investment and installation (construction), with any payback period, would have been implemented. In all cases, it is a question of invested own funds or funds obtained through a bank loan. In this regard, it can be pointed out that not all hydro groups will operate continuously, as some of them may be taken out for repairs, mainly due to problems with the turbines or generators (mainly in the bearings) or in the transmission mechanisms. The latter emphasizes the role of preventive maintenance in achieving the planned electricity production.

The following are important considerations, also mentioned at the beginning:

- ✓ The efficiency of small HPPs is significantly lower than that of large HPPs built after dams, as the former are highly dependent on the annual season and rainfall.
- ✓ Capital investments for the construction of small HPPs are relatively low and pay off relatively quickly.

Regardless of the already known inconveniences in the use of RES, the so-called 'green energy' and its storage for later use is set to be the basis of the sustainable energy of the future.

As with other sources of energy, the goal of RES is to generate energy at the least cost. However, adequate programs, investments and mechanisms are needed to encourage the further development of this production. The dynamic regulatory environment that has been observed in recent years and the introduction of restrictive measures have a significant negative effect on the financial situation of companies, worsen the competitiveness of hydroelectric power generation and prevent the implementation of new projects in the sector. In order to avoid the adverse consequences of this policy, which will most sensitively affect the price of energy for society, the creation of a predictable regulatory framework ensuring the sustainable development of the sector is an urgent priority.

Electricity use is constantly growing, and conventional sources are being depleted at a very rapid rate. One of the solutions to prevent the energy crisis is for people to start getting more energy from RES. In practice, several types of renewable energy are often used together to combine their advantages for maximum efficiency for each specific application. In addition, energy storage systems can be included.

8. Acknowledgments

The implementation of this paper is thanks to the support from: the Project BG16RFPR002-1.014-0005 Competence Center 'Intelligent Mechatronic, Eco- and Energy-Saving Systems and Technologies' financed by the Operational Program 'Science and Education for Intelligent Growth' of the European Regional Development Fund.

9. References

1. https://fakti.bg/
2. https://www.investor.bg/
3. https://www.energy-review.bg/
4. Rachev S., Racheva M., Dimitrov L.: Data processing of energy generated by hydroelectric power plant (2025), *E3S Web of Conferences*. Vol. 638, art. no. 02005. EDP Sciences, 2025. ISSN: 2555-0403
   DOI: 10.1051/e3sconf/202563802005
5. https://nek.bg/
6. https://bg.wikipedia.org
7. Moses, Lincoln E. Think and explain with statistics. ADDISON-WESLEY, 1-3 (1986)
8. Rachev S., R. Turmanidze, V. Shilakadze. Statistical processing of data from the operation of a photovoltaic power plant, International Scientific Journal "INDUSTRY 4.0", 108-110 (2024) 20(1), ISSN (Print) 2534-8582, ISSN (Web) 2534-997X.
9. Rachev S.: Statistical Processing of Data from the Operation of a Wind Power Plant. *5th International Conference on Communications, Information, Electronic and Energy Systems (CIEES)*, 1-6, (2024). IEEE.
   ISBN: 979-835035286-3
   DOI: 10.1109/CIEES62939.2024.10811349.
10. Chance, Beth L. Investigating Statistical Concepts, Applications, and Methods. Duxbury Press, (2005).

Mechanical Behavior of Vein under Medical Compression Stocking. Preliminary Numerical Investigations

Nikola Nikolov, Elena Goranova

Institute of Mechanics, Bulgarian Academy of Sciences
n.nikolov@imbm.bas.bg

Abstract:

This work presents a numerical Finite Element Modeling of mechanical behavior of a human vein under influence of medical compression sock. The FE Model is developed in form of structural transient analysis by help of program product Ansys. The geometry of the vein and the muscle is assumed as an idealized, and consists of two coaxial cylinders. The stocking pressure is translated to the vein through the muscles contractions, surrounding tissues and the skin. Moreover, such a pressure and its variations, as well the position of the vein in the muscle environment, should also have influence on the functioning of venous valves and on the lymphatic system drainage. Because of preliminary character of this elaboration, these aspects are not discussed here.
The work set-up aims to establish principally how the stocking pressure loads the vein wall depending on different venous elasticity under given constant muscle elasticity.
The mechanical behavior of vein possessing elastic module E=30kPa and 100kPa is considered under stocking pressure Pst=25mmHg and 60.8mmHg and muscle tissue with elastic module Em=12kPa. The displacements in the vein and muscle with corresponded distributions of stress and strain states are identified in the both two elements.
It is concluded, that these two pressures induce similar stress values in the vein walls depending on the two venous elastic modules, correspondingly. Based on that, it is suggested that a 3-Dimensional space of the geometry, pressure and the elastic modules could be existed. In such a space, optimal patient-orientated values of the pressure depending on the geometrical sizes and elasticity should be available.

Keywords*: Venous ELASTICITY, Venous Surrounding tissue ELASTICITY, STRUCTURAL ANALYSIS, Finite Element Modeling*

1. Introduction

In XVII century William Hardy had found unidirectional blood flow in the human body because of the presence of valves [1].

In the vein the unidirectional transport is ensured by venous valves. A human vein and valve clinically observed are given in Fig. 1. The work of venous valve is numerically modeled in [2]. Non-closure of the venous valve leads to venous reflux as seen as yellow color in Fig. 1. A basic characteristic of the venous insufficiency is the retaining of blood in the capillaries and in the surrounding tissues. Such a retaining causes increase in the capillary pressure and succeeding swelling. The systematic retaining of the blood lead to appearance of oedema [3].

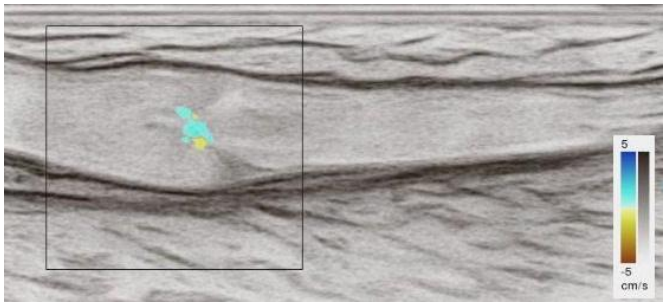


Fig. 1. Clinically observed vein and venous valve demonstrating blood reflux

Because of these circumstances the medical compressive therapy (Table 1) appears as a proper one for keeping the above pointed difference in the pressure and assures the drainage.
At this model, Fig. 2, venous valves are excluded. The pressure (Table 1) acting outside the surface of Volume 2 is transmitted by the tissues of this volume to the venous wall of Volume 1. This pressure could trans-murally lead to changes in the inside venous diameter, respectively in the venous lumen will influence the circulation and subsequent damages the venous valves.

Table 1. Ranges of Medicine Compression Stocking, [SIGVARIS]

Compr. Class for:	Compr. Mercury Column	Min Compr Pascal	Max Compr Pascal	Aver. Compr. Pascal
Prophyl axis	13 mmHg	1729		
Prophyl axis	18 mmHg	2394		
Travel	15-18 mmHg	1995	2394	2194.5
CCL1	18-21 mmHg	2394	2793	2593.5
CCL2	23-32 mmHg	3059	4256	3657.5
CCL3	34-36 mmHg	4522	6118	5320
CCL4	> 49 mmHg	> 6517		
Varix Ulcers	CCL1+(23-32)=53mmHg	7049		

The aims of this work are limited to (1) numerical developed model which should numerically describe (2) how the external surface of stocking pressure (Table 1) is transmitted from outside the skin surface through the tissue itself to the outside venous wall; (3) how the venous wall intra-murally transmit this pressure to the inside.
It is well known that, the new developed models (as well the theories!) are based on simplified idealized assumptions. Usually, that models are graphically presented, and often give adequate explanations, as well directions of future investigations. The proposed model is developed from such points of view.

2. Problem discussion

In their nature the described phenomenon present a combination of complex physico-chemical and biological live processes, and they are developed in a system “vein-environment tissues” in which deformation processes are initiated and advanced. That all is

performed with one only goal, namely – to keep the matter where they are developed alive. To achieve this goal it is extremely needed and important, that a big part of the processes to be strongly developed in acceptable limits of equilibrium, Fig. 3. To large extension these limits are determined by the range of variation of the applied external load, as well as the range of variation of the geometry and material properties of the elements in the system.

A structural analysis is performed in this work **because** the attention is concentrated on the deformation behavior of the two elements with different elasticity only as response of the surface stocking pressure. In fact, there are complicated fluid-structural interactions during the venous blood transport. That effects are not discussed here. The work has a **preliminary character because** the aims are to find venous deformations related to the different elasticity and to suggest possible negative effects on the venous wall. Enlargement and complicating of this work taking into account the above circumstances could be a subject of next works.

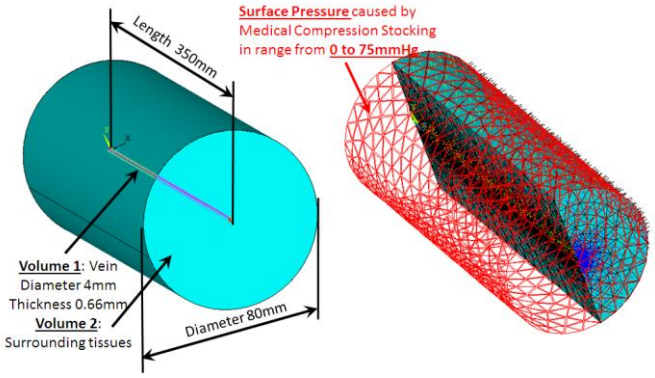


Fig. 2 Geometry of the FE model and Loads

The real structural composition of Volume 2 (surrounding/ environment tissue of the vein) contains as materials besides derma, muscles, bones and lots of fine blood system and lymphatic system. The compression on the outside surface of this volume means practically compression on these structural elements numbered in itself. Under normal work conditions the peripheral capillary blood system supplies nutritive substances to the tissues in Volume 2, and the lymphatic system drains surplus amounts of lymphous fluid from the same volume.

In reality the venous structure is very complex and specific for each human individual, respectively it is very difficult to build a total numerical approximation to a given real case. Here, a vein with diameter of 4mm, thickness of 0.66mm and length 350mm is treated under surrounding tissue possessing outside diameter of 80mm and the same length of 350mm, Fig. 2. Generally, the veins are situated under intramuscular and inter-compartment conditions. At the second, the influence of the environmental elements as arteries, bones, skin, fats, fascia *etc.* is directly applied on the outside vein wall. These two common cases will not be separately discussed in this work. These two common cases will not be separately discussed in this work. The venous Volumes 1 and 2 are separated in 97791 and 246990 finite elements with 189247 and 342920 nodes, correspondingly. Boundary conditions of zero-displacement and symmetry are applied in the two ends of the Volumes 1 and 2. Contact conditions are applied between outside surface of Vol. 1 and inside surface of Vol. 2.

In the numerical investigations of deformation processes, the material's mechanical behavior under external loads is usually described by help of materials' models. There exist, and there are continuously developed [3] great number of materials' models of biological tissues including such ones of vascular origin. The classical linear Hook's material model is assumed in this work for both the vein and its surrounding tissue taking into account the preliminary type of this work. It determines a linear dependency between the stress state and strain state in given material, and both the states are related through Elastic module which is characteristic for each material.

In Fig. 3, experimentally obtained stress-strain diagrams (broken black step-like line) under uniaxial tension of venous sample are given. Based on these lines linear elastic (Hook's, green ellipse) and hyperelastic (5-parameter Mooney-Rivlin, thin blue line and numbers) material models are derived.

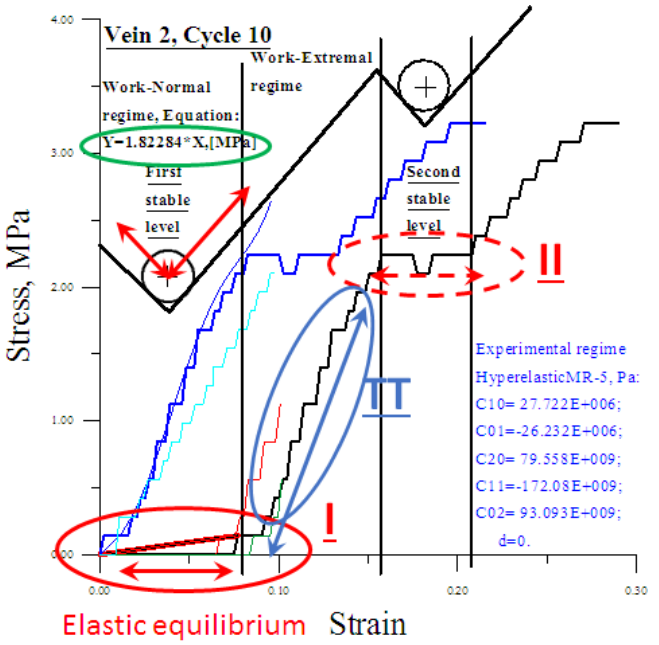


Fig. 3. Experimentally obtained stress-strain diagram by venous sample. Linear and Mooney-Rivlin elastic materials' models of vein demonstrating stable equilibrium and transitional regime of loading.

Two I and II stable equilibrium elastic regimes (red ellipses) of experimental venous behavior are seen. Above the diagram the two regimes are graphically illustrated by deviations of boll from its equilibrium state on the sloped surface. Four structural levels of deformation are established depending on corresponding regimes of increasing strain values. The first (I) equilibrium regimes is read under strain values until 0.08. After that, a transitional (TT) regime is seen up to strains 0.15 under acute increased stresses. With next increasing strains from 0.16 to 0.21, a second (II) equilibrium regime is read under relatively low increasing stresses. The rupture regime of this venous sample is established under increased strain value of 0.3.

Three levels of venous insufficiency are identified according to [4] depending on experimentally established venous elastic modules lower than 30kPa. Above 30kPa and upper 100kPa the vein is discussed as a normal. In this work the deformation behavior of vein with elastic modules of 30 and 100kPa assumed as limiting is numerically modeled under increasing compressive stocking pressure from 0 to 75mmHg (Table 1) applied on the outside surface of surrounding tissue with elastic module of 12kPa,.

Strain enlargement process and form change process are simultaneously developed in Vols 1 and 2 as effect of external pressure. The stability of deformation process depends on loss of stability of one in between both the processes. The loss in strain enlargements leads to strain localizations in and ruptures. The loss of form-change leads to wrinkles and warps, compromised damaged forms and fractures.

Equilibrium equations are solved under the corresponding boundary conditions, and as result corresponding node displacements, Figs 4 and 5, with corresponding stress strain distributions, Figs 6 and 7, are obtained relating the vein deformation behavior to stocking compression Fig. 2 and Table 1, depending on the assumed elastic material models for the vein and the tissue.

3. Objective and research methodologies. Results

The numerically obtained displacements in the vein and the surrounding tissue are "conditionally" presented in macro-, mezo-

and micro-levels related to opportunity similar experimental ones to be clinically observed.

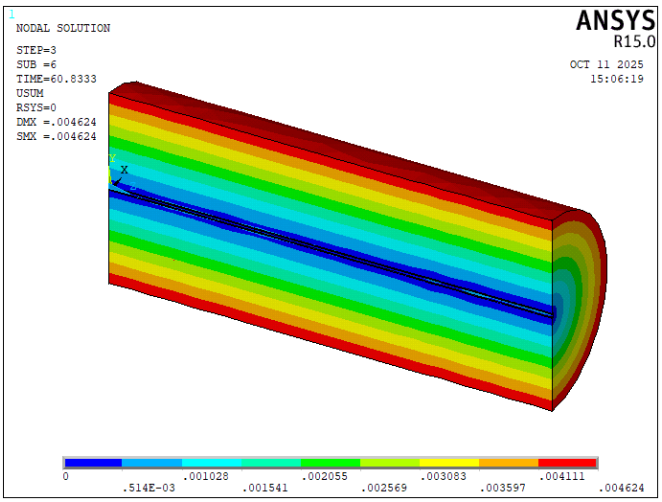


Fig. 4. Macro-level of the displacements in vein with Evein=30kPa and tissues with Emuscle=12kPa under MCS of 60mmHg.

In Fig. 4 the macro-distributions of the displacements are given across and longitudinal in the vein. Concentrically decreasing values from 4mm on the surface to 0.5-1mm in the vein and closely to vein are seen. Irregular displacements are longitudinally understandable in the vein at this observation level. With decreasing scale-observations to micro-level, three areas of displacement with equal values are seen in Fig. 5. The displacement in vein with E=100kPa have regular character under the two pressures. In the vein with E=30kPa the concentration of the displacements are clearly seen with the higher load of 60mmHg.

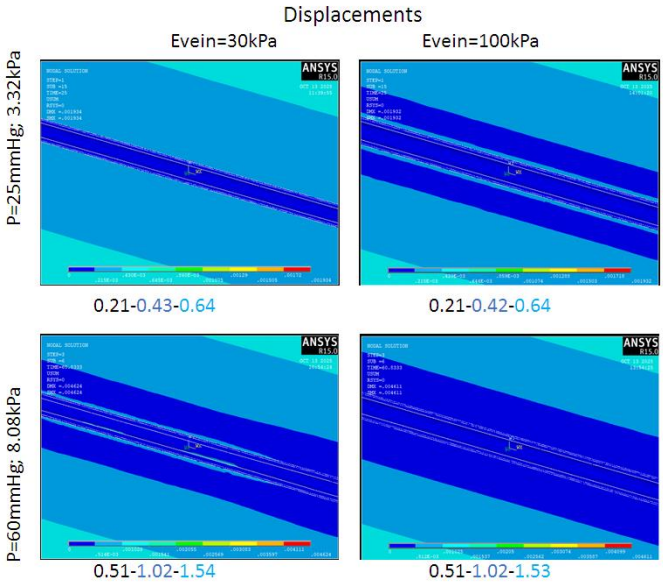


Fig. 5 Displacement, mm in meso-level in vein with Evein=30 and 100kPa and Emuscle 12=kPa under P=25 and 60mmHg.

It should be emphasized, the subject of this elaboration is concentrated on the numerically modeled deformation behavior of idealized forms of the two volumes determined by their mechanical properties. The corresponded to Fig. 5 strain- and stress-distributions are presented in Figs 6 and 7. Twice-thrice increased venous strain are seen with Ev=30kPa while the stress differences in are of one time and half. Related to strain-values in the I-equilibrium state in Fig. 3, the values higher of 0.12 for Ev=30kPa under 25mmHg and for Ev=100kPa under 60mmHg suggest transition to the TT-stage *i.e.* start of new structural level of deformation. Strain- and stress-distributions in the surrounding tissues have close to similar characters.

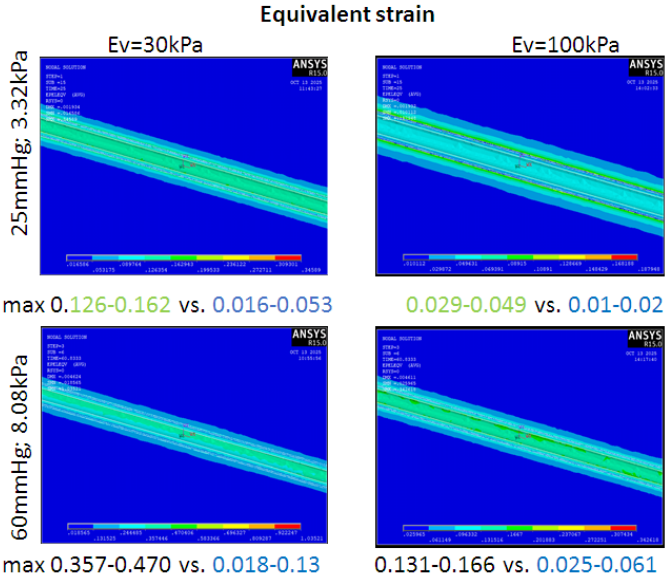


Fig. 6. Strain-distribution in meso-level in vein/tissue with Evein=30 and 100kPa and Emuscle 12=kPa under P=25 and 60mmHg.

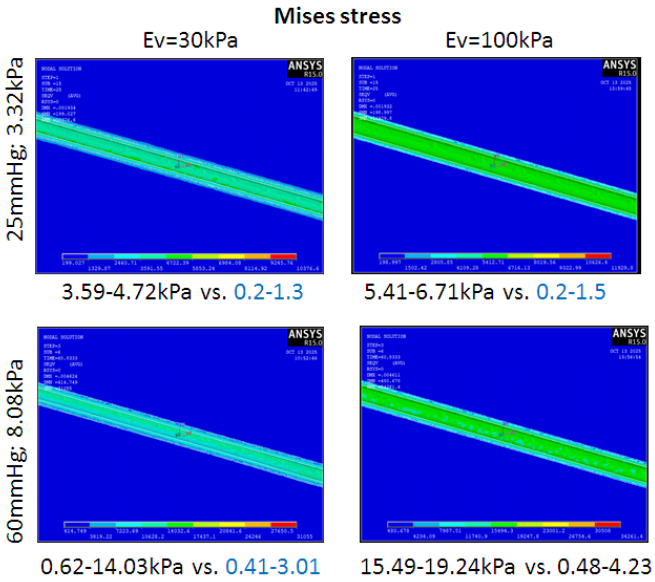


Fig. 7. Mises stress distribution in meso-level in vein/tissue with Evein=30 and 100kPa and Emuscle 12=kPa under P=25 and 60mmHg.

Next decreasing in "scale-level" numerical observation to micro-level and concentration of the attention on the vein reveal displacements and stress-strain distributions in longitudinal and trans-mural venous directions, Figs 8, 9, 10.

In Fig. 8 at P=25mmHg twice higher displacement's values for Ev=30mmHg are seen compared to Ev=100kPa. However, in Fig. 8 the loss of stability in the circular venous form is clearly seen with Evein=30kPa under P=60mmHg. The vein with Ev=100kPa obtains more elliptical form at 70mmHg. Here, it must be strongly pointed that this surface stocking pressure is over-pressure according to Table 1, but we are here numerically looking for the limiting loading regimes depending on the venous elasticity. Such loading regimes could be related to different deformation behavior specific for given elastin-collagen contents.

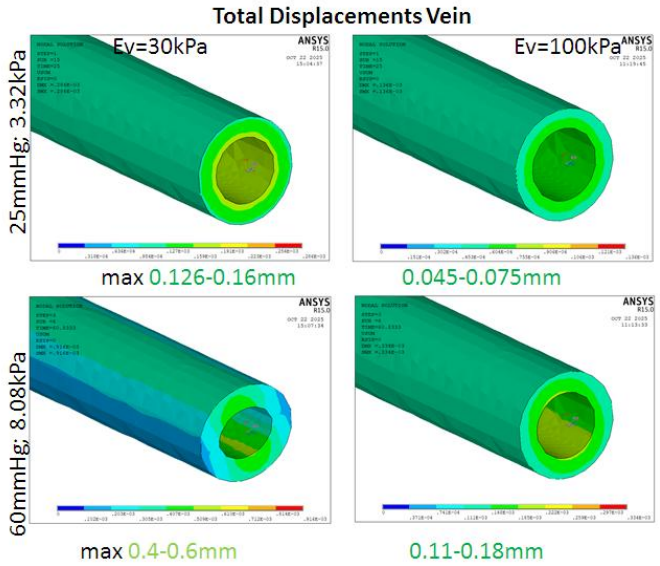


Fig. 8. Displacement in micro-level in vein with Evein=30 and 100kPa and Emuscle 12=kPa under P=25 and 60mmHg.

Next, the attention on the strain values of vein with Ev-30kPa (Fig. 9) establish that the values of 0.031-0.066 at 25mmHg are in the ranges of the I-rst equilibrium Work-Normal regime seen in Fig. 3, and upper value goes closely to the limit of 0.08. Surface P=60kPa leads to strain values 0.018-0.244, where the second values indicates structural transformation in the venous wall. The surface stress values observed in Fig. 9 are approximate to the values of 3.32 and 8.08kPa (25 and 60mmHg) applied to the surface of the venous surrounding tissue

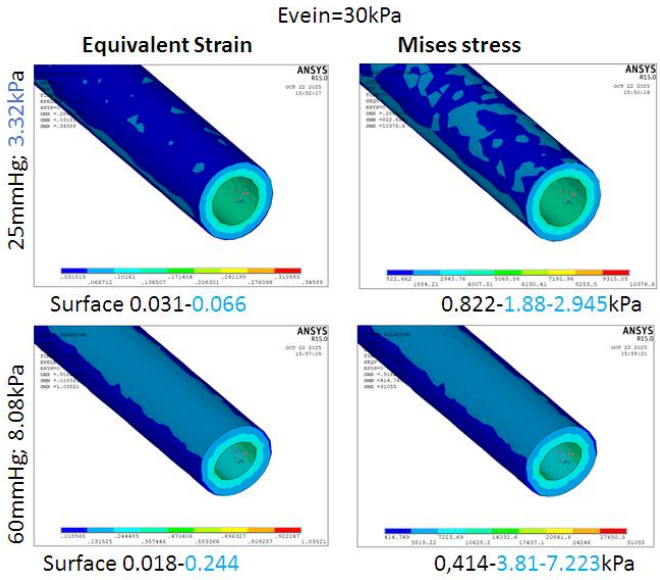


Fig. 9. Strain and stress distributions at micro-level in vein with Evein=30kPa and Emuscle 12=kPa under P=25 and 60mmHg.

Analyses of Fig. 10, as well Fig. 8, reveal a stably deformed cylindrical form of the vein with Ev=100kPa. Looking at the strain values from 0.022-0.034 to 0.061-0.096 for P==25 and 60mmHg correspondingly, it could be concluded that the vein works under equilibrium conditions of the Ist level, Fig. 3. The venous stress values are in commensurable ranges to the surface pressure of P=25 and 60mmHg. They show that the surface stocking compression is transmitted by the venous surrounding tissue possessing Emuscle=12kPa to the outside venous wall with similar values. Questions could be here imposed about these stress values, could they cause structural (elastin-collagen, including fibre tearing) transformations in the vein with E=30kPa and do not cause in this one with Ev=100kPa. That is out of the subject of this work because of its initial work stage.

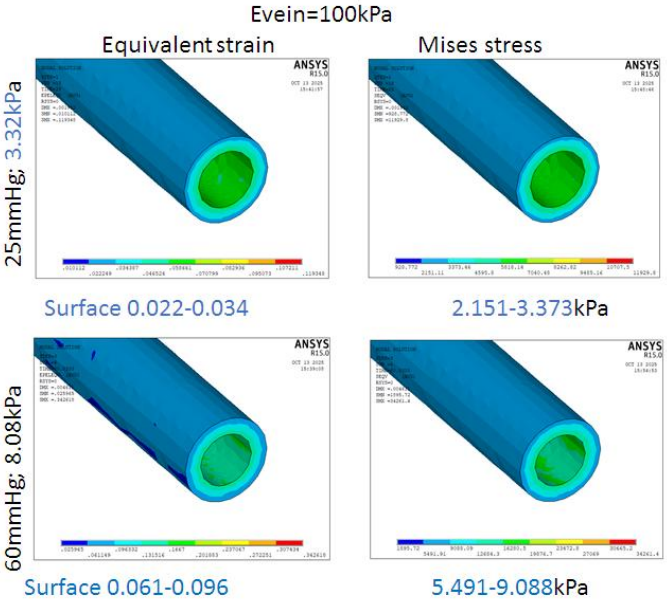


Fig. 10. Strain and stress distribution at micro-level in vein with Evein= 100kPa and Emuscle 12=kPa under P=25 and 60mmHg.

4. Conclusions

A 3-D numerical simulation of mechanical behavior of vein under medicine compression stocking is developed by help of FE Modeling and Ansys program product, Fig. 2. The vein is modeled as tube with diameter 4mm, thickness 0.66mm, length 350mm and having elastic (Young) modules Ev=30kPa and 100kPa. The surrounding tissue of the vein has diameter 80mm, the same length of 350mm and elastic module Emuscle=12kPa. Linear elastic (Hook) materials' models are assumed, as in elastic equilibrium loading stage, Fig. 3. The surrounding-tissue surface is compressed step-by-step in range from 0 to 75mmHg, Table 1. Three levels of distributions of the displacements, strain and stress in the vein are presented under pressure P=25 and 60mmHg in Figs 4-11. It is established that the strains in vein with Ev=100kPa have values below 0.08, as these ones characteristic for the normal elastic equilibrium loading stage given Fig. 3. With Ev=30kPa at pressure of P=25mmHg the strains are lower than the equilibrium of 0.08, but with increasing P=60mmHg elliptical loss of stability in the venous form-change process is established at thrice higher strain 0.244 than the equilibrium limiting one 0.08. It is established for the two venous elasticities, that all surface pressures P from 0 to 75mmHg are transmitted in similar stress values on the outside venous wall, Figs 9-10 approximately of 3.32 and 8.08kPa for cases of P=25 and 60mmHg. Finally, we conclude 3-D space of the geometry, pressures and elastic modules could be existed. In such a space, optimal patiently-orientated values of the stocking pressure should be available depending on the geometry and elasticity.

References

1. T. Young, The Croonian Lecture. On the Functions of the Heart and Arteries. *Phil. Trans. Roy Soc.*, **99,** 4 (1809), London, 1-31.
2. E. Goranova, N. Nikolov, Numerical Modeling of the Venous Valve Functioning. *J. of Theoretical and Applied Mechanics*, **51** (2021) 468-487.
3. P-Y. Rohan, P. Badel, B. Lun, D. Rastel, S. Avril, Prediction of the Biomechanical Effects of Compression Therapy on Deep Veins using FEM *Annals of Biomedical Engineering*, **43**, No. 2, (2015) 314–324.
4. H. Clarke, S.R.G. Smith, S.N. Vasdekis, J.T. Holls, A.N. Nicolaides, Role of venous elasticity in the development of varicose veins. Br.J. Surg. **76,** 1989, June, 577-580.